CY CERGY PARIS UNIVERSITÉ

Ammonia in Star-Forming Regions: Insights into Desorption, Binding Energies, and Surface Formation, through Experiments and Models

---

A Doctoral Dissertation by

Shreya KAKKENPARA SURESH

Supervisors:

Prof. François DULIEU
Prof. Paola CASELLI
Dr. Olli SIPILÄ

Jury:

President:
Prof. Fabrice DUVERNAY

Examiners:
Dr. Stephanie CAZAUX
Dr. Marcelino AGUNDEZ

To Amma and Achan

Contents

List of Figures

Abstract

Throughout their life cycle, stars leave a legacy of evolving chemical compositions within the interstellar medium (ISM). In this evolving chemical landscape, Nitrogen (N) is particularly intriguing. Nitrogen is critical for the formation of essential biomolecules such as amino acids and nucleobases. Among the several N-bearing species, ammonia (NH_3) stands out for several reasons. It has been observed across a variety of sources, is one of the few species detected both in the gas-phase and within ices, is a robust temperature probe, and a reliable tracer of the densest parts of star-forming regions. Despite its importance, the chemistry of NH_3, particularly on grain surfaces, remains little explored, highlighting a significant gap in our understanding of interstellar nitrogen chemistry.

In this thesis, I examine the surface chemistry of NH_3 during the earliest stages of star-formation. I employ a combination of experimental and modelling techniques. In the first part of this study, I perform experiments to study the impact on the desorption of NH_3 in mixed ices composed of H_2O, CO, and CO_2. I also estimate the binding energy of NH_3 on two types of ices - compact Amorphous Solid Water (c-ASW) and crystalline ice (CI). The presence of H_2O lowers the desorption rate of NH_3 and traps a fraction of the adsorbed NH_3. On each type of water ice, NH_3 has a distribution of binding energies, rather than a single value as suggested in literature. The results indicate that NH_3 can remain on dust grains over a broad range of temperatures and may lack a definitive snowline, with its desorption being significantly influenced by its chemical environment.

In part two, I incorporate the experimentally determined values of NH_3 binding energy into a model of a pre-stellar and a protostellar core and use a gas-grain chemical code to evaluate how varying the binding energy impacts NH_3 abundances in these sources. In pre-stellar cores, changing the binding energy did not affect gas-phase NH_3 abundances. In protostellar cores, higher binding energy values led to lower gas-phase abundances of NH_3 and a decrease in the size of the NH_3 desorption zone while lower values produced the opposite effect. The impact of these variations is further explored through radiative transfer modelling of the NH_3 (1,1) transition. These binding energy dependent variations in NH_3 abundances also affect the abundances and formation of other species chemically linked to NH_3.

In part three, NH_3 formation on grain surfaces via successive hydrogenation of N atoms is explored, with a specific focus on its formation in cold, dark molecular clouds. This part of the research integrates experimental techniques with modelling. The experiments involve depositing nitrogen and hydrogen atoms onto a surface maintained at 10 K and monitoring the process using Fourier Transform Infrared (FTIR) spectroscopy. In parallel,

the modelling aims to simulate these experiments by developing a custom chemical network of nitrogen, hydrogen, and related species and tracking the hydrogenation process using a gas-grain chemical code. I present the results of the calibration for both the experimental setup and the models. Additionally, I outline the forthcoming steps for this project, which is innovative in its attempt to bridge the gap between simulations and experiments.

In the future, addressing several key areas, including examining a range of binding energies for NH_3 in models, investigating the behaviour of NH_3 in ices with other compounds such as CH_4 and CH_3OH, and understanding how various physical and chemical conditions influence NH_3 formation on grain surfaces, could significantly improve our understanding of NH_3 chemistry. Additionally, expanding research to include other N-bearing species, such as cyanides, nitriles, and more complex amines, will offer a deeper insight into nitrogen chemistry in the ISM.

Keywords: Astrochemistry – Ammonia – Binding Energy – Experiments – Astrochemical Modelling – Prestellar cores – Protostellar cores

Résumé

Les étoiles enrichissent le milieu interstellaire (ISM) en éléments chimiques tout au long de leur cycle de vie, notamment en azote (N), un élément clé dans la formation de biomolécules comme les acides aminés. Parmi les espèces azotées, l'ammoniac (NH_3) est particulièrement notable, détecté à la fois en phase gazeuse et dans les glaces, et jouant un rôle crucial dans les régions de formation stellaire. Pourtant, la chimie de surface de NH_3 reste peu étudiée, laissant une lacune importante dans notre compréhension de la chimie de l'azote dans l'ISM.

Cette thèse explore la chimie de surface de NH_3 lors des premières étapes de la formation stellaire en combinant expériences et modélisation. Dans la première partie de cette étude, mes expériences ont montré que la désorption de NH_3 est influencée par la composition des glaces mixtes, comme celles contenant H_2O, CO, et CO_2. J'ai déterminé que NH_3 présente une distribution d'énergies de liaison sur différents types de glaces - l'eau solide amorphe compacte (c-ASW) et la glace cristalline (CI)- plutôt qu'une valeur unique. Ces résultats indiquent que NH_3 peut rester sur des grains de poussière sur une plus large gamme de températures et peut ne pas avoir de limite de neige définitive, sa désorption étant significativement influencée par son environnement chimique.

Dans la deuxième partie, j'intègre les valeurs déterminées expérimentalement de l'énergie de liaison de NH_3 dans un modèle physique de noyau pré-stellaire et protostellaire. J'utilise un code chimique gaz-grain pour évaluer l'effect de la variation de l'énergie de liaison sur l'abondance de NH_3 dans ces sources. Dans les noyaux préstellaires, la modification de l'énergie de liaison n'a pas affecté l'abondance de NH_3 en phase gazeuse. Dans les noyaux protostellaires, des valeurs d'énergie de liaison plus élevées ont conduit à une diminution de l'abondance de NH_3 en phase gazeuse et à une diminution de la taille de la zone de désorption de NH_3, tandis que des valeurs plus faibles ont produit l'effet inverse. L'impact de ces variations est exploré plus en détail par la modélisation du transfert radiatif de la transition NH_3 (1,1). Ces variations de l'abondance de NH_3 dépendantes de l'énergie de liaison affectent également l'abondance et la formation d'autres espèces chimiquement liées à NH_3.

Dans la troisième partie, j'explore la formation de NH_3 à la surface des grains de poussière dans les nuages moléculaires froids et sombres, via l'hydrogénation d'atomes d'azote. Cette partie intègre des techniques expérimentales à la modélisation. Les expériences impliquent le dépôt d'atomes d'azote et d'hydrogène sur une surface maintenue à 10 K et la surveillance du processus à l'aide de la spectroscopie infrarouge à transformée de Fourier (FTIR). Parallèlement, la modélisation visait à simuler ces expériences en développant un réseau

chimique personnalisé d'azote, d'hydrogène et d'espèces apparentées et en suivant le processus d'hydrogénation à l'aide d'un code chimique gaz-grain. Je présente les résultats de l'étalonnage pour la configuration expérimentale et les modèles. De plus, je décris les prochaines étapes de ce projet, qui est innovant dans sa tentative de combler le fossé entre les simulations et les expériences.

À l'avenir, l'examen de plusieurs domaines clés, notamment l'examen d'une gamme d'énergies de liaison pour NH_3 dans les modèles, l'étude du comportement de NH_3 dans les glaces avec d'autres composés tels que CH_4 et CH_3OH, et la compréhension de la manière dont diverses conditions physiques et chimiques influencent la formation de NH_3 sur les surfaces des grains, pourraient améliorer considérablement notre compréhension de la chimie du NH_3. De plus, l'élargissement de la recherche à d'autres espèces porteuses d'azote, telles que les cyanures, les nitriles et les amines plus complexes, offrira un aperçu plus approfondi de la chimie de l'azote dans le milieu interstellaire.

Mots clés: Astrochimie – Ammoniac – Énergie de liaison – Expériences – Modélisation astrochimique – Noyaux préstellaires – Noyaux protostellaires

1

Theoretical Background

1.1 The Interstellar Medium

Stars are the fundamental building blocks of the universe, playing a crucial role in its evolution and composition. The most abundant element, hydrogen (H), was created during the Big Bang, along with smaller amounts of helium (He), deuterium (D), and trace quantities of lithium (Li). The creation of other essential elements, such as carbon (C), nitrogen (N), oxygen (O), and heavier elements (collectively known as metals), occurs within the cores of stars in a process called nuclear fusion, where atomic nuclei are fused to form new atomic nuclei. Stars enrich the medium surrounding it through stellar winds and supernovae (the dramatic endpoints of massive stars). Therefore, understanding the formation and lifecycle of stars is essential for comprehending the complex and dynamic nature of our universe.

The space between stars, known as the Interstellar Medium, is filled with gas and dust. Gas constitutes 99% of the ISM by mass, while dust makes up the remaining 1%. Of the gas, 70% is hydrogen, 28% is helium, and 1.5% consists of heavier elements. Dust grains are typically composed of carbonaceous material or silicates. Interstellar matter is not uniformly distributed throughout a galaxy; instead, it is concentrated in clumps and filaments of various scales, part of larger structures called molecular clouds. Stars are born from the ISM, specifically in the densest and coldest regions of these clouds.

The ISM exists in different phases, each in pressure equilibrium with the others, and is categorised based on whether the matter is in atomic, ionised, or molecular form. The **Warm Ionised Medium (WIM)** has a temperature of approximately 8000 K and a volume number density of about 0.3 cm^{-3}, with hydrogen typically in ionised form. The WIM can be observed using Hα emission or pulsar dispersion methods. The **Warm Neutral Medium (WNM)** has a similar temperature but a slightly higher number density of around 0.5

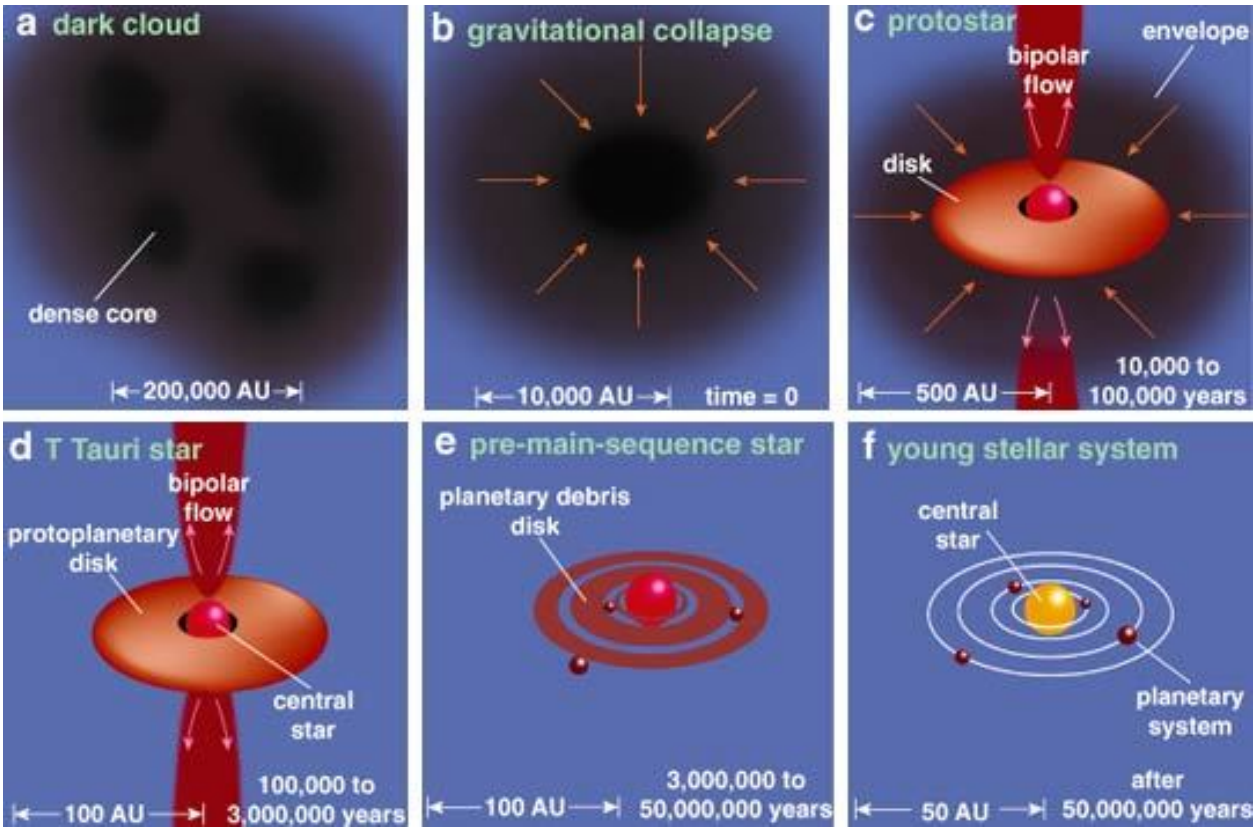

Figure 1.1: Illustration depicting main stages of low-mass star formation. *Source: Sahoo (2016).*

cm^{-3}, with most of the hydrogen in atomic form. The **Cold Neutral Medium (CNM)**, in contrast, has a temperature of about 100 K and a number density between 30 and 50 cm^{-3}. Both the WNM and CNM can be traced by the 21 cm line of atomic hydrogen in absorption or emission, as well as by optical and ultraviolet(UV) absorption/emission lines of various elements towards background stars. The **molecular phase**, where hydrogen is in molecular form (H_2), has temperatures ranging from 20 to 10 K and densities between 10^3 - 10^6 cm^{-3}. This phase is traced, for example, by the CO J = 1-0 transition at 2.6 mm. The molecular phase is particularly significant for star formation, as stars form within these dense and cold regions.

1.1.1 A Star is Born

Stars form due to the gravitational collapse of dense cores, known as *prestellar cores*, in molecular clouds. The mass of these dense cores dictates the evolutionary path of the stars that form from them. Stars can broadly be classified into two types based on their mass: high mass (greater than 8 $M_\odot$) and low mass (less than 2 $M_\odot$)[1].

The formation of high-mass stars is still poorly understood. These stars begin fusion in their cores and evolve into the main sequence stage within a short time frame of approximately 10^5

[1]Stars between 2 and 8 $M_\odot$ are called intermediate-mass stars

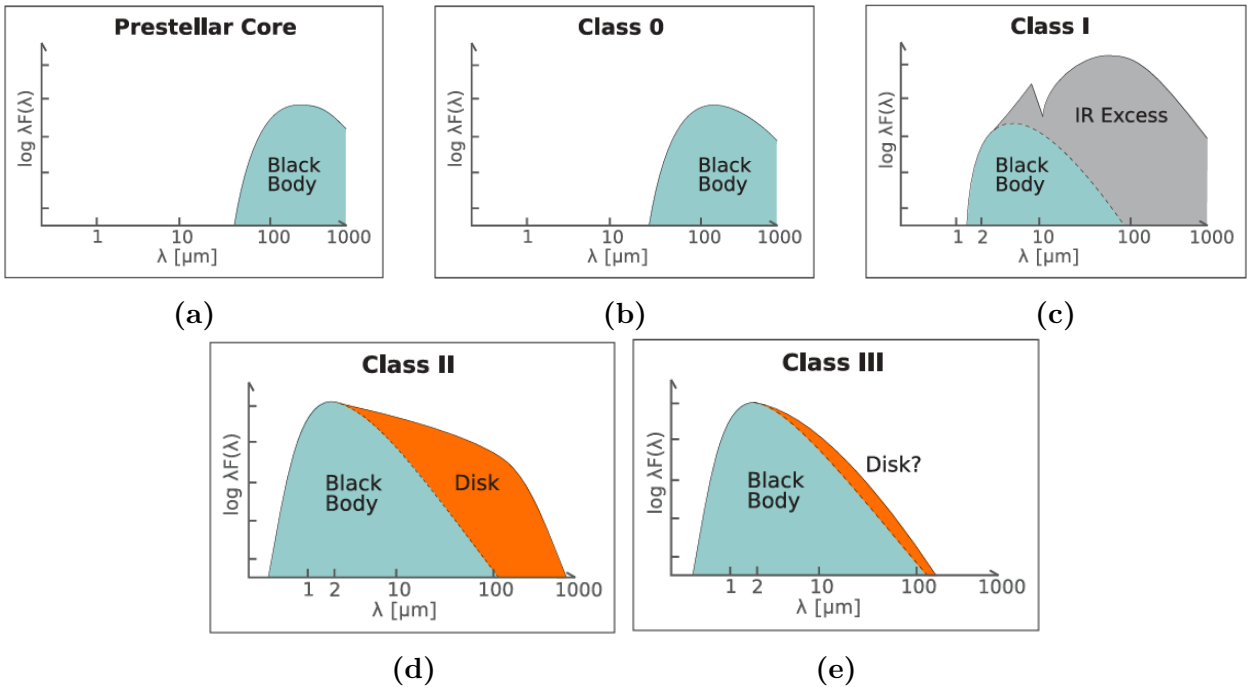

Figure 1.2: Spectral energy distributions at various stages of star formation. *Source: Persson (2014)*

years while still embedded in their parent cloud core. They emit intense UV radiation, leading to the creation of HII regions and photodissociation regions (PDRs) around them. The region surrounding the central protostar, characterised by high temperatures and densities, is known as a hot core. The lifecycle of a high-mass star typically ends as a neutron star or a black hole. High-mass star-forming regions are statistically located further away than low-mass star-forming regions, and high-mass stars are far fewer than their low-mass counterparts, which adds additional constraints to studying their formation.

In contrast, low-mass protostars take much longer, around 10^7 - 10^8 years, to evolve into the main sequence stage. Similar to high-mass protostars, hot core-like chemistry has been detected in their central regions, which are rich in complex organic molecules. These regions are referred to as hot corinos (Cazaux et al. 2003). The Sun and our solar system are believed to have formed from such a type of protostar.

Low-mass stars form from the collapse of dense cores, (Fig. 1.1 a and b) that are characterised by low temperatures (∼6 K, Pagani et al. (2007)) and high densities ($> 10^5$ cm^{-3}, Keto & Caselli (2008)). This collapse is isothermal because the core is effectively cooled by molecular line emission (mainly CO) and by dust grains. The spectral energy distribution (SED) lies primarily in the far-infrared, as shown in Fig. 1.2a. As the density of H_2 in the center increases beyond 10^{10} cm^{-3} (Larson 1969), the opacity of the core increases. Due to this increase in opacity, radiation is trapped within the cloud, raising the temperature of the central region of the core. When the central temperature exceeds 1500 K, H_2 begins to dissociate, a process that consumes a significant amount of energy. This energy consumption reduces the pressure stabilising the core during collapse, accelerating gravitational contrac-

tion and leading to a second collapse that forms a protostar (Fig. 1.1c). The protostar continues to grow as gas accretes onto it, still remaining deeply embedded in its envelope. The object is classified as a **Class 0** source (Fig. 1.2b).

To conserve angular momentum, the infalling material forms a flattened disk around the protostar while simultaneously releasing jets perpendicular to this disk. At this stage, the object is classified as a **Class I** source (Fig. 1.2c), with emission primarily in the far-infrared and weak emission in the near-infrared, originating from the surrounding dust and gas. Eventually, the gaseous envelope dissipates as it is accreted onto the protostar. Quasi-static contraction increases the central temperature of the protostar, with heat transported to the surface *via* convection. Most of the material from the parent cloud has dissipated, leaving behind a small disk known as a protoplanetary disk, where planetary systems can form. At this phase, the object is a **Class II** source (Fig. 1.2d) and is called a classical T-Tauri star (Fig. 1.1d and e). The central star, now a pre-main sequence source, becomes visible in the optical range along with mid-infrared emission from the disk. Finally, the remaining disk clears up, leaving behind a planetary system (Fig. 1.1f). At this stage, the emission is mainly from the central star, which is classified as a **Class III** source (Fig. 1.2e), indicating that most of the surrounding material has been accreted or dispersed.

1.1.2 Cloud instability and collapse

The dynamics of molecular clouds are dominated by gravity. To understand this, let us consider the simplest case where the only forces within a cloud are the gas thermal energy (U) acting outwards and the gravitational potential energy (Ω) acting inwards. If the cloud is in hydrostatic equilibrium, this balance can be expressed using the virial theorem as:

$$2U + \Omega = 0 \tag{1.1}$$

In this context, U represents the total kinetic energy of the gas particles. The virial theorem states that for a system in equilibrium, the thermal energy is balanced by half the magnitude of the gravitational potential energy. It indicates that if the thermal energy is not sufficient to balance the gravitational pull, the cloud will collapse under its own gravity. Conversely, if the thermal energy is too high, the cloud will expand. Understanding this balance is crucial for studying the stability and evolution of molecular clouds and the star formation processes within them.

For a typical molecular cloud of mass M, radius R, and temperature T, assuming spherical symmetry, the gas thermal energy and the gravitational potential energy can be expressed as follows:

$$U = \frac{3Mk_BT}{2\mu m_H} \tag{1.2}$$

and,

$$\Omega = \frac{GM^2}{R} \tag{1.3}$$

where k_B is the Boltzmann constant, G is the gravitational constant, μ is the mean molecular weight and m_H is the mass of the hydrogen atom. The ratio of thermal energy to gravitational energy is:

$$\frac{2U}{|\Omega|} \approx 2 \times \left(\frac{3Mk_BT}{2\mu m_H}\right)\left(\frac{GM^2}{R}\right)^{-1} \approx 10^{-2}\left(\frac{T}{15K}\right)\left(\frac{R}{25pc}\right)\left(\frac{M}{10^5 M_\odot}\right)^{-1}. \tag{1.4}$$

From eq. 1.4, for conditions that are typical in molecular clouds, such as a giant molecular cloud (T $\approx$ 15 K, R $\approx$ 25 pc and M $\approx 10^5 M_\odot$), thermal support against gravity is very small. This encourages the collapse of the cloud leading to the formation of stars. When a cloud collapses due to self-gravity, the time scale for the collapse can be given by the free-fall time scale, τ_{ff} as

$$\tau_{ff} = \left(\frac{3\pi}{32G\rho}\right)^{\frac{1}{2}}, \tag{1.5}$$

where ρ is the density of the cloud, assuming a spherical homogeneous cloud. This free-fall time scale provides an estimate of the time it takes for a cloud to collapse under its own gravity in the absence of other forces. Observations have revealed molecular clouds with ages far greater than those estimated based on the free-fall timescale under typical molecular cloud conditions. Additionally, the star formation rate based on the free-fall timescale is two orders of magnitude higher than the observed rate (Robitaille & Whitney 2010). This suggests that other forces must be present to stabilise the molecular cloud against collapse and consequently regulate the star formation rate.

In the initial assumption, contributions from non-thermal motions, $\mathcal{K}$ (such as turbulence and the rotation of the cloud), and the magnetic field, $\mathcal{M}$, within the clouds have not been included. When these factors are incorporated, a more complete form of the virial theorem can be expressed as:

$$2U + \Omega + \mathcal{K} + \mathcal{M} = 0 \tag{1.6}$$

A detailed discussion of the implications of non-thermal motions and the magnetic field is beyond the scope of this thesis and is therefore omitted.

The maximum size a cloud can reach before it collapses is determined by two parameters, the *Jeans Mass* (M_J) and the *Jeans Length* (λ_J). The Jeans Length gives the maximum stable size, while the Jeans Mass determines the maximum stable mass a cloud can have such that it is still stable against collapse. Using the virial theorem, these two parameters can be derived as:

$$M_J \approx 2M_\odot \left(\frac{T}{15K}\right)^{\frac{3}{2}} \left(\frac{n}{10^3 cm^{-3}}\right)^{-\frac{1}{2}} \tag{1.7}$$

$$\lambda_J \approx 0.3pc \left(\frac{T}{15K}\right)^{\frac{1}{2}} \left(\frac{n}{10^3 cm^{-3}}\right)^{-\frac{1}{2}} \tag{1.8}$$

Both of these equations indicate that low temperatures and high densities favour collapse. Lower temperatures reduce the thermal pressure opposing gravity, while higher densities increase the gravitational pull within the cloud.

1.2 Chemical reactions in the interstellar medium

The ISM presents a rich repository of chemical species, with over 300 molecules[2] detected so far. This richness is a consequence of various chemical processes occurring within the ISM. These processes can be broadly categorized into two types: gas-phase reactions and grain-surface reactions. In the following sections, we will explore the different processes under each of these categories.

1.2.1 Gas-phase Reactions

Let us consider a bimolecular reaction of type A + B $\longrightarrow$ C + D. In terms of the reactants, the rate of change of their abundances can be given as:

$$\frac{d[A]}{dt} = \frac{d[B]}{dt} = -k[A][B] \tag{1.9}$$

Similarly, the rate of formation of the products can be expressed as:

$$\frac{d[C]}{dt} = \frac{d[D]}{dt} = k[A][B] \tag{1.10}$$

where [X] represents the number density of species X expressed in cm^{-3}, and k is the rate constant, which is a measure of how fast a reaction proceeds under the given conditions, and is typically expressed in cm^3 s^{-1}. The larger the value of k, the faster the reaction usually proceeds. The negative sign in eq. 1.9 indicates the decrease in the abundances of the reactants A and B as the reaction proceeds.

Similarly, for a unimolecular reaction, the rate can be given as:

$$\frac{d[A]}{dt} = -k[A]. \tag{1.11}$$

In this case, the rate constant k has the units s^{-1}.

[2] https://cdms.astro.uni-koeln.de/classic/molecules

Gas-phase reactions can be further subdivided into three categories based on their effects on chemical bonds: formation, destruction, and rearrangement (Fig. 1.3). Bonds are formed through processes such as radiative association and associative detachment, leading to the creation of both simple and complex species. Conversely, reactions such as photodissociation and dissociative recombination destroy bonds, resulting in the fragmentation of species. Reactions like ion-molecule exchange, neutral-neutral interactions, and charge transfer rearrange the chemical bonds of the reactants to create new species. A summary of these reactions is provided in table 1.1.

Table 1.1: Types of gas-phase reactions in the ISM along with their typical rate constants

Category	Type of reaction	Reaction	Rate constant (cm^3s^{-1})
Bond Formation	Radiative Association	$A + B \longrightarrow AB + h\nu$	10^{-17} – 10^{-14}
	Associative Detachment	$A^- + B \longrightarrow AB + e$	$\sim 10^{-9}$
Bond destruction	Photodissociation	$AB + h\nu \longrightarrow A + B$	10^{-10} – 10^{-8} [a]
	Dissociative recombination	$A^+ + e \longrightarrow C + D$	10^{-7} – 10^{-6}
Bond rearrangement	Ion-molecule	$A^+ + B \longrightarrow C^+ + D$	10^{-9} – 10^{-7}
	Neutral-neutral	$A + B \longrightarrow C + D$	10^{-11} – 10^{-9}
	Charge transfer	$A^+ + B \longrightarrow A + B^+$	$\sim 10^{-9}$

[a] Photodissociation rate constants have units of s^{-1}, because they are unimolecular reactions

Bonds are formed when two species approach, interact, and the resultant excess energy is carried away by collision with a third body. Even in the densest parts of the ISM (like prestellar cores) where densities can reach up to 10^6 cm^{-3}, such collisions are very unlikely as the densities are not sufficient for three-body collisions. In the absence of such a third body, the excess energy is carried away either by a photon (radiative association) or an electron (associative detachment).

In **radiative association**, two species collide and form a momentary activated complex. The excess energy generated is distributed among the different vibrational modes of this complex. If the energy is concentrated along vibrational modes that favour the dissociation of the complex, it leads to dissociation back into the initial reactant species. The probability that the formed complex will dissociate decreases for larger molecules due to the availability of many vibrational modes. The rate constant for radiative association is typically between 10^{-17} and 10^{-14} cm^3 s^{-1}. In **associative detachment**, an anion reacts with a neutral species, resulting in the formation of a neutral species and the ejection of an electron from the anion. These reactions can occur quite rapidly, with a rate constant of approximately 10^{-9} cm^3 s^{-1}.

Interstellar space is rich in ultraviolet (UV) photons, with an estimated density of around 10^8 photons cm^{-2} s^{-1} sr^{-1} (Habing 1968; Draine 1978). Molecules in the ISM can absorb

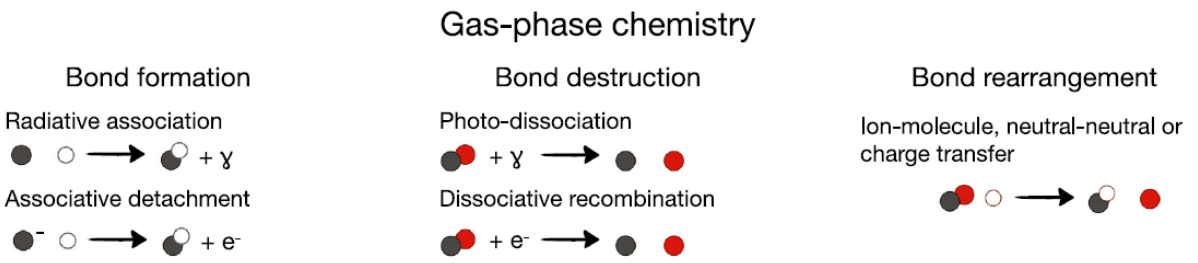

Figure 1.3: Schematic representations of gas-phase reactions. Source: Öberg & Bergin (2021)

these UV photons and undergo dissociation through a process called **photodissociation**. In the case of molecular hydrogen, dissociation takes place when H_2 in a dissociative excited electronic state dissociates into H atoms. In the diffuse medium or at the edges of clouds, these UV photons primarily originate from stars such as OB stars. Additionally, shocks contribute to UV photon production through the collisional excitation of H atoms or the recombination of H^+ ions.

UV photodissociation plays a crucial role in breaking molecular bonds, particularly near diffuse clouds where densities can be as low as a few tens of atoms per cm^{-3}, or at the edges of molecular clouds where UV photons can easily penetrate. Since molecular bond energies typically range from 5 to 10 eV (corresponding to wavelengths of approximately 3000 Å or shorter), UV photodissociation is a dominant destruction mechanism for molecules in these regions, with typical rates between 10^{-8} and 10^{-10} s^{-1}. Within the interiors of molecular clouds, the UV photon flux is reduced due to attenuation by dust and self-shielding by abundant species (like H_2). However, UV photons are still present in these regions, primarily due to cosmic rays. When a cosmic ray enters the cloud, it ionises the surrounding H_2 gas, generating energetic electrons. These electrons electronically excite H_2 molecules, which then decay radiatively, emitting UV photons. Cosmic rays can penetrate deep into the cloud, providing a constant source of UV photon intensity. The effective photodissociation rate constant within cold clouds can be represented as:

$$k_{pd} = a\, exp[-bA_v], \tag{1.12}$$

where a is the unshielded photodissociation rate constant, b is a constant dependent on the molecule and the adopted grain model, and A_v is the visual extinction due to dust.

Bonds can also be broken through **dissociative recombination**. In this process, a cation and an electron react to form a neutral species in an excited electronic state. This neutral species disintegrates into smaller fragments to conserve energy and momentum. This process is important to produce neutral species from molecular ions in interstellar clouds. For large molecules such as polycyclic aromatic hydrocarbons (PAHs), the energy in the excited electronic state of the resulting neutral species is distributed across various vibrational modes. This vibrational energy is subsequently emitted *via* infrared (IR) radiation. The rate constants for these reactions are typically around 10^{-7} cm^3 s^{-1}, with a temperature dependence varying between $T^{-1/3}$ and T^{-1}.

Ion-molecule reactions are crucial to the chemistry in cold, dark clouds. These ions are generated through collisions with cosmic rays. When an ion approaches a neutral molecule, the electric field of the ion induces a dipole in the neutral species. This polarization-induced interaction potential is generally sufficient to overcome activation barriers, allowing the reaction to proceed, particularly if it is exothermic. The rate constant for these reactions, known as the Langevin rate, is expressed as:

$$k_L = 2\pi e \left(\frac{\alpha}{\mu}\right)^{1/2}, \tag{1.13}$$

where α represents the polarizability of the neutral species and μ is the reduced mass. These reactions proceed rapidly, generally with rate constants around 10^{-9} cm^3 s^{-1}. The presence of a permanent dipole in the neutral species can further increase these rates. In such cases, the reaction rate constant is given by:

$$k_{dip} = 2\pi e \left(\left(\frac{\alpha}{\mu}\right)^{1/2} + \mu_D \left(\frac{2}{\pi \mu k T}\right)^{1/2}\right) \tag{1.14}$$

where μ_D is the dipole moment of the neutral species. Under these conditions, the value of the rate constant can reach up to 10^{-7} cm^3 s^{-1}. The rate constants of ion-molecule reactions are approximately two orders of magnitude higher than those of neutral-neutral reactions. Consequently, ion-molecule reactions are significant drivers of interstellar chemistry.

Neutral-neutral reactions possess a significant activation barrier due to the necessary breaking of bonds before rearrangement can occur. As a result, they become important in hot cores of protostars, shocks, and photodissociation regions near highly luminous stars, where the higher temperatures help overcome this activation barrier. In cold and dark environments like dark clouds or pre-stellar cores, only neutral-neutral reactions involving atoms or radicals with a single unpaired electron are significant. These unpaired electrons make the species highly reactive. Studies by Shannon et al. (2013) have shown that reactions between a radical and a neutral species can proceed at elevated rates due to quantum mechanical tunnelling through the activation barrier. The typical reaction rate constants for neutral-neutral reactions under these conditions are of a few 10^{-10} cm^3 s^{-1}.

Charge-transfer reactions involve an ion taking an electron from an atom or a molecule. This type of reaction is important for maintaining the ionisation balance in the ISM, for example, of trace species in HII regions. Rate constants can be of the order of 10^{-9} cm^3 s^{-1}.

1.2.2 Grain Surface Reactions

Though comprising only about 1% of the ISM by mass, dust grains (fig. 1.4 *left*) play a crucial role in its chemistry. These sub-micron-sized particles, typically composed of carbonaceous material or silicates, such as $Mg_{2x}Fe_{2-2x}SiO_4$, pyroxenes, and olivines, are formed by the condensation of atoms or molecules ejected during supernova explosions or from the outer layers expelled by asymptotic giant branch (AGB) stars. Dust grains shield the interiors of

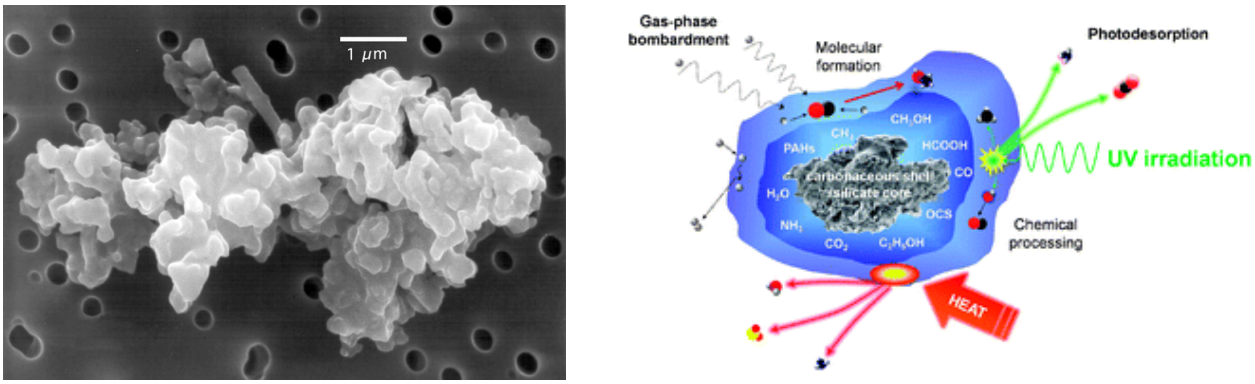

Figure 1.4: *Left:* Image of an Interplanetary Dust Particle (IDP), which could be a composite of interstellar dust grains, *Source: Jessberger et al. (2001)*; *Right:* Schematic depicting the major components of ice around a dust grain and the various pathways for ice processing in astrophysical environments. *Source: Burke & Brown (2010)*.

molecular clouds from UV radiation, allowing molecules to survive longer in these regions than in diffuse clouds. This shielding facilitates the formation of complex molecules (such as complex organic molecules; COMs), that are abundant within these clouds. Additionally, the formation on dust grains is essential to explain the creation and observed abundances of several species detected in the ISM. Dust grains provide surfaces where species can meet and react, and act as sinks for the excess energy produced in molecular reactions. The dissipation of excess energy stabilises the products formed. In this manner, dust grains contribute to the enhancement of the chemical richness of the ISM, especially under the cold conditions found in molecular clouds.

In dense regions of molecular clouds, where temperatures can be as low as 10 K, dust grains are often enveloped by molecular species accreted onto the grain. Under these conditions, the ice is mainly composed of H_2O, followed by CO, CO_2, NH_3, CH_3OH, and CH_4 (together referred to as volatiles), forming a "dirty" mixture (Fig. 1.4 *right*). The accreted species can diffuse on the ice surface and react with other species, enriching the chemical composition of the ice. Reactions on the ice can also be triggered by cosmic rays or UV irradiation. The various chemical processes on dust grains are elaborated in the following sections.

Adsorption

Grain surface chemistry begins with the accretion of species from the gas-phase, *via* collisions, onto dust grains, where they stick to the surface – a process called **adsorption**. Species are adsorbed onto local minima of the interaction potential between the species and the surface, called sites. Adsorption can be classified as **physisorption** or **chemisorption** based on the depth of the potential well. Physisorption (Fig. 1.5a) involves Van der Waals or electrostatic forces, with well depths between 0.01 - 0.2 eV (100–2000 K), while chemisorption (Fig. 1.5b) involves the formation of chemical bonds with well depths of approximately 1 eV (10,000 K). The temperature below which a species is efficiently adsorbed onto the grain surface is known as the **adsorption temperature**.

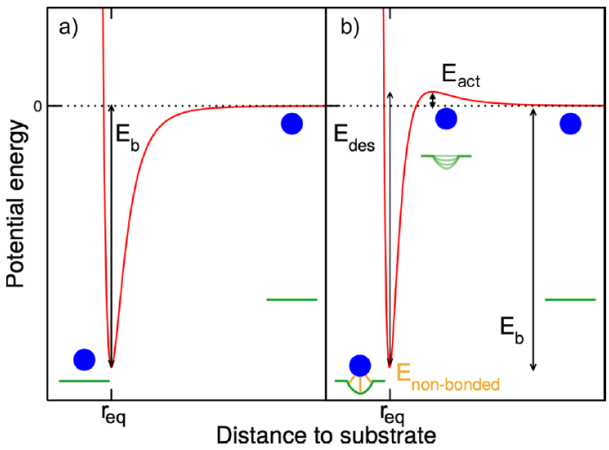

Figure 1.5: A schematic illustration of physisorption (a) and chemisorption (b). The adsorbate is represented by the blue sphere, and the substrate is shown as the green line. In physisorption, the desorption energy corresponds to the depth of the potential well, E_b. In chemisorption, there may be an additional activation energy. The binding energy is sometimes approximated as the sum of non-binding interactions between the adsorbate and the surface. *Source:Minissale et al. (2022)*

The rate constant for adsorption can be given as:

$$k_{ads} = S\sigma < v > . \tag{1.15}$$

Here, S is the sticking probability which tells us the probability that a species is adsorbed during a collision with the dust grain, $\sigma = \pi a^2$ is the geometrical cross-section of the grain assuming a spherical grain with radius a, and $v = \sqrt{\frac{8k_BT_{gas}}{\pi m}}$ is the average thermal speed of a species. Here k_B is the Boltzmann constant, T_{gas} is the gas temperature and m is the mass of the species.

Surface Mobility and Reaction Mechanisms

Once adsorbed, depending on the dust temperature, species can move across the grain surface to encounter and react with other species (Fig. 1.6). This movement is called **diffusion**. Reactions occurring as a result of diffusion of species are called the **Langmuir-Hinshelwood (LH)** reactions. Alternatively, gaseous species can directly collide with species on the dust grain, initiating reactions through a process known as the **Eley-Rideal (ER)** mechanism.

The mobility of species is crucial in the LH mechanism and grain-surface chemistry in general. To migrate from one site to another, a species needs a certain amount of energy, known as diffusion energy (E_{diff}), the height of the potential barrier between two adjacent sites. The motion of a species from one site to another can be described as a hopping motion. The timescale of this hopping motion, t_{hop}, can be expressed as:

$$t_{hop} = \nu_0^{-1} exp\left(\frac{E_{diff}}{k_B T_g}\right) \tag{1.16}$$

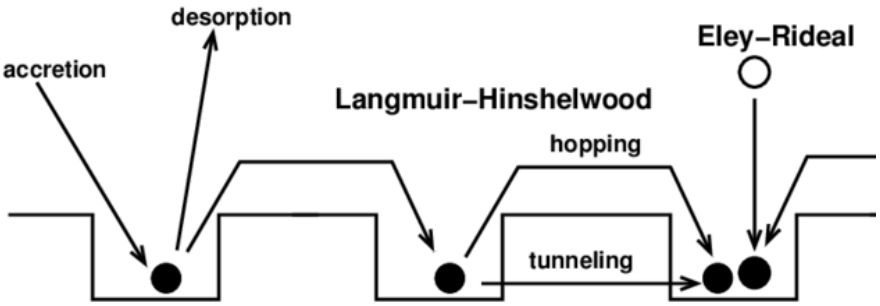

Figure 1.6: Schematic of various surface processes. *Source: Ioppolo (2010)*

where ν_0 is the vibrational frequency of the adsorbed species in the potential well and T_g is the grain temperature. Following Hasegawa et al. (1992), and using the harmonic oscillator approximation, we can estimate ν_0 by

$$\nu_0 = \left(\frac{2N_s E_{des}}{\pi^2 m}\right) \tag{1.17}$$

where N_s is the density of binding sites on the grain surface ($\approx 1.5 \times 10^{15}$ cm^{-2}) and E_{des} is the desorption energy (to be discussed in the following section) of the species of the grain. For light species such as hydrogen and deuterium, quantum tunnelling plays a significant role in their migration between two sites. These species can move from one site to another by tunnelling through the potential barrier that separates them (Hasegawa & Herbst 1993). For a one-dimensional rectangular barrier of width a and height E_{barr}, the tunnelling timescale through the barrier is given as

$$t_{tunn} = \nu_0^{-1} exp\left[\frac{-2a}{\hbar}(2mE_{barr})^{\frac{1}{2}}\right] \tag{1.18}$$

Here $\hbar = \frac{h}{2\pi}$ is the reduced Planck constant. At 10 K, assuming barrier width $a = 1$Å, the timescale for tunnelling through the potential barrier between two sites for an H atom is typically $\approx 10^{-4}$ s, whereas the hopping timescale at the same temperature can be as short as 10^{-3} s. Therefore, quantum tunnelling occurs much faster than hopping at these low temperatures and thus plays an important role in regulating the chemistry. The rate constant of tunnelling can be defined as

$$k_{tunn} = exp\left[\frac{-2a}{\hbar}(2mE_{barr})^{\frac{1}{2}}\right]. \tag{1.19}$$

At very low temperatures ($\approx$ 10 K), most heavier atoms (C, O, N, etc.) and molecules have very low mobilities, except hydrogen and deuterium. Hence, it is usually assumed that the heavier species remain at their sites until an H atom approaches. At these temperatures, hydrogenation reactions play a crucial role in gas-grain reactions.

From the hopping timescale defined in Eq. 1.16, we can estimate the timescale for a species to scan every site on a grain surface. This timescale is called the diffusion timescale. It is defined as:

$$t_{diff} = t_{hop} n_s \tag{1.20}$$

where n_s represents the number of sites on the grain surface. Assuming the grain is spherical, this number is related to the grain radius, a_g, and density of surface sites, N_s, as follows:

$$n_s = N_s 4\pi a_g^2. \tag{1.21}$$

For two species, j and k, moving on the surface of a grain, the rate constant for reactions between them can be given as

$$k_{jk} = \frac{\alpha \kappa_{jk} \left(R_j^{diff} + R_k^{diff} \right)}{n_g} \tag{1.22}$$

Here, α represents the branching ratio of the reaction, and κ_{jk} is the efficiency of the reaction. For exothermic reactions without an activation barrier, κ_{jk} is equal to unity. For reactions with an activation barrier, κ_{jk} varies as *exp (-E_a/T_{dust})*, where E_a is the activation energy of the reaction. R^{diff} is the thermal diffusion rate for a species and is given by

$$R_j^{diff} = \frac{\nu_0}{n_s} exp\left(\frac{-E_{diff,j}}{T_g} \right) \tag{1.23}$$

The ratio of E_{diff}/E_{des} dictates the surface mobility of a species. Astrochemical models typically express $E_{diff} = f\, E_{des}$, where f is a fraction assumed to be constant for all adsorbed species. Most models adopt values for f between 0.3 and 0.7 (Hasegawa et al. 1992; Ruffle & Herbst 2000; Vasyunin & Herbst 2013; Riedel et al. 2023). Recent experiments by Furuya et al. (2022) demonstrated that this fraction can vary depending on the adsorbed species, with f values as low as 0.2. Hence, there is a critical need for more experimental data to better constrain this parameter.

Desorption

Species adsorbed on grain surfaces can return to the gas phase through a process known as **desorption**, which requires energy, referred to as the **desorption energy (E_{des})**. For physisorption, the desorption energy approximately equals the binding energy with the surface (Fig. 1.5a). For chemisorption, additional energy is needed to overcome the dynamical barrier due to the formation of chemical bonds between the surface and the adsorbed species (Fig. 1.5b).

Desorption can occur through thermal or non-thermal mechanisms. A species is desorbed thermally when it gains sufficient thermal energy from the dust grain to overcome its binding energy with the grain. The thermal desorption rate constant per molecule or atom from the grain surface is given by:

$$k_{td} = \nu_0 \, exp\left(-E_{des}/k_B T_g\right), \tag{1.24}$$

where ν_0 - the pre-exponential factor - is the vibrational frequency of the atom or molecule perpendicular to the surface. Based on eq. 1.17, its value is of the order of 10^{12} - 10^{13} s^{-1} for most species in the ISM. Both E_{des} and ν_0 are determined experimentally or *via* computational methods. This is discussed in detail in Chapter 2. As the temperature increases, diffusion competes with thermal desorption.

At the low temperatures found in cold clouds, non-thermal desorption mechanisms are necessary for explaining the observed gas-phase abundances of many species. These mechanisms include desorption driven by UV photons, cosmic ray-induced desorption, and reactive desorption. UV photons from the interstellar radiation field can penetrate the outer regions of dense clouds, interacting with ices and causing the desorption of adsorbed species. Within the dense clouds, UV photons are produced when cosmic rays or X-rays collide with H_2. Cosmic-ray induced desorption is a non-thermal mechanism where a cosmic ray impacts a grain, heating it and causing adsorbed species to desorb. This process is further detailed in section 3.2.3. Reactive desorption occurs when the product of an exothermic chemical reaction gains sufficient excess energy to overcome the species-surface bond, resulting in its desorption from the surface. Most theoretical models assume a desorption efficiency of 1 - 10 % for all species, based on the work of (Garrod et al. 2007) and Vasyunin & Herbst (2013). Recent experimental studies (Minissale et al. 2016; Chuang et al. 2018), on the contrary, indicate that the efficiency of reactive desorption varies depending on the specific chemical reaction and the composition of the surface. However, further research is needed to better constrain and understand this mechanism.

1.3 Ammonia

Nitrogen, the fifth most abundant element in the Universe, is crucial to form molecules like amino acids and nucleobases, which are precursors to life. N-bearing molecules have been observed across a variety of regions like diffuse clouds (Liszt & Lucas 2001), dark and dense clouds (Caselli et al. 2002a,b), and protoplanetary disks (Salinas et al. 2016). Complex N-bearing species have been observed towards prestellar cores (Jiménez-Serra et al. 2016; Megías et al. 2023), Class 0 low-mass protostars (Nazari et al. 2021), and the Galactic Centre (Zeng et al. 2018). A significant advantage of N-bearing molecules, such as N_2H^+ and NH_3, is their resistance to gas-phase depletion compared to common tracers like CO (Caselli et al. 2002b; Aikawa et al. 2005; Flower et al. 2006; Bergin & Tafalla 2007; Sipilä et al. 2015). The binding energy of N atoms was found to be slightly lower than expected (Minissale et al. 2016) but well below that of O, CO, and N_2, changing the hierarchy of their volatility, making N atoms more resistant to freezeout. Moreover, the effective binding energy of N_2 is considerably reduced by the presence of CO molecules (Nguyen et al. 2018), which would also make this molecule more resistant to depletion. Therefore, nitrogen-bearing molecules have been crucial molecular tracers of the inner core regions (Bergin et al. 2006; Friesen et al. 2009; Pineda et al. 2010, 2011, 2015; Chitsazzadeh et al. 2014), providing valuable insights into the kinematics and evolution of these sources.

Despite its fundamental role in prebiotic chemistry, many aspects of nitrogen chemistry remain poorly understood. A key unresolved question concerns the elemental partitioning of

nitrogen in the interstellar medium (ISM). In dense clouds and cores, the primary nitrogen reservoirs are atomic nitrogen (N) and molecular nitrogen (N_2); however, how the remaining nitrogen is distributed is not yet well established. One potential reservoir is ammonia (NH_3), which may play a significant role in the nitrogen budget of these environments.

Ammonia is one of the simplest N-bearing molecules. It was the first polyatomic molecule detected in the ISM by Cheung et al. (1968) through its $(J,K) = (1,1)$ inversion transition towards the Galactic Centre. Ammonia has been widely observed in a variety of environments including molecular clouds (Irvine et al. 1987), prestellar cores (Crapsi et al. 2007), the Galactic Centre (Winnewisser et al. 1979), diffuse clouds (Liszt et al. 2006), galaxies (Sandqvist et al. 2017; Gorski et al. 2018), star-forming regions (Fehér et al. 2022), comets (Poch et al. 2020), and planet-forming disks (Salinas et al. 2016). It is one of the six major molecules found in interstellar ices in the solid form (Boogert et al. 2015). Ammonia is also a robust temperature probe in molecular clouds making it a valuable tracer for dense gas (Ho & Townes 1983; Walmsley & Ungerechts 1983; Maret et al. 2009).

The molecule has a trigonal pyramidal structure (Fig. 1.7), with one nitrogen atom covalently bonded to three hydrogen atoms. The nitrogen atom carries a lone pair of electrons, which repels the bonding electron pairs of the hydrogen atoms. This repulsion results in a bond angle of approximately ≈107° instead of the expected 109.5° for a regular tetrahedral arrangement. This structural configuration imparts a dipole moment to the molecule, rendering it polar and, consequently, observable using its rotational spectra.

The rotational dynamics of ammonia is characterised by two quantum numbers, J and K, denoting the total angular momentum and the projection of the total angular momentum on the principal molecular axis, respectively. Transitions of the form J > K, for a given K, occur rapidly (within 10 - 100 seconds) through far-infrared $\Delta J = 1$ transitions, and are denoted as nonmetastable. On the other hand, transitions of the form J = K, termed metastable, are stimulated by collisions rather than radiation. Hence, the population ratio between two states serves as an accurate indicator of the gas kinetic temperature, T_K.

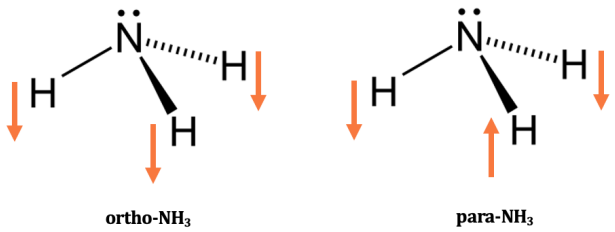

Figure 1.7: Ortho- and para- spin configurations of ammonia.

Ammonia exists in two distinct forms (Fig. 1.7) determined by the orientation of the hydrogen atoms: the ortho-state (K = 3n, where n is an integer) and the para-state (K ≠ 3n). In the ortho-state, all hydrogen atoms have parallel spins. In contrast, the para-state has hydrogen atoms with non-parallel spins. For example, the $(J,K) = (0,0)$, (1,1), (2,2) and (4,4) are examples of para-states while (3,3) and (6,6) are examples of the ortho-state (Fig. 1.8). Interconversion between the ortho- and para-states in the gas phase typically does not

occur through normal radiative or collisional transitions. However, reactive collisions with protons and protonated species can cause mixing of ortho- and para-species by scrambling protons within the reaction complex. These interconversion processes are nearly thermoneutral, implying they proceed more slowly compared to exothermic reactive pathways. The rotational temperature between ortho- and para-species, known as the spin temperature, is crucial for determining the formation temperature of ammonia.

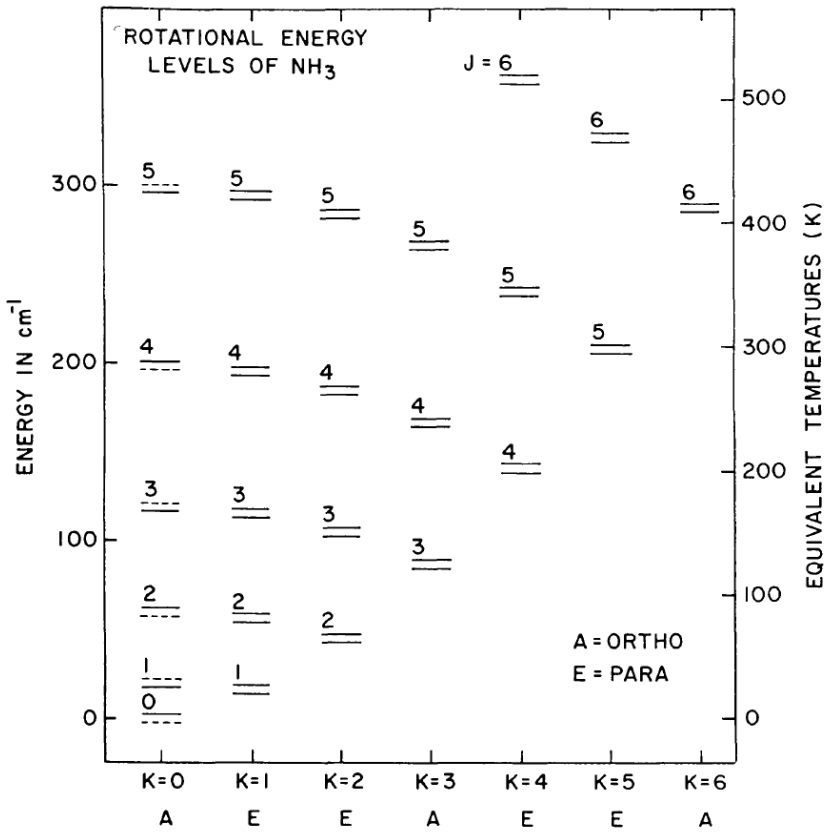

Figure 1.8: Energy level diagram of the rotational inversion states of NH_3. Here, J represents the total angular momentum quantum number, and K denotes the projection of the total angular momentum on the principal molecular axis. Each (J,K) level is split into doublets due to the quantum mechanical tunnelling of the N atom through the plane of the hydrogen atoms. *Source: Ho & Townes (1983)*

The nitrogen atom can quantum mechanically tunnel through the plane of the hydrogen atoms due to a low potential barrier of around 24.7 kJ/mol leading to the inversion of the molecule. This tunnelling causes the spin of the nitrogen nucleus to align either parallel or anti-parallel to the geometry of the molecule resulting in the splitting of each (J,K) energy level into doublets (Fig. 1.8). These lines are closely spaced allowing the telescope-receiver combination to be used in observations for sources with similar beam sizes, minimising calibration uncertainties in measured line ratios. These inversion doublets are further split into multiple components, known as hyperfine transitions. This additional splitting occurs due to the interaction between the electric quadrupole moment of the nitrogen nucleus and

the electric field gradient created by the surrounding electrons, as well as due to weaker magnetic interactions from the 3 H nuclei. For example, the (1,1) inversion line of ammonia has 18 hyperfine components (Fig. 1.9), and the (2,2) line features a total of 21 components, and so on.

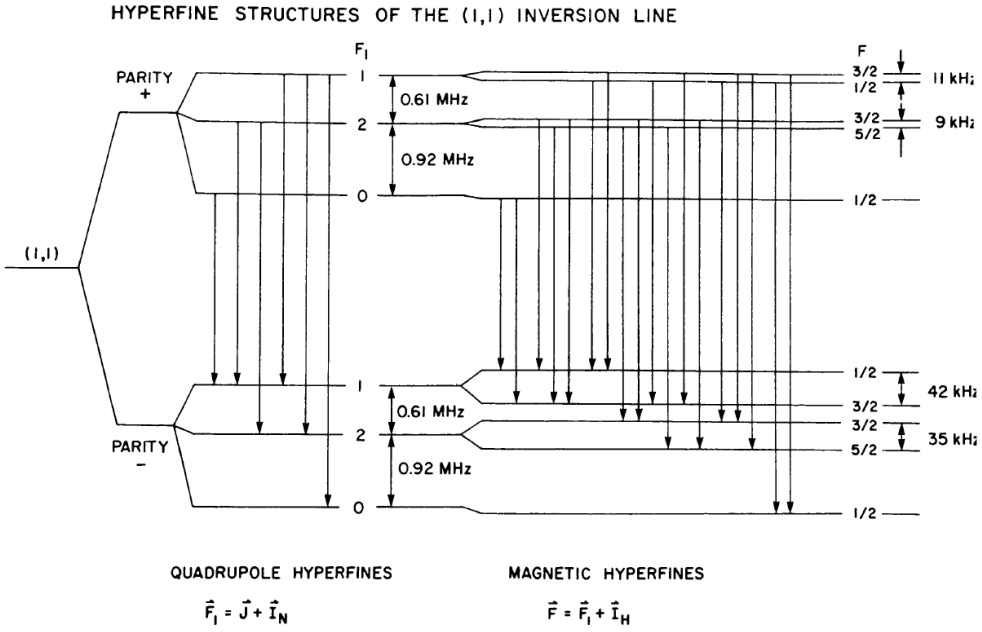

Figure 1.9: Hyperfine levels of the (J,K) = (1,1) of NH_3 showing the inversion doublets, quadrupole, and magnetic hyperfine components. *Source: Ho & Townes (1983)*

This molecule serves as an invaluable tool for probing the interstellar medium, thanks to its distinctive properties discussed above. These include the presence of metastable and nonmetastable states, ortho- and para-species, inversion motion, and hyperfine structures, all of which can be used to derive the physical and chemical conditions of various regions within the ISM.

1.4 Radiative Transfer

This section is based on the derivation from Mangum & Shirley (2015)

Information about the various phenomena in the ISM is communicated to observers *via* electromagnetic radiation. As the radiation travels through space, it undergoes absorption, emission and scattering by the atoms and molecules in the medium between the Earth and the source. To accurately interpret observational data, radiative transfer models are essential. By integrating these models with predictions from astrochemical models (discussed in section 3.1.1), astronomers can predict the detectability of specific species, improving our understanding of the physical properties of astrophysical objects. In the present work, we will adopt a similar approach in chapter 3 to verify the detectability of our results of ammonia.

This section will explain the fundamental theory of radiative transfer necessary to understand how this is achieved.

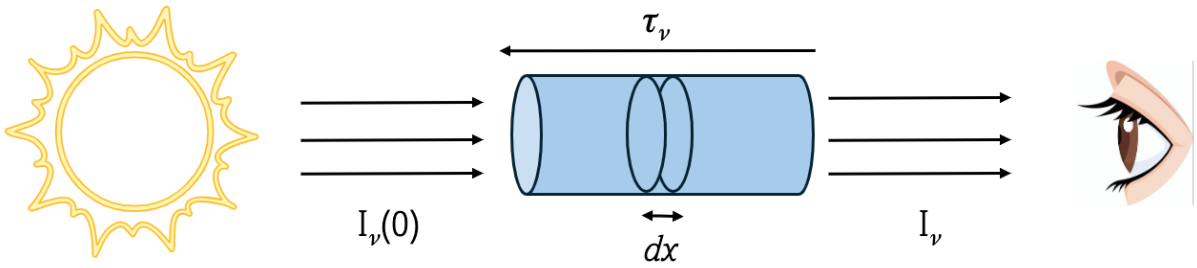

Figure 1.10: Schematic representing the variation in intensity of radiation from a source, $I_\nu(0)$, to the observed intensity, I_ν, after passing through a column of material of length, dx.

The intensity of radiation that reaches the Earth after interaction with the ISM between the observer and the source can mathematically be described by the radiative transfer equation:

$$\frac{dI_\nu}{dx} = -\alpha_\nu I_\nu + j_\nu \,. \tag{1.25}$$

Equation 1.25 gives the change in intensity, dI_ν, of light of a given frequency ν from a source after propagation through an infinitesimal length, dx, through a medium. Here, α_ν is the absorption constant and j_ν is the emissivity. Since the propagation path of the radiation is usually unknown, the quantity τ_ν, called the optical depth is used instead which is defined as

$$d\tau_\nu = -\alpha_\nu dx \,. \tag{1.26}$$

The radiative transfer equation then becomes,

$$dI_\nu = S_\nu d\tau_\nu - I_\nu d\tau_\nu \,, \tag{1.27}$$

where S_ν is the source function defined as

$$S_\nu = \frac{j_\nu}{\alpha_\nu} \,. \tag{1.28}$$

Multiplying both sides of eq. 1.27 by e^{τ_ν} and integrating from $\tau_\nu = 0$ and $I_\nu = I_\nu(0)$ along the line of sight, we get the intensity (I_ν) measured by the observer

$$I_\nu = I_\nu(0)e^{-\tau_\nu} + \int_0^{\tau'} exp[-(\tau_\nu - \tau')]S_\nu \, d\tau' \,. \tag{1.29}$$

The first term in this equation gives the background intensity $I_\nu(0)$ attenuated by the medium between the source and the observer by a factor $e^{-\tau_\nu}$. The second term is the integrated

emission, $S_\nu d\tau'$, attenuated by the medium between the observer and the point of emission by a factor $exp[-(\tau_\nu - \tau')]$.

Assuming the medium to be infinitely optically thick and behaving like a blackbody, then $I_\nu = B_\nu$. If the medium is physically and chemically uniform with a temperature, T_{ex}, along the line of sight. This means that the source function remains constant. Then, from eq. 1.27,

$$0 = dI_\nu = S_\nu d\tau_\nu - B_\nu d\tau_\nu \,, \tag{1.30}$$

i.e., the source function is equal to the Planck function, that is, $S_\nu = B_\nu(T_{ex})$ at T_{ex}. Here, T_{ex} is the excitation temperature which is defined as

$$T_{ex} = \frac{\frac{h\nu}{k}}{ln(\frac{n_l g_u}{n_u g_l})} \,, \tag{1.31}$$

and n is the population in the upper (u) and lower (l) energy levels for a transition with frequency ν. If we consider T_{ex} to be constant, eq. 1.29 becomes

$$I_\nu = I_\nu(0)e^{-\tau_\nu} + B_\nu(T_{ex})[1 - e^{-\tau_\nu}] \,. \tag{1.32}$$

When the medium is optically thick, i.e., $\tau \gg 1$, eq. 1.32 implies that

$$I_\nu = B_\nu(T_{ex}) \,. \tag{1.33}$$

This means that the observed intensity is from the source function of the medium itself, which, under the earlier assumption, resembles a blackbody spectrum since the incident intensity does not penetrate the medium.

When the medium is optically thin, i.e., $\tau \ll 1$, and applying a Taylor expansion of the exponent in eq. 1.32, we have the following scenarios:

1. When the background intensity is negligible, ($I_\nu(0) \rightarrow 0$)

$$I_\nu = \tau_\nu B_\nu(T_{ex}) \tag{1.34}$$

2. When the background intensity is significant

$$I_\nu = I_\nu(0) + \tau(B_\nu(T_{ex}) - I_\nu(0)) \tag{1.35}$$

If $I_\nu(0) > B_\nu(T_{ex})$, the intensity observed is reduced. Conversely, if $I_\nu(0) < B_\nu(T_{ex})$, intensity is added to the radiation we observe.

The intensity we observe from molecular line measurements is the difference between the background intensity, $B_\nu(T_{bg})$ and radiation from the source. Hence:

$$\Delta I_\nu = I_\nu - I_\nu(0) = [B_\nu(T_{ex}) - B_\nu(T_{bg})][1 - e^{-\tau_\nu}]. \tag{1.36}$$

If we replace the specific intensity I_ν with Rayleigh-Jeans equivalent temperature which is the equivalent temperature of a blackbody at temperature T,

$$J_\nu(T) = \frac{\frac{h\nu}{k}}{exp(\frac{h\nu}{kT}) - 1}, \tag{1.37}$$

and introduce the concept of brightness temperature, T_B, which is the equivalent temperature that a black body would have in order to emit the radiation intensity ΔI_ν, where

$$T_B = \frac{c^2}{2k\nu^2}\Delta I_\nu. \tag{1.38}$$

$B_\nu(T)$ can be related to $J_\nu(T)$ as

$$\frac{c^2}{2k\nu^2}B_\nu(T) = J_\nu(T) \tag{1.39}$$

Then the radiative transfer equation can be expressed in terms of the brightness temperature as follows

$$T_B = f[J_\nu(T_{ex}) - J_\nu(T_{bg})][1 - exp(-\tau_\nu)] \tag{1.40}$$

where f is the beam-filling factor which is the fraction of the beam solid angle of telescope antenna filled by the source solid angle.

To understand the structure of a source and the interstellar medium better, it is important to obtain parameters such as molecular abundances, density, and kinetic temperature. The column density is an essential quantity that can be used to derive these physical conditions. The column density is simply the number of molecules per unit area along the line of sight. It can be expressed as the number of molecules in an energy level u integrated over the pathlength ds:

$$N_u = \int n_u ds. \tag{1.41}$$

The column density and the optical depth can be related to each other by

$$N_u = \frac{3h}{8\pi^3|\mu_{lu}|^2}\left[exp\left(\frac{h\nu}{kT}\right) - 1\right]^{-1}\int \tau_\nu dv, \tag{1.42}$$

where the conversion $\frac{d\nu}{\nu} = \frac{dv}{c}$ has been applied to switch from frequency units to velocity. The full derivation can be found in Mangum & Shirley (2015). Equation 1.42 gives us the

expression for the column density of emission for molecules in the upper transition state u. The quantity $|\mu_{lu}|^2$ is the dipole matrix element for transition from the upper energy state u to a lower energy state l. Now, using N_u, we can calculate the total population of all energy levels in the molecule, N_{tot}, using the expression

$$\frac{N_{tot}}{N_u} = \frac{Q_{rot}}{g_u} exp\left(\frac{E_u}{kT_{ex}}\right). \tag{1.43}$$

The quantity Q_{rot} is the rotational partition function and describes the statistical sum over all rotational energy levels in the molecule and, g_u is the degeneracy of the energy level u. Substituting eq. 1.42 in eq. 1.43, we get the following expression for N_{tot}

$$N_{tot} = \frac{3h}{8\pi^3|\mu_{lu}|^2} \frac{Q_{rot}}{g_u} exp\left(\frac{E_u}{kT_{ex}}\right) \left[exp\left(\frac{h\nu}{kT}\right) - 1\right]^{-1} \int \tau_\nu dv. \tag{1.44}$$

As previously mentioned, radiative transfer models are powerful tools to understand the relationship between the observed emission from a source and its physical conditions. These models can, conversely, evaluate the observability of emission (for example, by simulating emission lines, column densities, etc) based on a specific set of initial conditions. This latter approach will be used in the present work.

1.5 Thesis Content

With the necessary background established, the next chapters will present the results of our research, which are obtained through experimental and numerical modelling approaches. A brief summary of each chapter is provided below:

1. **Chapter 2** examines the desorption behaviour of ammonia in mixed ices, determines its binding energy on various water ice substrates, and assesses the overall impact on the ammonia snowline using an experimental approach.
2. **Chapter 3** discusses the application of the experimentally determined binding energy values in models of pre- and protostellar cores. The impact of varying binding energy on the chemistry and evolution of these sources is examined using gas-grain astrochemical networks and radiative transfer modelling.
3. **Chapter 4** investigates the formation of ammonia on cold surfaces through the successive hydrogenation of nitrogen atoms, integrating both experimental methods and gas-grain modeling approaches.
4. **Chapter 5** provides a brief summary of the research presented in this thesis and explores future prospects and potential directions for further investigation.

Bibliography

Aikawa, Y., Herbst, E., Roberts, H., & Caselli, P. 2005, The Astrophysical Journal, 620, 330

Bergin, E. A., Maret, S., van der Tak, F. F., et al. 2006, , 645, 369

Bergin, E. A. & Tafalla, M. 2007, Annu. Rev. Astron. Astrophys., 45, 339

Boogert, A. A., Gerakines, P. A., & Whittet, D. C. 2015, Annual Review of Astronomy and Astrophysics, 53, 541

Burke, D. J. & Brown, W. A. 2010, Physical Chemistry Chemical Physics, 12, 5947

Caselli, P., Benson, P. J., Myers, P. C., & Tafalla, M. 2002a, The Astrophysical Journal, 572, 238

Caselli, P., Walmsley, C., Zucconi, A., et al. 2002b, The Astrophysical Journal, 565, 344

Cazaux, S., Tielens, A., Ceccarelli, C., et al. 2003, The Astrophysical Journal, 593, L51

Cheung, A., Rank, D. M., Townes, C., Thornton, D. D., & Welch, W. 1968, Physical Review Letters, 21, 1701

Chitsazzadeh, S., Di Francesco, J., Schnee, S., et al. 2014, , 790, 129

Chuang, K. J., Fedoseev, G., Qasim, D., et al. 2018, , 853, 102

Crapsi, A., Caselli, P., Walmsley, M. C., & Tafalla, M. 2007, Astronomy & Astrophysics, 470, 221

Draine, B. T. 1978, Astrophysical Journal Supplement Series, vol. 36, Apr. 1978, p. 595-619., 36, 595

Fehér, O., Tóth, L. V., Kraus, A., et al. 2022, The Astrophysical Journal Supplement Series, 258, 17

Flower, D. R., Pineau Des Forêts, G., & Walmsley, C. M. 2006, , 456, 215

Friesen, R., Di Francesco, J., Shirley, Y., & Myers, P. 2009, The Astrophysical Journal, 697, 1457

Furuya, K., Hama, T., Oba, Y., et al. 2022, The Astrophysical Journal Letters, 933, L16

Garrod, R. T., Wakelam, V., & Herbst, E. 2007, Astronomy & Astrophysics, 467, 1103

Gorski, M., Ott, J., Rand, R., et al. 2018, The Astrophysical Journal, 856, 134

Habing, H. 1968, Bulletin of the Astronomical Institutes of the Netherlands, Vol. 19, p. 421, 19, 421

Hasegawa, T. I. & Herbst, E. 1993, Monthly Notices of the Royal Astronomical Society, 261, 83

Hasegawa, T. I., Herbst, E., & Leung, C. M. 1992, , 82, 167

Ho, P. T. & Townes, C. H. 1983, Annual Review of Astronomy and Astrophysics, 21, 239

Ioppolo, S. 2010, PhD thesis, Universiteit Leiden, surface formation routes of interstellar molecules: a laboratory study

Irvine, W., Goldsmith, P., Hjalmarson, Å., Hollenbach, D., & Thronson, H. 1987, Reidel Dordrecht, 561

Jessberger, E. K., Stephan, T., Rost, D., et al. 2001, in Interplanetary dust (Springer), 253–294

Jiménez-Serra, I., Vasyunin, A. I., Caselli, P., et al. 2016, The Astrophysical Journal Letters, 830, L6

Keto, E. & Caselli, P. 2008, The Astrophysical Journal, 683, 238

Larson, R. B. 1969, Monthly Notices of the Royal Astronomical Society, 145, 271

Liszt, H. & Lucas, R. 2001, Astronomy & Astrophysics, 370, 576

Liszt, H., Lucas, R., & Pety, J. 2006, Astronomy & Astrophysics, 448, 253

Mangum, J. G. & Shirley, Y. L. 2015, Publications of the Astronomical Society of the Pacific, 127, 266

Maret, S., Faure, A., Scifoni, E., & Wiesenfeld, L. 2009, Monthly Notices of the Royal Astronomical Society, 399, 425

Megías, A., Jiménez-Serra, I., Martín-Pintado, J., et al. 2023, Monthly Notices of the Royal Astronomical Society, 519, 1601

Minissale, M., Aikawa, Y., Bergin, E., et al. 2022, ACS Earth and Space Chemistry, 6, 597

Minissale, M., Congiu, E., & Dulieu, F. 2016, Astronomy & Astrophysics, 585, A146

Minissale, M., Dulieu, F., Cazaux, S., & Hocuk, S. 2016, , 585, A24

Nazari, P., van Gelder, M., Van Dishoeck, E., et al. 2021, Astronomy & Astrophysics, 650, A150

Nguyen, T., Baouche, S., Congiu, E., et al. 2018, Astronomy & Astrophysics, 619, A111

Öberg, K. I. & Bergin, E. A. 2021, Physics Reports, 893, 1

Pagani, L., Bacmann, A., Cabrit, S., & Vastel, C. 2007, , 467, 179

Persson, M. V. 2014, SEDs of the different protostellar evolutionary stages.

Pineda, J. E., Goodman, A. A., Arce, H. G., et al. 2010, The Astrophysical Journal Letters, 712, L116

Pineda, J. E., Goodman, A. A., Arce, H. G., et al. 2011, The Astrophysical Journal Letters, 739, L2

Pineda, J. E., Offner, S. S., Parker, R. J., et al. 2015, Nature, 518, 213

Poch, O., Istiqomah, I., Quirico, E., et al. 2020, Science, 367, eaaw7462

Riedel, W., Sipilä, O., Redaelli, E., et al. 2023, Astronomy & Astrophysics, 680, A87

Robitaille, T. P. & Whitney, B. A. 2010, The Astrophysical Journal Letters, 710, L11

Ruffle, D. P. & Herbst, E. 2000, Monthly Notices of the Royal Astronomical Society, 319, 837

Sahoo, S. 2016, Episodic Accretion in V2493 Cyg.

Salinas, V. N., Hogerheijde, M. R., Bergin, E. A., et al. 2016, Astronomy & Astrophysics, 591, A122

Sandqvist, A., Hjalmarson, Å., Frisk, U., et al. 2017, Astronomy & Astrophysics, 599, A135

Shannon, R. J., Blitz, M. A., Goddard, A., & Heard, D. E. 2013, Nature chemistry, 5, 745

Sipilä, O., Harju, J., Caselli, P., & Schlemmer, S. 2015, , 581, A122

Vasyunin, A. & Herbst, E. 2013, The Astrophysical Journal, 769, 34

Walmsley, C. & Ungerechts, H. 1983, Astronomy and Astrophysics (ISSN 0004-6361), vol. 122, no. 1-2, June 1983, p. 164-170., 122, 164

Winnewisser, G., Churchwell, E., & Walmsley, C. 1979, Astronomy and Astrophysics, vol. 72, no. 1-2, Feb. 1979, p. 215-223., 72, 215

Zeng, S., Jiménez-Serra, I., Rivilla, V., et al. 2018, Monthly Notices of the Royal Astronomical Society, 478, 2962

2

Experimental study of the binding energy of NH_3 on different types of ice and its impact on the snow line of NH_3 and H_2O

The contents of this chapter are published in *Astronomy & Astrophysics*: Kakkenpara Suresh et al. (2024).

2.1 Introduction

N-bearing molecules, as previously discussed, are considered to be excellent tracers of dense and cold interstellar regions. Recent work using multi-transition studies done with the IRAM 30m antenna and high sensitivity interferometric observations with ALMA and JVLA have shown that these molecules freeze out within the central region of pre-stellar cores (e.g. Redaelli et al. 2019; Caselli et al. 2022; Pineda et al. 2022), although at higher densities than CO. Gas-grain astrochemical models are able to reproduce the observations (Caselli et al. 2022; Pineda et al. 2022). Still, they are limited by uncertainties in such factors as the binding energies of NH_3 and knowledge of its surface chemistry. Following the work of Collings et al. (2004), Penteado et al. (2017) derived binding energies for several species, including NH_3. Similarly, Collings et al. (2004), He et al. (2016), and Suhasaria et al. (2015) have studied the desorption properties of NH_3 from various substrates. However, the binding energies of NH_3, the importance of surface chemistry for its formation, and its chemical desorption efficiency (Caselli et al. 2017; Sipilä et al. 2019) are still not well constrained, highlighting the need for further investigation.

Kruczkiewicz et al. (2021) have shown that ammonia can be efficiently stored in the form

of ammonium salts, which at higher temperatures decompose to release ammonia into the gas phase irrespective of the presence or absence of water. This release into the gas phase occurs at a temperature higher than that of the desorption of water ice (T $\sim$ 154 K) but lower than room temperature. This implies that ammonia could remain on grains closer to a young stellar object than the water snow line. The majority of NH_3 in the ice mantles should therefore be free to interact with the major components of interstellar or cometary ices such as water, CO_2, or CO. Similarly, Poch et al. (2020) have demonstrated that ammonium salts are a dominant nitrogen reservoir on cometary surfaces, explaining the low measured cometary nitrogen-to-carbon ratio as compared to that of the Sun. Finally, as ammonia ice is one of the major nitrogen reservoirs in star-forming regions (Öberg et al. 2011), knowledge of the ammonia snow line is crucial when considering the formation and evolution of more complex N-bearing species in planetary systems.

The aim of the work in this chapter is to experimentally study the behaviour of ammonia in the presence of different components of molecular ice mantles, such as H_2O, CO, and CO_2. The binding energy of ammonia on different water ice substrates, namely, compact amorphous solid water ice (c-ASW) and crystalline ice (CI) are also obtained. Additionally, experiments are performed to determine the snow line of ammonia. The chapter is organised as follows: Section 2.2 describes the experimental set-up; Section 2.3 details the experiments and the results; Section 2.4 discusses the conclusion and future prospects.

2.2 Experimental Set-up and Methods

The experiments are conducted on the multi-beam Ultra High Vacuum (UHV) setup VENUS (VErs des NoUvelles Syntheses), which simulates the physical conditions found in cold molecular clouds (Congiu et al. 2020). This setup is located at LERMA (Laboratoire d'Étude du Rayonnement et de la Matière en Astrophysique et Atmosphèrique) at the CY Cergy Paris University. VENUS is designed to study astrochemically relevant surface reactions via non-energetic processes under low temperature and pressure conditions similar to those in the ISM. It is suitable for studying both very thin layers (from submonolayer to one monolayer) and thick layers of pure and mixed ices. The setup (Fig. 2.1) is comprised of different components:

1. An Ultra High Vacuum (UHV) chamber called the *main chamber*
2. A sample holder attached to a cryostat, mounted in the main chamber
3. A Quadrupole Mass Spectrometer (QMS) within the main chamber
4. A Fourier Transform Reflection Absorption Infrared Spectrometer (FT-RAIRS)
5. Four seperate beamlines to inject species onto the sample holder
6. An intermediary stage between each beamline and the main chamber, consisting of two chambers (Ch1 and Ch2)

In the following sections, each of these components will be described in detail.

2.2.1 The Main Chamber

VENUS consists of a stainless steel UHV chamber (Fig. 2.1, henceforth referred to as the main chamber) which can reach a base pressure of up to a few 10^{-10} mbar *via* differential pumping. Such low pressures are attained using a turbo-molecular pump connected to the main chamber, with the pressure stability monitored by a cold cathode gauge. The accretion time of typical pollutants (H_2, H_2O, CO) at this pressure is much longer than the duration of an average experiment. For instance, forming 1 ML[1] of water ice at these pressures takes around 5000 minutes (≈83 hours, Accolla 2010). Similarly, it takes about 2.5 hours to accrete 1ML H_2 on the surface (assuming a surface site density of approximately $\sim 10^{15}$ cm^{-2} and a collision rate of 10^{11} molec cm^{-2} s^{-1}) (Woodruff 2016). Therefore, experiments can be performed on a clean surface with the contamination amounting to only a few percent of a monolayer.

Depositions are made on a gold-coated copper sample holder within the main chamber. The sample holder is attached to the cold finger of closed-cycle He cryostat. The temperature of the sample holder can be varied between 7 and 400 K via a computer-controlled resistive heater. The gold surface, approximately 9 mm in diameter, is optically flat, chemically inert, and ensures optimal mid-infrared light reflectance. The cryo-cooler, to which the gold surface is attached, can be moved in and out of the main chamber, as well as horizontally and vertically.

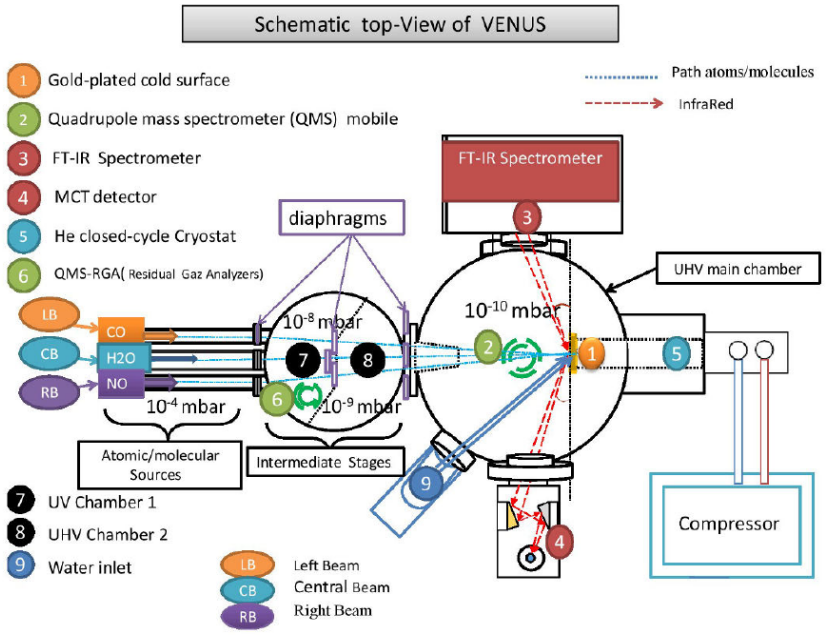

Figure 2.1: Schematic top view of Venus. *Source: Congiu et al. (2020)*

[1]ML = Monolayer, corresponds to 10^{15} molecules/cm^2

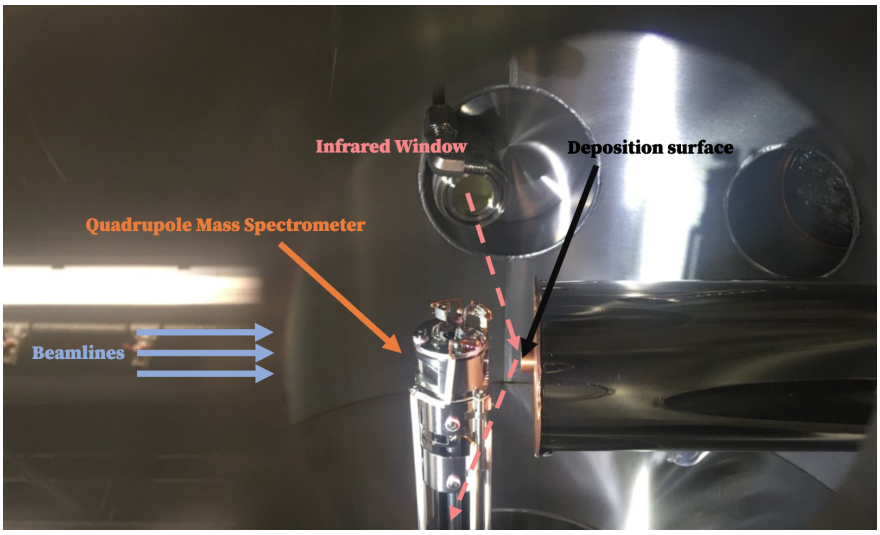

Figure 2.2: Inside view of the main chamber showing the deposition surface, the QMS, the infrared window, and the direction of the incoming gas source. The QMS here is in the "high" position where it is in front of the deposition surface and the beamlines. During deposition, the QMS is lowered to the "low" position to allow the gas to be deposited onto the surface.

2.2.2 The Quadrupole Mass Spectrometer

A Quadrupole Mass Spectrometer (QMS, Hiden 51/3F), mounted at the bottom of the main chamber (Fig. 2.2), is used to probe the composition of the beams and study the species desorbed from the gold substrate during Temperature Programmed Desorption (TPD) experiments. The QMS can be translated vertically or rotated to examine species in the mass range of 1 to 300 amu.

During vertical translation, the QMS can be positioned in either the "low" or "high" position. In the "low" position, the QMS inspects the composition of residual gas species in the main chamber. In the "high" position, it serves two purposes: when positioned in front of the beamline, it probes beam intensity and composition, verifying beam alignment accuracy; when positioned in front of the deposition surface, it records the species desorbed from the surface during TPD. During deposition, the QMS is lowered to the "low" position. The QMS is controlled via software provided by Hiden, allowing control over technical settings such as the energy of the ionising electrons and the dwell time for each mass.

The QMS consists of an ioniser and four parallel cylindrical (or hyperbolic) rods. The incoming gas is ionised by the ioniser through collisions with electrons produced by a hot filament, then moves to the quadrupole rods, which act as a mass analyser, separating the ions based on their mass-to-charge ratio *(m/z)*. This is achieved by applying a voltage to the adjacent and opposite rods such that, for a given voltage, only ions of a specific m/z will reach the QMS detector. The other ions collide along the length of the rods. The voltage is constantly varied, enabling the QMS to scan multiple masses in a short duration of time.

2.2.3 The Beamlines

VENUS consists of five beam lines that serve as gas sources for injecting species into the main chamber. Four of these beam lines (Fig. 2.3) are separated from the main chamber by intermediary chambers, referred to as chambers 1 and 2, which are enclosed in a single stainless steel chamber and divided by an S-shaped wall. The pressures in chambers 1 and 2 are maintained at 10^{-8} mbar and 10^{-9} mbar, respectively by a turbo-molecular pump and closely monitored by a cold cathode gauge.

The beam lines, labelled "top", "bottom", "central", and "right", can be used simultaneously to introduce atoms or molecules into the main chamber. They can reach a pressure of a few 10^{-5} - 10^{-4} mbar and fluxes of 2 x 10^{12} molecules cm^{-2} s^{-1}. This implies that 1 ML can be deposited on the surface in roughly 10 minutes. The beam lines are designed to inject the desired species onto the deposition surface at a rate that maintains the base pressure of 10^{-10} mbar in the main chamber. The flux of gaseous species is controlled by an automated regulator (Bronkhorst High-Tech control valve), ensuring accurately reproducible molecular flows across experiments. A laser beam is used to align each of the beams, ensuring they overlap on the same spot on the deposition surface. The atoms/molecules are at ambient temperature ($\sim$ 300 K) as they travel from the beam line into the main chamber.

The fifth beam line, a UHV leak valve mounted to one of the main chamber windows and connected to a stainless steel gas-handling manifold, is directly connected to the main chamber and can be used to inject molecules or atoms as needed.

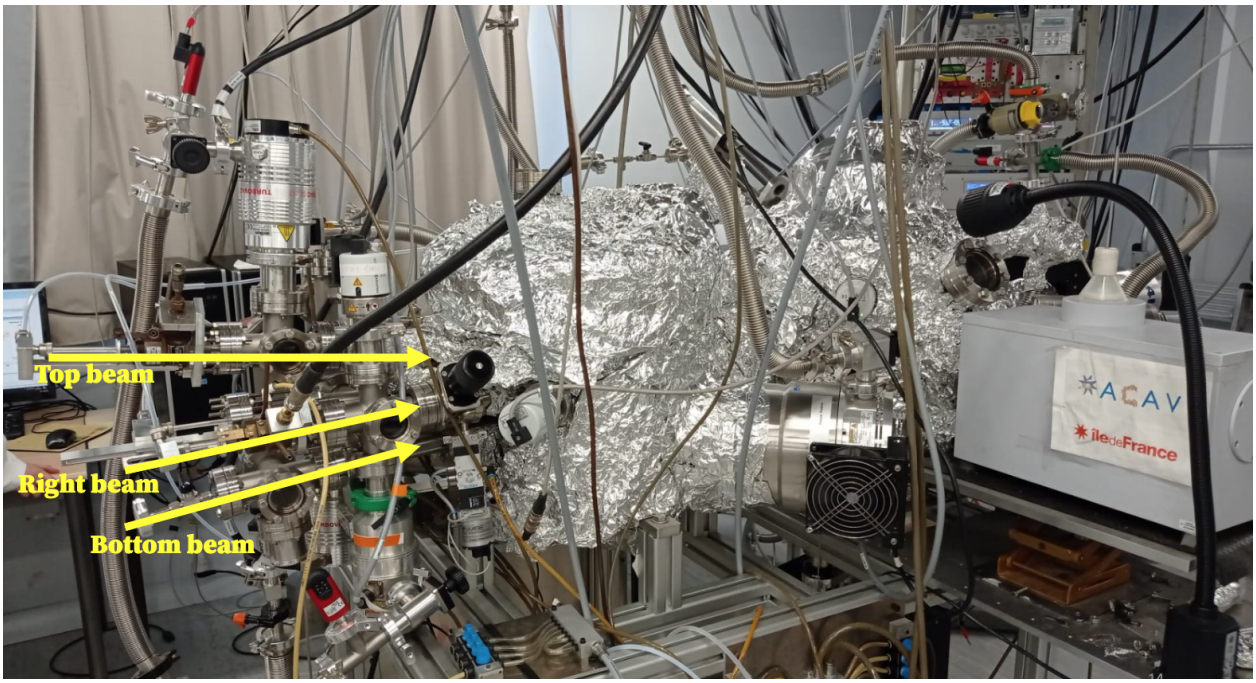

Figure 2.3: Figure showing three of the five beam lines. The central beam is located behind the right beam in this image.

2.2.4 The Infrared Spectrometer

In situ studies of the composition, thickness, and morphology of adsorbed or deposited species are performed by a Bruker Vertex 70v Fourier Transform Reflection Absorption Infrared Spectrometer (FT-RAIRS) attached to the main chamber, which operates in the mid-infrared region (4000–700 cm^{-1} or 2.2–14.3 μm). Combined with the QMS, data from these two instruments provide a more comprehensive understanding of the studied systems than either instrument alone.

A mid-infrared source produces polychromatic infrared radiation, which is focused onto the deposition surface at a grazing angle of 83° using two gold-coated mirrors: a flat mirror and a 90° off-axis parabolic (OAP) mirror (within compartment E1 in Fig. 2.4). After being reflected off the gold substrate (which acts as a flat mirror), the infrared beam enters a second compartment (E2), where another 400 mm OAP mirror collects the infrared light coming from the sample. This light is then focused onto the sensor element of a liquid-nitrogen-cooled mercury cadmium telluride (MCT) detector using a 43 mm OAP mirror.

The spectrometer and the two compartments (E1 and E2) are differentially pumped using a dry scroll pump to maintain pressures at roughly 10^{-2} mbar. The MCT detector collects the raw data, which is then converted into an analysable IR spectrum using Fourier transforms through the OPUS software. The acquisition time for a spectrum is roughly 2 minutes, with an average of 256 scans per spectrum and a typical resolution of 4 cm^{-1}. Spectra can be obtained prior to, during, or after deposition or TPD experiments.

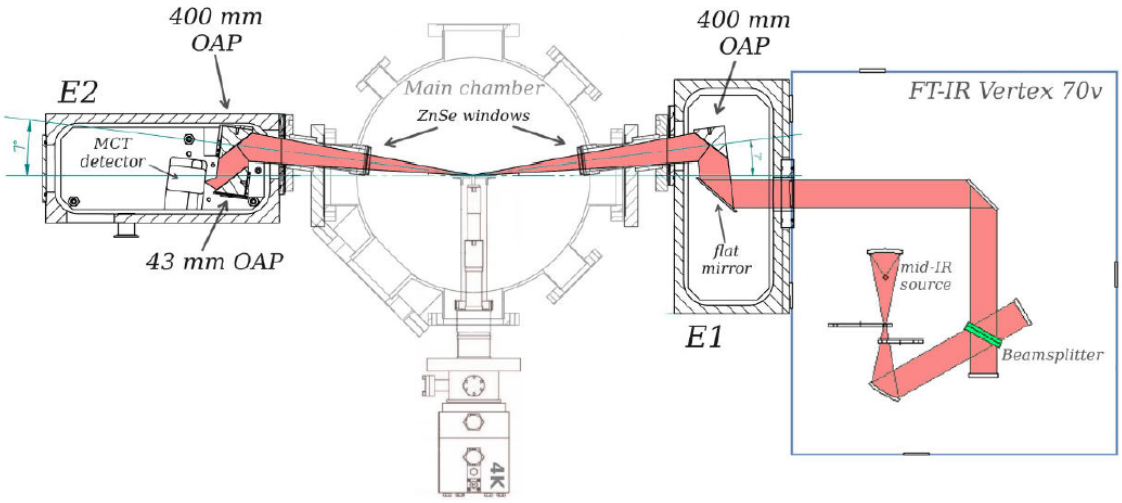

Figure 2.4: Schematic of the FT-RAIRS of VENUS. *Source: Congiu et al. (2020)*

2.2.5 Temperature Programmed Desorption

Temperature Programmed Desorption is a valuable technique for studying the thermal desorption of species from surfaces. During a typical TPD experiment, a species is first deposited

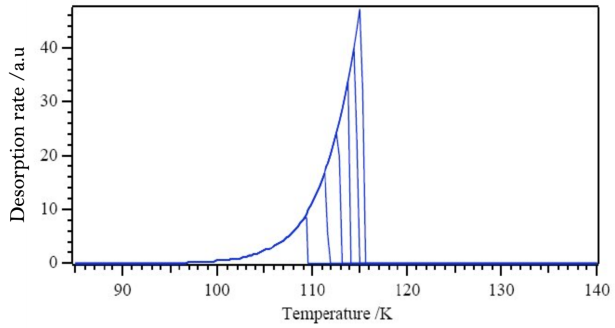

(a) zero order desorption

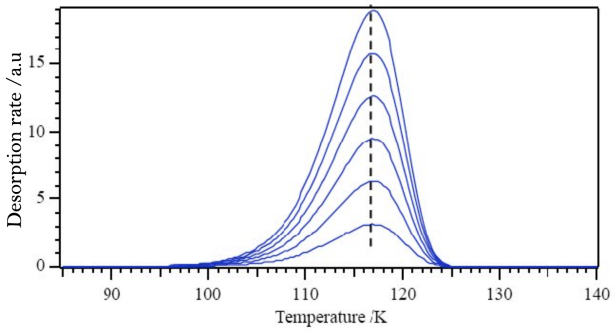

(b) first order desorption

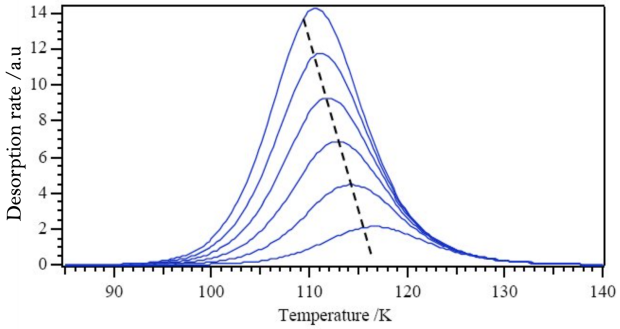

(c) second order desorption

Figure 2.5: Desorption curves for various orders of desorption.

onto the surface. The temperature, T, of the surface is then increased linearly, and the desorbed species are monitored using a QMS. The species on the surface gain sufficient thermal energy from the surface to desorb. The heating process is described by:

$$T = T_0 + \beta t \tag{2.1}$$

where $\beta = \frac{dT}{dt}$, represents the heating rate or the ramp and T_0 the initial temperature of the surface.

The desorption rate of an adsorbed species, X, follows the Arrhenius law and is described

by the Polanyi-Wigner equation:

$$r = \frac{dN}{dt} = \nu N_X^n \; exp\left(\frac{-E_{des}}{k_B T}\right) = k_{td} N_X^n \tag{2.2}$$

Here, ν is the pre-exponential factor that indicates the frequency of vibration of the bond between the species and the substrate, N represents the surface coverage of the species, and n is the order of desorption (ranging from 0 to 2).

Depending on the order of desorption, the kinetics can be categorised into three types. In zero-order desorption ($n = 0$), the desorption rate is independent of the coverage of the species (Fig. 2.5a). The desorption curve is characterised by common leading edges until peak desorption, after which the curve sharply falls to zero. This typically corresponds to the desorption of multiple layers of the adsorbed species. First-order desorption ($n = 1$) is observed in cases involving unimolecular or atomic desorption (Fig. 2.5b). Characteristic features of the desorption curves include common peak position regardless of coverage and asymmetric profiles featuring a longer leading edge and a shorter tail. In second-order desorption (n = 2), there is a shift in the peak desorption temperature with varying coverage (Fig. 2.5c). As the coverage increases, the peak desorption shifts to lower temperatures, indicating that the reaction rate is proportional to the concentration of the adsorbate. The desorption profiles are symmetric and share common trailing edges.

When an adsorbed species gains enough energy, it can move across the surface and scan binding sites. These species tend to occupy the sites with the highest binding energy first, followed by those with lower binding energy. This behaviour is reflected in the TPD curve, where peak desorption occurs at higher temperatures under low coverage. As coverage increases, the desorption curve broadens towards lower temperatures. When all of the sites on the surface are filled, any adsorbing species are adsorbed onto the species already adsorbed on the surface. The peak of the TPD curve begins to shift towards higher temperatures and increases in height and we see the typical shape of a TPD of the zeroth order.

2.3 Results

2.3.1 Calibration for 1 monolayer of NH_3

The initial step involves calibrating the molecular flux of NH_3. Figure 2.6 illustrates the calibration experiments performed to achieve this. In these experiments, varying doses of NH_3 were deposited onto a gold substrate at 10K, followed by TPD analysis.

At low dosages (less than 1 ML), the peak desorption temperature is higher. As the dosage increases, this peak shifts to lower temperatures. Once all adsorption sites are occupied, the peak desorption temperature no longer shifts. At this saturation point, additional NH_3 molecules bind to NH_3 already adsorbed on the surface, resulting in desorption following zeroth order kinetics. This phenomenon is evident from the increase in peak height (as observed in the 12-minute curve and beyond) and the subsequent shift of the curve towards higher temperatures.

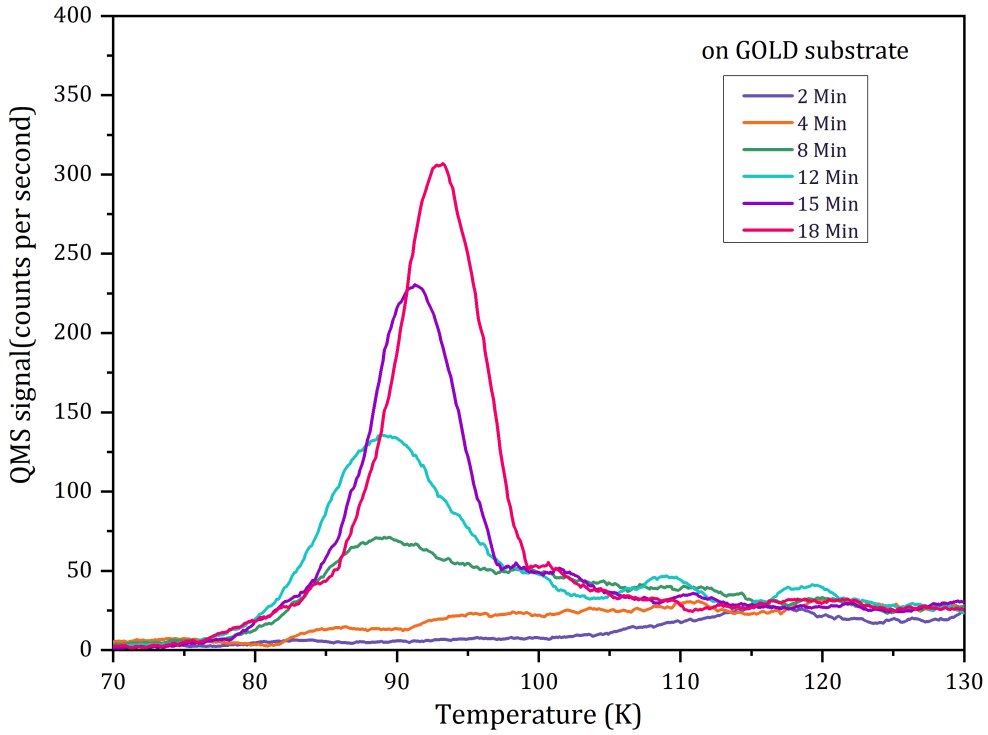

Figure 2.6: Experiments to calibrate for 1ML of NH_3. TPD curves of NH_3 deposited on a gold substrate for various dosages. NH_3 is injected at a constant pressure of 4.67×10^{-5} mbar varying the duration of injection to obtain the desired dosage.

Based on our experiments, 1ML is formed for an exposure time of greater than 8 minutes but lesser than 12 minutes. Based on these findings, we choose an exposure time of 9 minutes for subsequent experiments, which aligns with the times determined for ^{13}CO and N_2 under similar beam conditions.

2.3.2 Co-deposition experiments

The initial set of experiments are aimed at understanding the interaction of ammonia with the major components found on grain mantles. Three major molecules are considered: H_2O, CO, and CO_2. However, for the experiments, ^{13}CO (mass = 29 amu) is used instead of ^{12}CO (mass = 28 amu) to allow for a clear distinction from atmospheric N_2 (mass = 28 amu) by the QMS. Similarly, the major mass channels for water and NH_3 are 18 amu and 17 amu, respectively. Water also has fragments of mass equal to 17 amu, and NH_3 fragments into mass of 16 amu. To distinguish between these overlapping fragments of H_2O and NH_3, experiments are performed using each species separately, the ratio (percentage) of fragmentation into each mass by the QMS is determined, and the quantities for each mass are calibrated proportionately.

Initially, ammonia is co-deposited separately with each component. A second set of co-deposition experiments is then conducted, incorporating water into the mixture. The species are injected onto the gold substrate, which is maintained at a temperature of 10 K during

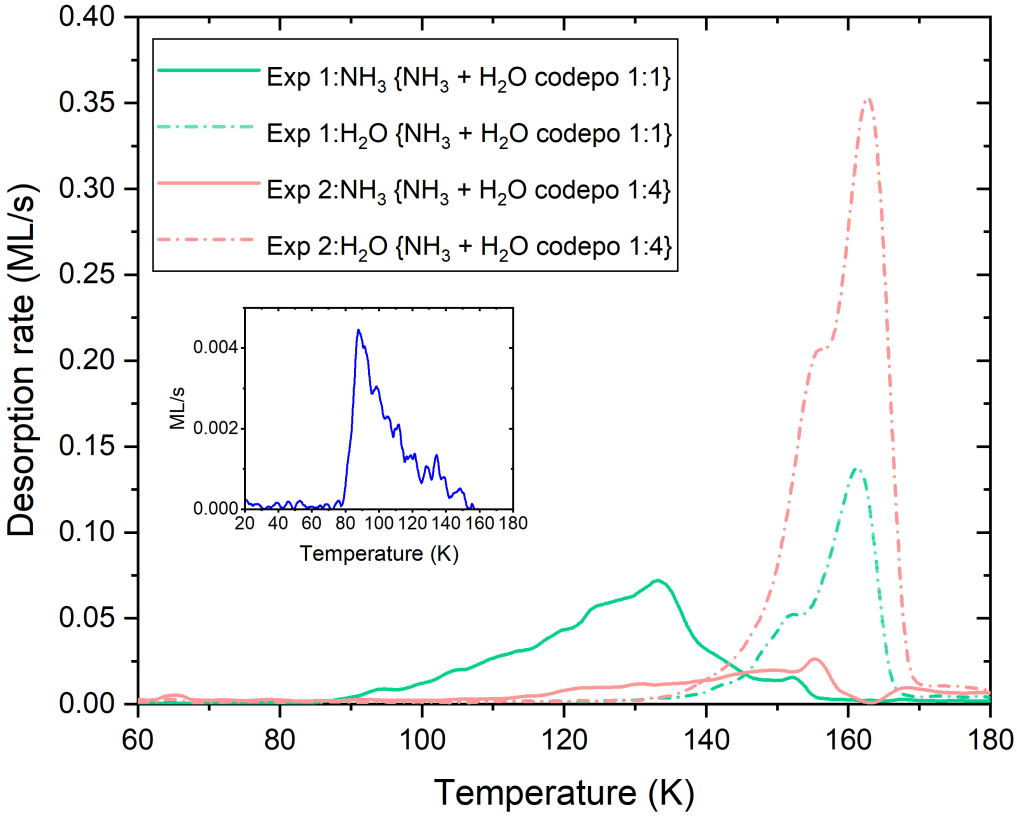

Figure 2.7: NH_3-H_2O co-deposition experiments. All experiments were performed on a gold substrate. The TPDs had a ramp of 0.2 K/s. The solid lines represent the desorption of NH_3, while the dashed-dotted lines represent the desorption of water. Lines of the same colour belong to the same set of experiments. Inset: TPD of 1 ML NH_3 from a gold surface used to calibrate all the subsequent experiments.

the deposition. Each of these species is dosed using separate beams. The pressure of the NH_3, ^{13}CO, and CO_2 at the first stage of the beam is a few 10^{-5} mbar (corresponding to a flux: 0.1 sccm [2]), while that of H_2O is 4.8×10^{-5} mbar. A monolayer is defined as 1×10^{15} molecules cm^{-2}. The reproducibility between two depositions is within a few percent, and the accuracy in the absolute determination of an ML is around 20%, as it is more precise for some molecules and less for other species (such as NH_3).

Table 2.1 lists the experiments used for the co-deposition experiments along with the ratios and monolayers of each species used. Two types of mixing ratios are used for the co-deposition of ammonia with other species (including water). In the first set, all adsorbates (NH_3, ^{13}CO, CO_2, and H_2O) are deposited in equal proportions, while in the second set, the ratios are based on astronomically observed abundances (McClure et al. 2023; Rocha, W. R. M. et al.

[2]sccm = standard cubic centimetre

2025). The raw data (mass spectra) are accessible online via a dedicated database.[3] Other sets of experiments are also carried out and analysed under similar conditions. These experiments are listed in Appendix A and are accessible online. For this work, the experiments that best demonstrate the findings are selected.

Table 2.1: List of co-deposition experiments.

No.	Experiment	Ratio	Quantity deposited (ML)
1	{NH_3 + H_2O}	1:1	~10 each
2	{NH_3 + H_2O}	1:4	5.8 (NH_3), 23.8(H_2O)
3	{NH_3 + ^{13}CO}	1:1	11.3(NH_3), 12.3(^{13}CO)
4	{NH_3 + ^{13}CO}	1:6	1(NH_3), 6.5(^{13}CO)
5	{NH_3 + ^{13}CO + H_2O}	1:1:1	8.1(NH_3), 9.2(^{13}CO), 9.2(H_2O)
6	{NH_3 + ^{13}CO + H_2O}	1:2:9	1.6(NH_3), 3.6(^{13}CO), 8.9(H_2O)
7	{NH_3 + CO_2}	1:1	14.7(NH_3), 14.7(CO_2)
8	{NH_3 + CO_2}	1:7	0.7(NH_3), 5.4(CO_2)
9	{NH_3 + CO_2 + H_2O}	1:1:1	9(NH_3), 9.3(CO_2), 8.9(H_2O)
10	{NH_3 + CO_2 + H_2O}	1:4:5	1.5(NH_3), 4(CO_2), 5.5(H_2O)

Note: All experiments are performed on a gold substrate held at 10 K. The ratios have been rounded off to the nearest whole number for visual convenience, while the number of monolayers deposited is mentioned to one decimal point of accuracy. The ramp during the TPD was 0.2 K/s.

Figure 2.7 shows the TPD curves of the NH_3-H_2O co-deposition experiments. In the calibra-

[3] https://lerma.labo.cyu.fr/DR/traitement.php

tion experiment (Fig. 2.6), a sudden rise in the NH_3 desorption around 80 K is seen, which falls off slowly once peak desorption has been completed. During the co-deposition with water, a significant decrease of the NH_3 desorption rate is observed, and peak desorption is shifted to higher temperatures. About 6% of the deposited NH_3 with regard to H_2O is trapped by water and then released during the phase change of water from an amorphous to crystalline form. This trapped fraction was estimated by calculating the area under the TPD profile of the desired species (in this case NH_3). In reality, water deposited at such a low temperature is fairly porous and, hence, has a larger surface area wherein the NH_3 molecules can lodge themselves. Upon increasing the temperature, water underwent a phase change from amorphous to crystalline form, which can be observed through the plateau or "shoulder" at around 155 K in the desorption curve of water (Fig. 2.7; see also Speedy et al. 1996). During this phase change, water molecules began to re-arrange to form a crystalline structure, during which any NH_3 in its bulk was pushed out. The higher the H_2O/NH_3 ratio, the more the desorption of ammonia was delayed. When the NH_3 concentration was very high, there were more NH_3-NH_3 interactions that could substitute for NH_3-H_2O interactions.

During the co-deposition experiments of NH_3-^{13}CO mixture (Fig. 2.8), NH_3 desorbs independently (top row Fig. 2.8a and 2.8b) of ^{13}CO, irrespective of the ratio between the two. All of the NH_3 is desorbed between 80 K and 132 K. The desorption is in good agreement with a fit to the desorption rate equation $A \times exp(-E/k_b T)$, where E/k_b is the binding energy (in Kelvins), T is the temperature (in Kelvins), and A is the pre-exponential factor (s^{-1}). Since the experiments are in the multilayer regime (zero order kinetics), $E/k_b = 2965$ K and the $A = 2.1 \times 10^{12} s^{-1}$ are chosen following Martín-Doménech et al. (2014) and assuming that 1ML = 10^{15} molecules cm^{-2}. The offset from the fit seen in 2.8b is due to the low quantities of NH_3 used for the experiments. Higher quantities would ensure a good fit, as in the previous case.

When present with NH_3 in equal quantities, 85.8% of the deposited ^{13}CO is desorbed between 20 K and 50 K (Fig 2.8c, middle row, orange curve) and ^{13}CO exhibits a volcano effect due to NH_3. A volcano effect is the sudden desorption of a volatile species trapped under a less volatile species, such as H_2O, when the latter begins to desorb (Smith et al. (1997), Viti et al. (2004), Collings et al. (2003)). This volcano effect can be observed from the peak between 68 K and 80 K, and accounts for approximately 9% of the total desorbed ^{13}CO. This trapping is not observed when NH_3 is present in trace quantities, since there isn't enough NH_3 (Fig 2.8d). The ^{13}CO peak between 90 K and 110 K is the CO desorbing with NH_3. This is probably the CO being adsorbed on the substrate during the initial moments of the co-deposition and thereby buried under the later layers of NH_3 and ^{13}CO. The right panels of Fig. 2.8 contain the experiments in proportions that are more astronomically relevant. Here, NH_3 is deposited in trace amounts (1 ML or sub-monolayer quantities) as compared to ^{13}CO and H_2O. Once again, for NH_3, a similar desorption trend as in the case of the experiments presented in Fig. 2.7 is observed.

In the presence of H_2O, the trend in the desorption of NH_3 and ^{13}CO is different. There is as a significant delay in the desorption of NH_3. When present in quantities roughly equal to water, the NH_3 desorption rate is slower, and the desorption is delayed compared to its desorption in the absence of water. In the multi-layer (Fig. 2.8a) and the sub-monolayer

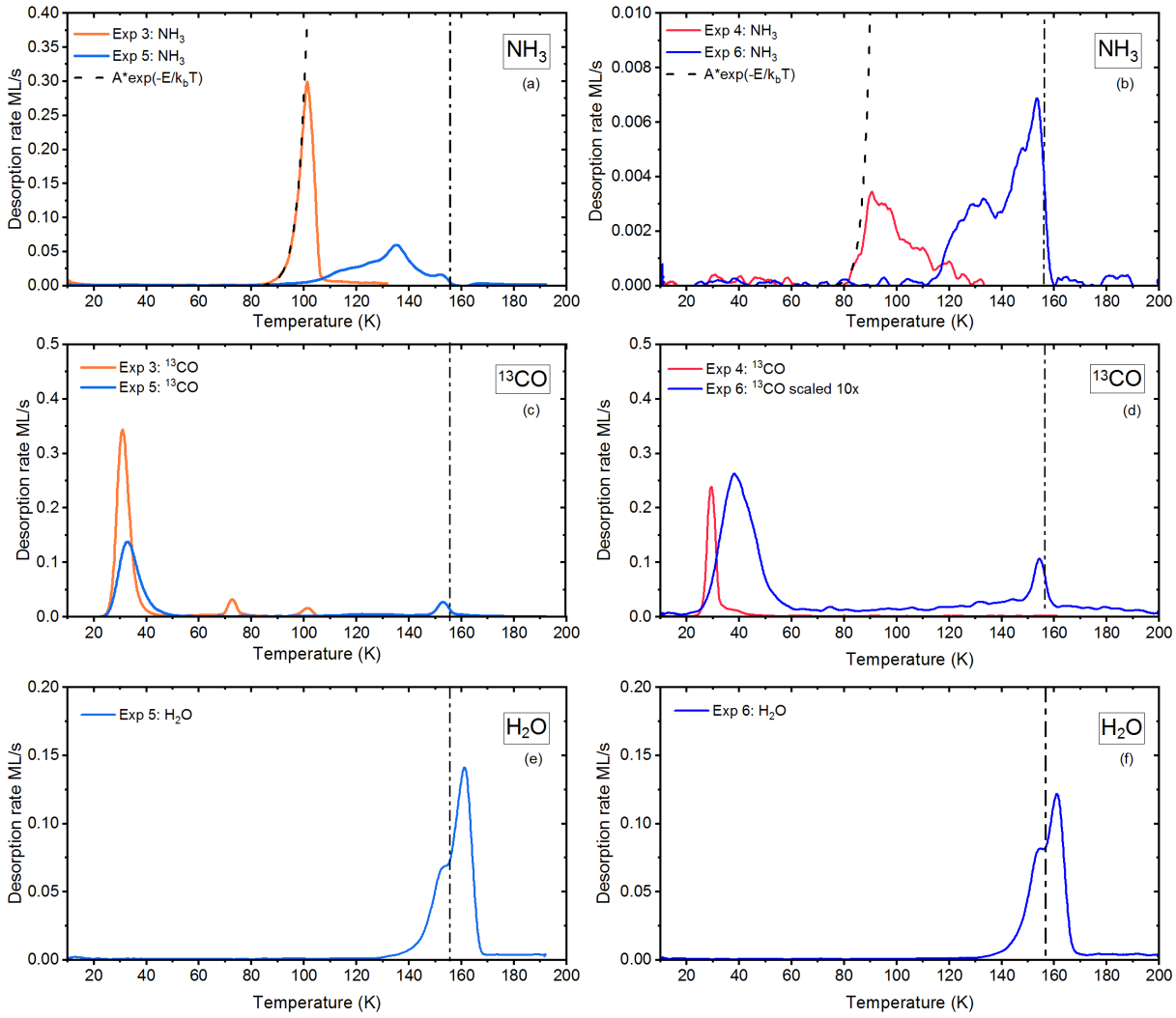

Figure 2.8: NH_3-^{13}CO (and H_2O) co-deposition experiments. The mass channels used for H_2O, NH_3, and ^{13}CO are 18 amu, 17 amu, and 29 amu, respectively, also accounting for fragments of mass = 17 amu (for H_2O) and 16 amu (for NH_3). All experiments are performed on a gold substrate. The TPDs have a ramp of 0.2 K/s. Lines of the same colour belong to the same set of experiments. The dash-dot vertical line at 155 K marks the temperature of the phase change of water from amorphous to crystalline.

(Fig. 2.8b) scenarios, the NH_3 desorption is shifted to higher temperatures. In the former, NH_3 desorption is delayed, possibly because it needs to diffuse through the bulk of the ice before desorption can take place. In the latter, at low concentrations, there is a higher probability for greater NH_3-H_2O interaction and lower NH_3-NH_3 interaction via hydrogen bonds, resulting in water holding on to NH_3 for a little longer than when NH_3 is present in larger quantities. It is worth noting that in both cases, an NH_3 volcano peak due to the crystallisation of water is seen. Roughly 5% of NH_3 with regard to water is trapped by water when co-deposited in equal quantities, and around 8.5% is trapped by water in the more

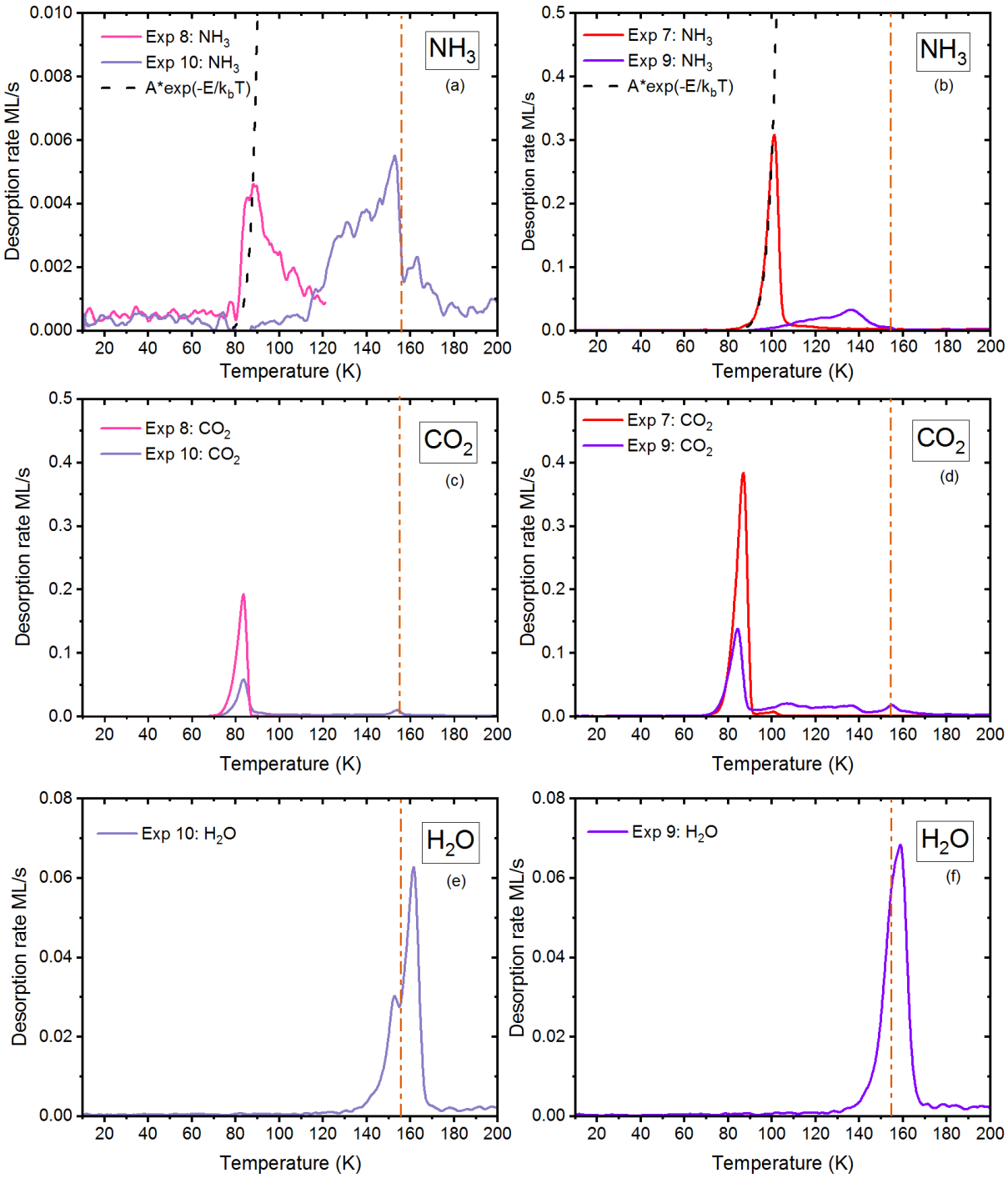

Figure 2.9: Same as Fig 2.8 but using CO_2 instead of ^{13}CO. The mass channel used for CO_2 is 44 amu.

astronomically relevant scenario (Expt 6 in Table. 2.1) where it is released, as observed in previous experiments, during the H_2O change of phase from amorphous to crystalline.

The co-deposition experiments of NH_3 with CO_2 also exhibited a similar behaviour as experiments with CO. The NH_3 desorption appears to be unaffected by the presence of CO_2 (Fig.2.9a and 2.9b), as NH_3 desorbed in the same temperature range as in the experiments with ^{13}CO. Its desorption fits well with the curve of the desorption rate equation with the values taken from Martín-Doménech et al. (2014). When NH_3 and CO_2 are in equal quantities (Fig. 2.9b), the bulk of CO_2 desorbs between 70 K and 92 K. Of the deposited CO_2, 2% desorbs during the desorption of NH_3. This could be due to mechanical trapping by NH_3, and hence the former may be able to desorb only after all the NH_3 has desorbed. The shift in peak desorption temperature of NH_3 towards higher values as observed in Fig. 2.9b when compared to Fig. 2.9a is due to the fact that in the former, there are multiple layers of NH_3. Additionally, in the sub-ML experiments (Fig. 2.9a, c and e), very low quantities of NH_3 are used, and therefore, the interaction between NH_3 and the gold substrate becomes significant. Once again, the presence of H_2O seems to significantly alter the desorption of both NH_3 (Fig. 2.9a and b) and CO_2 (Fig. 2.9c and d). The NH_3 desorbed in a similar manner to the previous experiments with ^{13}CO. Its desorption was not only delayed, but the rate was also slower. Roughly 9% of it was trapped and then later released during the phase change of H_2O. The CO_2 desorption, on the other hand, does not appear delayed. However, roughly 2% of it was trapped by water and then released along with NH_3 during the phase change of H_2O. In previous experimental works, Bossa et al. (2008) and Noble et al. (2014) have shown that carbamic acid (NH_2COOH) can be formed as early as 80 K by thermal reaction of CO_2 and NH_3. This is not detected in the present experiments, which are performed in much thinner layers compared to their work. Similarly, Potapov et al. (2019) reported the formation of $NH_4^+NH_2COO^-$, which is also not detected in our experiments.

2.3.3 Desorption of NH_3 from different types of ices

A second set of experiments are performed to understand the desorption dynamics and determine the distribution of binding energies. The method used is discussed in more detail in De Jong & Niemantsverdriet (1990), He et al. (2011), and Amiaud (2006). Subsequent depositions of roughly 1 ML of NH_3 are made on each type of ice substrate followed by a TPD. Two kinds of ice substrates are used for this purpose: CI and c-ASW. The CI substrate is formed by depositing water onto the gold deposition surface held at 110 K followed by flash heating up to 150 K. To create a c-ASW substrate, water is deposited onto the gold substrate at 110 K at an incident angle of $\theta = 0°$ with respect to the normal angle of the gold substrate. A normal angle of incidence leads to a denser ice substrate, as shown by Kimmel et al. (2001a,b). Several studies have shown a key role between the deposition temperature and its effect on the ice substrate. Scott Smith et al. (2006) found that water deposited at $\leq$ 110 K is amorphous but already begins to pre-crystallise at $\geq$ 120 K since this state is thermodynamically favoured. He et al. (2019) and Bossa et al. (2012) observed a significant reduction in the porosity of the substrate beyond 100 K. These studies were performed on samples that are $\sim$ 200 MLs and $\sim$ 3000 MLs, respectively, while the present study focuses on thin ices ($\sim$ tens of monolayers). Hence, it is safe to assume that the amorphous substrate formed in this case is indeed compact.

To prepare the raw data for analysis, an initial adjacent averaging smoothing process em-

ploying 35 data points is applied using Origin software. This initial smoothing is carried out to reduce background noise, which becomes significant at low dosages and high temperatures. Subsequently, the smoothed data is fed into a custom software developed at LERMA, which fits a set of 19 independent TPD curves distributed evenly over a range of 19 binding energies spanning from 3030 K to 5730 K. A more comprehensive explanation of this method can be found in Chaabouni et al. (2018). In this analysis, a pre-exponential factor, A, with a value of 1.94 x 10^{15} s^{-1} is chosen, as per the findings in Table 2 of Minissale et al. (2022). The results (Fig. 2.10 and 3.5) are presented in the form of blue curves, representing the mass spectrometer data, and orange curves, representing the fit to the experiments conducted using software developed at LERMA.

Figure 2.10 presents three consequent depositions of 1 ML of NH_3 on the same crystalline ice substrate. NH_3 on CI desorbs in a manner similar to NH_3 on the gold substrate just as in the calibration experiments (Fig 2.6). There is a sharp increase in the desorption rate at 75 K, with most of the desorption between 78 K and 140 K. On CI, two desorption peaks are observed. The first one, between 76 K and 98 K, corresponds to the NH_3-NH_3 interactions than of NH_3 with the surface. This peak can appear even without complete layers of NH_3. The second peak, between 98 K and 112 K, is expected to resemble the TPD curves from previous NH_3 depositions, given that the same amount of NH_3 (1 ML) is deposited on the same crystalline ice substrate. However, an increase in peak intensity is observed with each deposition, indicating that the ice surface evolves through repeated NH_3 dosing. This suggests that NH_3 is able to amorphise the ice by introducing defects into the ice surface structure. This modification seems, however, to be a surface phenomenon and alters only the top layers of the surface. Even when the quantity of NH_3 is increased, NH_3 prefers to bind to H_2O than with itself, marked by the increase in peak height (Fig. 2.10). Nevertheless, this modification does not affect the desorption of either H_2O or NH_3, as the latter is eventually pushed out of the surface of CI during the desorption of water. This, in turn, renders it harder to calculate one single value of binding energy for NH_3 on CI.

He et al. (2016) conducted a similar investigation in which they deposited NH_3 onto a CI substrate to determine the binding energy of NH_3 desorption. The present study exhibits considerable resemblance with their research, particularly with respect to their TPD curve obtained for a deposition of 2 ML. Noticeably, a major proportion of the desorption events in both studies take place within the temperature range of 80 K to 145 K. However, there is a discrepancy in the temperature at which the multilayer desorption peak appears. He et al. (2016) reported this peak at a slightly elevated temperature, approximately 100 K. This difference could potentially be attributed to their use of a higher heating ramp rate than this work, estimated to be around 0.5 K/s, during their TPD experiments. Another distinguishing feature between the two studies pertains to the temperature of complete desorption of the ices. In this investigation, the ices are nearly completely desorbed by 140 K, whereas in their work, desorption signals are present beyond 140 K. Unfortunately, a more comprehensive comparison is hindered by a lack of specified units for the desorption rate in the pertinent figure (Fig. 9) within their study. The difference in heating rate is certainly the main difference since the slower the heating, the earlier the desorption for an equivalent quantity. In terms of the determination of binding energies, He et al. (2016) adopting the direct inversion method, reported binding energy values falling within the range of approximately

2900 K to 4100 K. Notably, these binding energy values are lower than the values obtained in this study. This variation in binding energy values may be a result of a lower pre-exponential factor used, specifically 10^{12} s^{-1}, in their methodology as compared to the one employed in this study using the conversion formula proposed in Chaabouni et al. (2018) and reported in the review of Minissale et al. (2022).

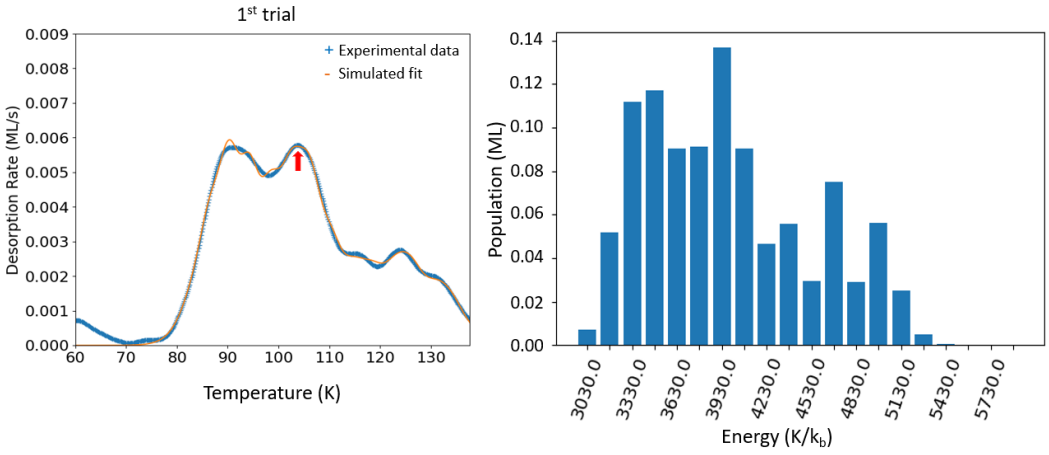

(a)

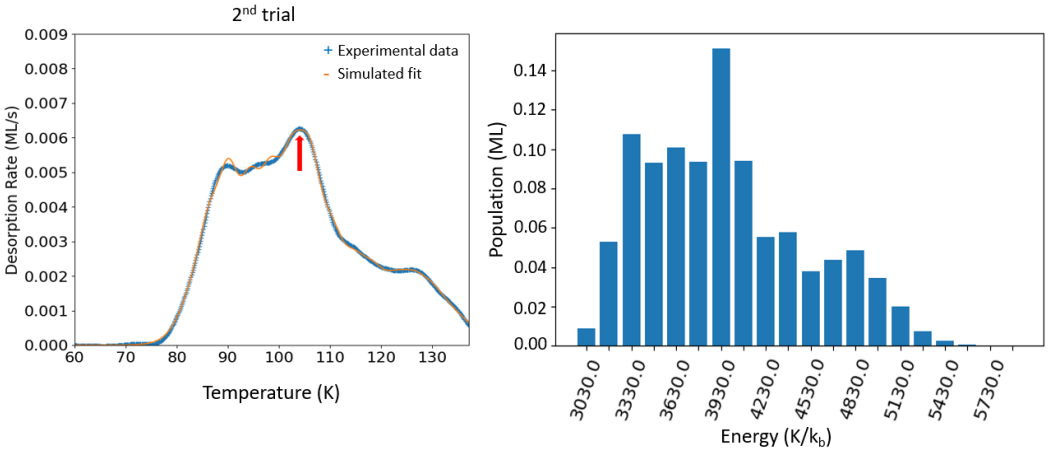

(b)

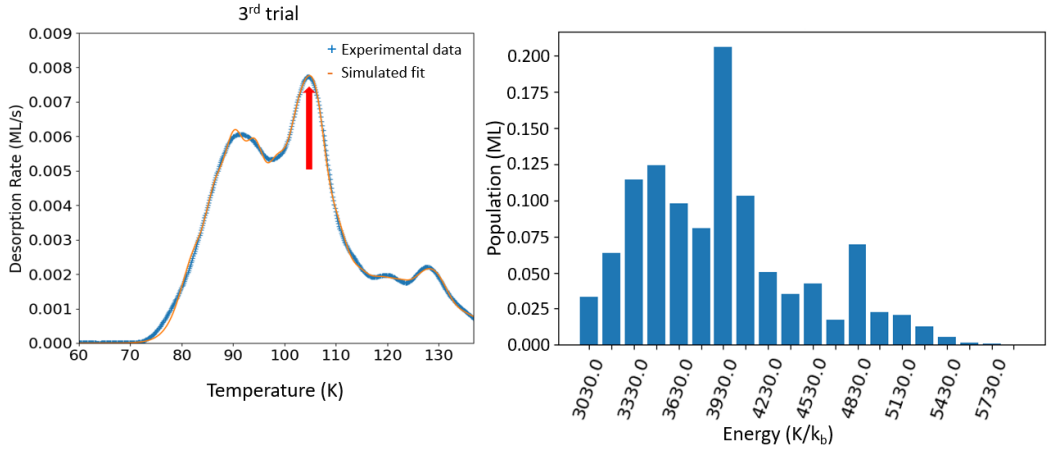

(c)

Figure 2.10: Binding energy fits of the TPDs *(left column)* and the corresponding binding energy distribution histograms *(right column)* of three separate, subsequent depositions of 1 ML of NH_3 on the surface of CI. Each deposition is followed by a TPD to remove the ammonia deposited on the ice substrate before the subsequent deposition was made. The preference of ammonia to bind to water instead of itself can be seen through the progressive increase in peak height (indicated by the red arrow) with each trial.

In contrast, NH_3 desorbs from c-ASW (Fig. 2.11) at higher temperatures. This delay could be due to the structure of c-ASW, i.e., the presence of concavities at the molecular level on its surface where NH_3 can lodge itself and be surrounded by many water molecules and hence form more hydrogen bonds than in the case of CI. The desorption curve has a single broad peak, in contrast to what is observed with CI. A bulk of this desorption takes place between 95 K and 140 K. On CI, the estimated binding energy between two monolayers of ammonia is between 3180 K- 3630 K and between ammonia and the surface of the water substrate between 3780 K – 4080 K. On c-ASW, the binding energy values are between 3630 K and 5280 K. The values are in very good agreement with the values obtained from ASW ice via theoretical calculations by Tinacci et al. (2022) and Germain et al. (2022), for the same value of the pre-exponential factor.

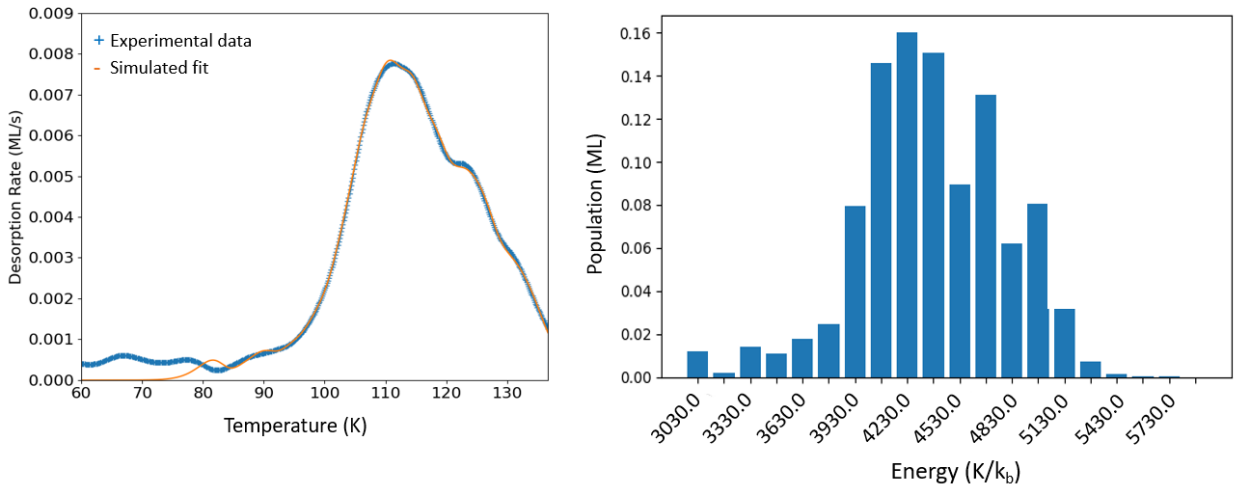

Figure 2.11: Binding energy fit *(left panel)* for 1ML deposition of NH_3 on c-ASW ice and the corresponding binding energy histogram *(right panel)*.

2.3.4 Temperature programmed during-exposure desorption experiments (TP-DED)

The aim of this rather rarely used type of experiment is to mimic snow line regions where both accretion and depletion on grains (i.e. adsorption and desorption) take place simultaneously. A snow line is defined in a region with a thermal gradient that applies on the grains (i.e. hotter towards the star and cooler in the outer regions) such that there exists a frontier zone (the snow line) where the accretion balances out the desorption. Towards the colder side, the accretion dominates and the molecules condense onto the grains, whereas on the hotter side, the concerned species are in the gas phase. The goal here was to investigate the snow line of NH_3 using this type of experiment. Figure 2.12 shows the basic schematics of a TP-DED experiment using the example of pure NH_3 deposition. For this set of experiments, the desired species is deposited onto the gold substrate (Fig. 2.12a.) as the substrate is simultaneously heated or cooled at a constant ramp of 0.5 K min^{-1}. During the heating process, as the deposition progresses, the species continues to accumulate or adsorb on

the substrate (2.12b.) until its desorption temperature range is reached. At this point, the species begins to slowly desorb from the substrate, and any incoming species desorbs immediately (2.12c.) until no more incoming molecules can adsorb due to the temperature of the surface being higher than the desorption temperature (2.12d). The reverse occurs during the cooling process. The experiment was monitored using the FT-RAIRS during the deposition and usually followed by a TPD at the end. The details of each experiment are given in Table 2.2.

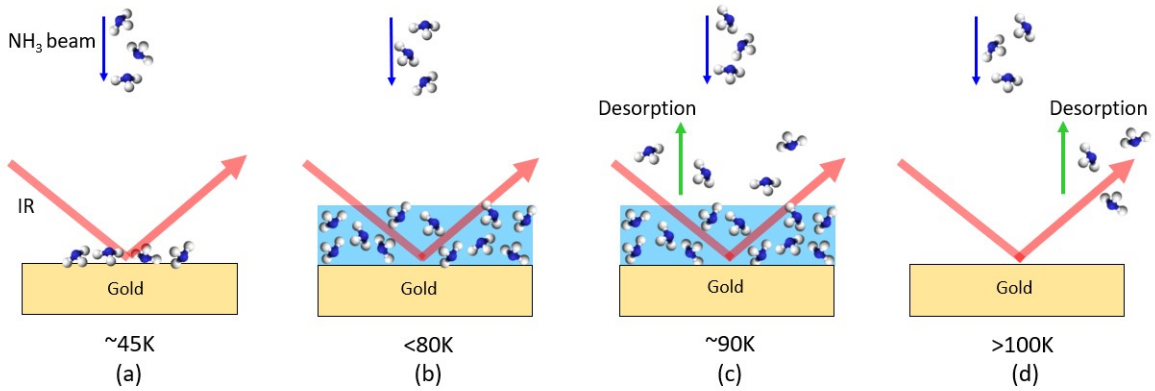

Figure 2.12: Schematic explaining the sequence of events in the TP-DED experiment. Here, an NH_3 beam is used as an example, but the same procedure follows for all three TP-DED experiments performed in this work. The temperatures in each sub-figure in the schematic are merely indicative due to the flux dependence of the adsorbate and do not represent the unique temperature at which the events take place.

Table 2.2: Summary of TP-DED experiments listing the adsorbates and the temperature range for the heating/cooling.

Expt No.	Adsorbate	Temperature Range (K)
1	NH_3	40 - 105 105 - 94
2	$NH_3 + H_2O$	40 - 180 180 - 60
3	$NH_3 + H_2O + CO_2$	40 - 180

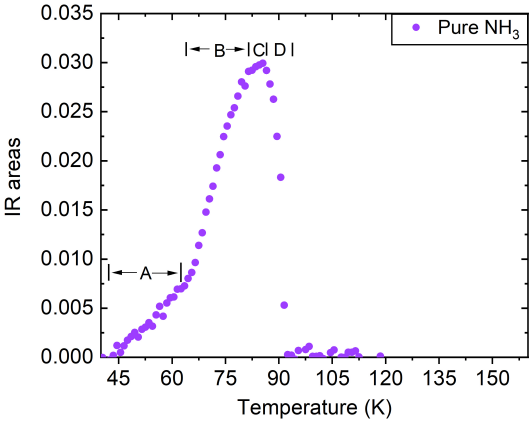

(a)

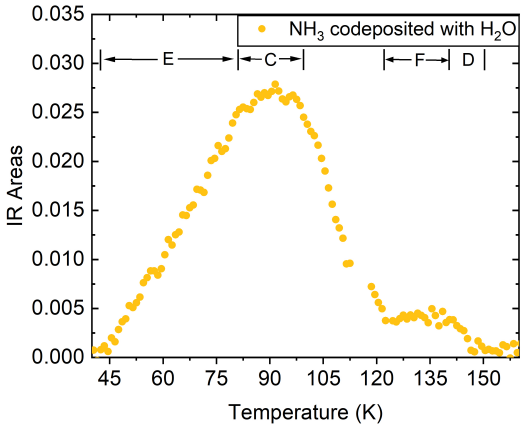

(b)

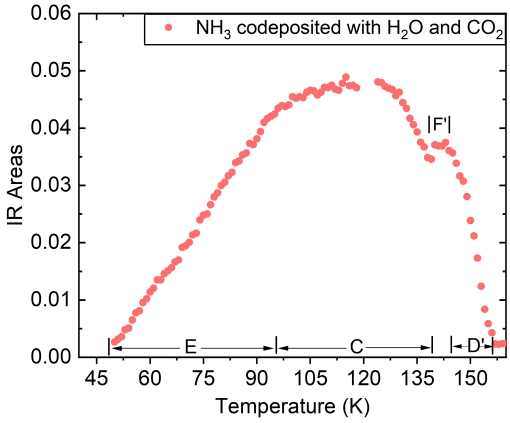

(c)

Figure 2.13: Figure depicting the quantity of NH_3 deposited with respect to temperature (K) during the TP-DED experiments, measured using a FT-RAIRS. For details on the zones A, B, C, D, D', E, F, and F', see main text, Section 3.3,

For the analysis, the area under the IR peak at 3383 cm^{-1} of NH_3 is plotted against temperature. The areas are calculated using the vibrational spectroscopy software OPUS[4] by the company BRUKER. A baseline correction is applied where necessary. In experiments two and three (Table 2.2), due to heavy baseline distortion and the fact that the IR peaks of NH_3 were superimposed with that of H_2O, gross assumptions are made to obtain the IR area of NH_3. Hence, the area reported is the area of NH_3 subtracted from the combined areas of NH_3 and H_2O.

All three experiments (see Fig. 2.13a, 2.13b, and 2.13c) show distinct zones during the TPDED. In the first experiment (Fig. 2.13a), Zone A corresponds to the accretion of NH_3 in the amorphous form. Given the time to form 1 ML on the gold substrate, the signal before 60 K corresponds to NH_3 on the substrate. Beyond this temperature, the observed signal is of NH_3 on an NH_3 layer. Since the surface was continuously exposed to gaseous NH_3 and the desorption was negligible for these temperatures, ammonia accumulated on the surface, marked by a linear increase in the IR absorbance signal. The same trend would be observed for a constant surface temperature desorption. As the temperature rose, the structure of NH_3 changed from amorphous to crystalline, denoted as Zone B and identifiable by a change in the slope. This is due to an increase in the absorption band strength after the phase transition and not due to a change in the flux of accretion, which is stable during every experiment. Cazaux et al. (2021) reported a similar phenomena during the heating of H_2S.

The plateau around 81.5 K (Fig. 2.13a Zone C) marks the zone where desorption is in competition with accretion. As a result, the net accumulation slowed down to almost null at around 88 K. Above 90 K (Zone D), NH_3 desorption drops suddenly since there is no more measurable NH_3 on the surface which desorbs immediately after accretion. Here, desorption dominates over accretion.

The next experiments are the co-deposition of NH_3 with H_2O (see Fig. 2.13b) under similar conditions. The first striking feature is the absence of the region of phase change of NH_3 from amorphous to crystalline. This could be due to the preference of NH_3 to form hydrogen bonds with H_2O than with itself as mentioned earlier. Zone E could, hence, be considered as the region that contains NH_3 within the H_2O structure. The turn-off point between Zone E and Zone C is less pronounced than in the previous case, and it marks the desorption of NH_3 in interaction with itself and probably not the water ice. After roughly 105 K, there is a decrease in the quantity of NH_3 due to the substrate reaching a higher desorption temperature and NH_3 no longer adsorbing as efficiently. An interesting point to note here is that a significant quantity of NH_3 is present on the surface compared to the previous experiment. This can be verified by the plateau (Zone F), which is an indicator of NH_3 in H_2O. This is due to the trapping phenomena by H_2O, which is further strengthened by the NH_3-H_2O interaction. The slow decline in the slope in Zone D corresponds to the release of NH_3 due to the desorption of H_2O as the latter approached its crystallisation temperature.

In the next set of experiments (Fig. 2.13c), we added CO_2 to the NH_3-H_2O mixture. During the experiment, there is a similar trend to that of the previous experiment with H_2O at the

[4] https://www.bruker.com/en/products-and-solutions/infrared-and-raman/opus-spectroscopy-software.html

beginning of the desorption process, i.e., the sudden change in the curve for NH_3 is very subtle, if at all present (Zone E). The accretion continues until the mixture reaches around 97 K. At this temperature, some similarities arise with the previous two experiments. Firstly, the signal of solid NH_3 is characterised by a plateau (Zone C) due to the competition between NH_3 accretion and desorption. This plateau was followed by a sudden yet short drop in the quantity of NH_3, because of the temperature. Zone F marks the narrow plateau due to the NH_3-H_2O-CO_2 interaction. The quantity of NH_3 in this zone is significantly higher than in the two previous cases. This could point to an additional interaction of NH_3 with CO_2 that retains NH_3 until a higher temperature. The most interesting point between all three experiments is the progressive shift in the peak desorption temperature of NH_3 upon the addition of each new species to pure NH_3. Some NH_3 still remains in the solid phase at unexpectedly high temperatures. In the case of the NH_3-CO_2-H_2O mixture, the snow line (the turning point of NH_3) coincides with the beginning of the desorption of water, almost superimposing over their snow lines. This also raises a question about the potential role of CO_2 in the desorption of NH_3. These experiments directly demonstrate that NH_3 lacks a snow line of its own, especially when combined with H_2O (and potentially CO_2), which consequently retains the NH_3 molecules on the grain up to higher temperatures than previously expected and, potentially, in a different spatial zone (the same as water).

2.4 Conclusions

In this present work, the interactions of NH_3 on grain surfaces are studied - which are still poorly understood - in the presence of other species found on grain surfaces, including H_2O, CO_2, and ^{13}CO. Various types of experiments are performed with the four species under conditions that mimicked those found in pre-stellar cores and protoplanetary discs, paying close attention to the behaviour of NH_3 in each case. The binding energy of NH_3 is calculated on two different types of water substrates: compact amorphous solid water ice and crystalline ice. The main findings of are as follows:

1. During the co-deposition of NH_3 with H_2O, there is a delay in the NH_3 desorption temperature and a decrease in the NH_3 desorption rate. H_2O traps around 6% of NH_3, releasing it during the phase change of water from amorphous to crystalline. When NH_3 is co-deposited with either ^{13}CO or CO_2 only, no such trend is seen. This behaviour was observed once again when H_2O is added to the NH_3-^{13}CO or NH_3-CO_2 mixture. In the NH_3-^{13}CO-H_2O and the NH_3-CO_2-H_2O experiments, roughly 5-9% NH_3 with respect to water is trapped, which is released during the phase change of water from amorphous to crystalline.

2. NH_3 has a range of binding energy values instead of a single unique value, in agreement with recent theoretical calculations. For CI, the binding energy values are between 3780 K-4080 K. NH_3 is able to amorphise the substrate surface by disrupting the structural order of the surface of the ice via hydrogen bonding with H_2O. In the case of c-ASW, the binding energies lie in the range of 3630 K-5280 K (for a pre-exponential factor set to A= 1.94×10^{15} s^{-1} in both cases).

3. During the TP-DED experiments, the crystallisation of NH_3 is noticeably impacted in

the presence of H_2O and CO_2. The desorption temperature of NH_3 increases significantly in their presence, and NH_3 desorbs over a longer range of temperature. Some trapping of NH_3 is also noted during the experiments. This indicates that NH_3 has no definite snow line and seems to be strongly influenced by these species. The trapping enables NH_3 to be stored on the dust grains and to be available at later times and/or be transported to regions of higher temperatures (e.g. closer to the central protostar or towards the inner disc of more evolved young stellar objects).

This investigation sheds light on the intricate interactions of NH_3 on grain surfaces, especially in the presence of key species such as H_2O, CO_2, and ^{13}CO. The observed delays in desorption, multiple binding energies, and the influence of these species on NH_3 crystallisation underline the sensitivity of NH_3 to the surrounding molecular environment emphasising the importance of considering these factors for a more accurate understanding of ammonia-and by extension, nitrogen-chemistry in the chemical evolution of dense interstellar regions.

Bibliography

Accolla, M. 2010, PhD thesis, Université de Cergy Pontoise

Amiaud, L. 2006, PhD thesis, thèse de doctorat dirigée par Lemaire, Jean-Louis Astrophysique Cergy-Pontoise 2006

Bossa, B., Theulé, P., Duvernay, F., Borget, F., & Chiavassa, T. 2008, Astronomy and Astrophysics, 492, 719

Bossa, J.-B., Isokoski, K., De Valois, M., & Linnartz, H. 2012, Astronomy & Astrophysics, 545, A82

Caselli, P., Bizzocchi, L., Keto, E., et al. 2017, Astronomy & Astrophysics, 603, L1

Caselli, P., Pineda, J. E., Sipilä, O., et al. 2022, The Astrophysical Journal, 929, 13

Cazaux, S., Carrascosa, H., Caro, G., et al. 2021, arXiv preprint arXiv:2110.04230

Chaabouni, H., Diana, S., Nguyen, T., & Dulieu, F. 2018, Astronomy & Astrophysics, 612, A47

Collings, M. P., Anderson, M. A., Chen, R., et al. 2004, Monthly Notices of the Royal Astronomical Society, 354, 1133

Collings, M. P., Dever, J. W., Fraser, H. J., McCoustra, M. R., & Williams, D. A. 2003, The Astrophysical Journal, 583, 1058

Congiu, E., Sow, A., Nguyen, T., Baouche, S., & Dulieu, F. 2020, Review of Scientific Instruments, 91, 124504

De Jong, A. & Niemantsverdriet, J. 1990, Surface Science, 233, 355

Germain, A., Tinacci, L., Pantaleone, S., Ceccarelli, C., & Ugliengo, P. 2022, ACS Earth and Space Chemistry

He, J., Acharyya, K., & Vidali, G. 2016, The Astrophysical Journal, 825, 89

He, J., Clements, A. R., Emtiaz, S., et al. 2019, The Astrophysical Journal, 878, 94

He, J., Frank, P., & Vidali, G. 2011, Physical Chemistry Chemical Physics, 13, 15803

Kakkenpara Suresh, S., Dulieu, F., Vitorino, J., & Caselli, P. 2024, Astronomy & Astrophysics, 682, A163

Kimmel, G. A., Dohnálek, Z., Stevenson, K. P., Smith, R. S., & Kay, B. D. 2001a, The Journal of Chemical Physics, 114, 5295

Kimmel, G. A., Stevenson, K. P., Dohnalek, Z., Smith, R. S., & Kay, B. D. 2001b, The Journal of Chemical Physics, 114, 5284

Kruczkiewicz, F., Vitorino, J., Congiu, E., Theulé, P., & Dulieu, F. 2021, Astronomy & Astrophysics, 652, A29

Martín-Doménech, R., Caro, G. M., Bueno, J., & Goesmann, F. 2014, Astronomy & Astrophysics, 564, A8

McClure, M. K., Rocha, W., Pontoppidan, K., et al. 2023, Nature astronomy, 7, 431

Minissale, M., Aikawa, Y., Bergin, E., et al. 2022, ACS Earth and Space Chemistry, 6, 597

Noble, J., Theule, P., Duvernay, F., et al. 2014, Physical Chemistry Chemical Physics, 16, 23604

Öberg, K. I., Boogert, A. C. A., Pontoppidan, K. M., et al. 2011, , 740, 109

Penteado, E., Walsh, C., & Cuppen, H. 2017, The Astrophysical Journal, 844, 71

Pineda, J. E., Harju, J., Caselli, P., et al. 2022, The Astronomical Journal, 163, 294

Poch, O., Istiqomah, I., Quirico, E., et al. 2020, Science, 367, eaaw7462

Potapov, A., Theulé, P., Jäger, C., & Henning, T. 2019, The Astrophysical Journal Letters, 878, L20

Redaelli, E., Bizzocchi, L., Caselli, P., et al. 2019, Astronomy & Astrophysics, 629, A15

Rocha, W. R. M., McClure, M. K., Sturm, J. A., et al. 2025, AA, 693, A288

Scott Smith, R., Zubkov, T., & Kay, B. D. 2006, The Journal of chemical physics, 124, 114710

Sipilä, O., Caselli, P., Redaelli, E., Juvela, M., & Bizzocchi, L. 2019, Monthly Notices of the Royal Astronomical Society, 487, 1269

Smith, R. S., Huang, C., Wong, E., & Kay, B. D. 1997, Physical review letters, 79, 909

Speedy, R. J., Debenedetti, P. G., Smith, R. S., Huang, C., & Kay, B. D. 1996, The Journal of chemical physics, 105, 240

Suhasaria, T., Thrower, J., & Zacharias, H. 2015, Monthly Notices of the Royal Astronomical Society, 454, 3317

Tinacci, L., Germain, A., Pantaleone, S., et al. 2022, ACS Earth and Space Chemistry, 6, 1514

Viti, S., Collings, M. P., Dever, J. W., McCoustra, M. R., & Williams, D. A. 2004, Monthly Notices of the Royal Astronomical Society, 354, 1141

Woodruff, D. P. 2016, Modern techniques of surface science (Cambridge university press)

3

Role of NH_3 binding energy in the early evolution of pre- and protostellar cores

The contents of this chapter are based Kakkenpara Suresh et al. (2024b) (to be resubmitted, *Astronomy & Astrophysics*)

3.1 Introduction

In Chapter 2, a distribution of binding energies for NH_3 on different water ice substrates is obtained. In their numerical study, Grassi et al. (2020) illustrated that employing a binding energy distribution allows molecules to occupy higher energy binding sites, thereby increasing their residence time on the grain surface. This prolonged residence time enhances their availability to react with other molecules, even at dust temperatures that conventionally exhibit limited or no reactivity. This, in turn, impacts the chemical complexity in star forming regions. For instance, in protoplanetary disks, employing a distribution of binding energies could affect the location and size of snowlines, which are crucial in determining the composition of planets formed within the disk. The chemical composition of these disks is largely shaped by the composition from earlier stages, specifically the pre- and protostellar stages.

In the present chapter, the impact of incorporating a range of binding energy values, using NH_3 as an example, on abundance distributions in pre- and protostellar cores is evaluated using an astrochemical model and gas-grain chemical networks. In particular, the effect on the abundance distribution of NH_3 due to variations in binding energy is studied. The possible effect that NH_3 abundance variations may have on the distributions of other molecules chemically linked to NH_3 is also examined.

3.1.1 Astrochemical Models

Astrochemical models are crucial for astronomers studying astrophysical sources, as they provide insights into the chemical composition and evolution of these objects. These models typically solve systems of ordinary differential equations (ODEs) to compute the time-dependent abundances of various species. The ODEs used are as follows:

$$\frac{dn_i(gas)}{dt} = \sum_{l,m} k_{lm} n_l n_m - n_i \sum_{ij} k_{ij} n_j + \sum_j k_{diss,j} n_j - n_i \sum_n k_{diss,n} - r_i^{acc} n_i + r_i^{des} n_i \quad (3.1)$$

$$\frac{dn_i(grain)}{dt} = \sum_{l,m} k_{lm} n_l n_m - n_i \sum_j k_{ij} n_j + \sum_j k_{diss,j} n_j - n_i \sum_n k_{diss,n} + r_i^{acc} n_i - r_i^{des} n_i. \quad (3.2)$$

Here n_i, n_l, n_m, and n_j are the abundances of species i, l, m, and j in cm^{-3}, k_{lm} and k_{ij} correspond to the rate coefficients for bimolecular reactions, and $k_{diss,j}$ and $k_{diss,n}$ dissociation rate coefficients of unimolecular reactions, that form and destroy species i. The terms r_i^{acc} and r_i^{des} refer to the rates of accretion and desorption of the species i. The first two terms in the gas-phase and grain equations describe the total bimolecular reactions that either form or destroy species i. The third and fourth terms represent unimolecular reactions leading to the formation and destruction of species i, while the final terms in both equations capture the effects of adsorption and desorption on grain surfaces.

The list of chemical reactions responsible for the formation and destruction of species is known as a chemical network. These networks are divided into two subcategories: gas-phase and grain-surface networks, based on the chemical processes described in section 1.2. Along with the chemical network, the initial elemental abundances, physical conditions (such as density, temperature, and cosmic ray ionisation rate, etc.,), and the geometry of the astrophysical object are essential inputs for these models. When combined with radiative transfer modelling, they help determine the observability of species. The calculation of abundances for key species that cannot be directly observed, such as those without a dipole moment (e.g., N_2), which play a vital role in star formation can also be done with astrochemical models. Furthermore, these models help predict abundance distributions over extended time scales beyond direct human observation.

This chapter is organised in the following way. Sections 2 and 3 discuss the models used as templates for a pre- and protostellar core, respectively, along with the results of the simulations with regard to NH_3, and the implications of these results in the chemistry of other species. A concise summary of our work is provided in Section 4.

3.2 The prestellar core

Pre-stellar cores represent the earliest stages of star formation. We use the model of L1544 as it is a well-studied low-mass pre-stellar core. It is located in the Taurus Molecular cloud at a distance of $\simeq$170 pc (Galli et al. 2019). It is centrally concentrated with central H_2 number densities of $\simeq 10^6$ cm^{-3} (Caselli et al. 2019) and temperatures of $\simeq$ 6 K (Crapsi

et al. 2007). It shows clear signs of infall, suggesting gravitational collapse (Lee et al. 1999), is chemically rich (Spezzano et al. 2017; Jiménez-Serra et al. 2016; Vastel et al. 2018), and has high freeze-out and deuteration fractions (Crapsi et al. 2005; Redaelli et al. 2019).

3.2.1 Physical Model

We use the 1D model by Keto & Caselli (2010) in which the core is assumed to be an unstable Bonnor-Ebert sphere with the density in the inner regions nearly constant and that in the outer regions varying as r^{-2} (where 'r' is the radius). A spherical grain of size 0.1 μm and a 3-phase chemical model following Hasegawa & Herbst (1993b) where the grain is differentiated as (a) a core, (b) an inert ice mantle and (c) a chemically active layer (Fig. 3.2b) which is available for desorption is considered. The efficiency due to reactive desorption is considered a constant value of 1% based on the work by Garrod et al. (2007).

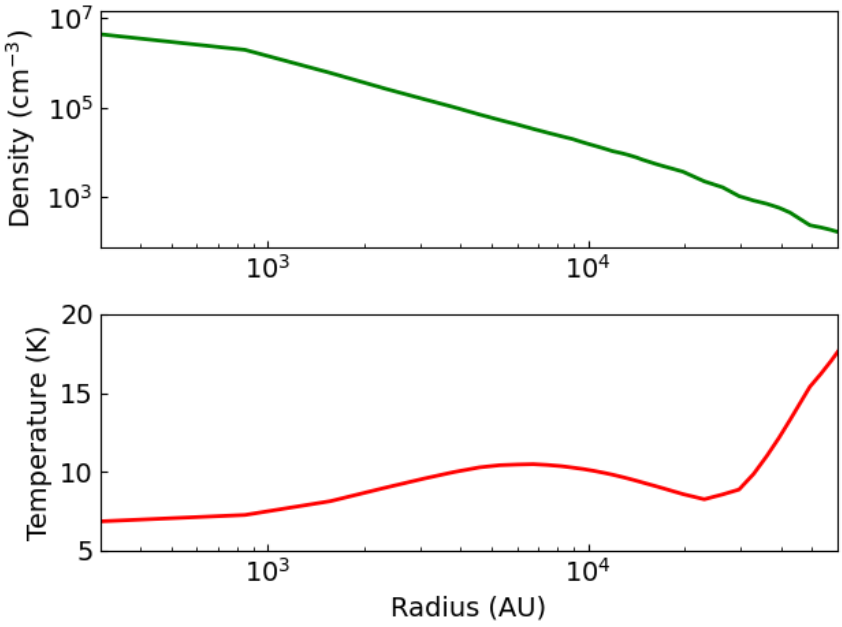

Figure 3.1: (Top) The H_2 number density and **(bottom)** the temperature distribution assumed to model the prestellar core.

3.2.2 Chemical Model

The chemical evolution of the core is tracked by a gas-grain chemical code, *pyRate*, discussed in Sipilä (2012) and Sipilä et al. (2010), that employs the rate equation method to calculate the molecular abundances. The gas-phase network is based on the kida.uva.2014[1] network (Wakelam et al. 2015) modified to incorporate deuterated species and spin state chemistry (Sipilä et al. 2015a,b). The grain surface network is based on Semenov et al. (2010). The species are assumed to be atomic initially, except for H_2 and HD, and the initial ortho/para

[1]https://kida.astrochem-tools.org/networks.html

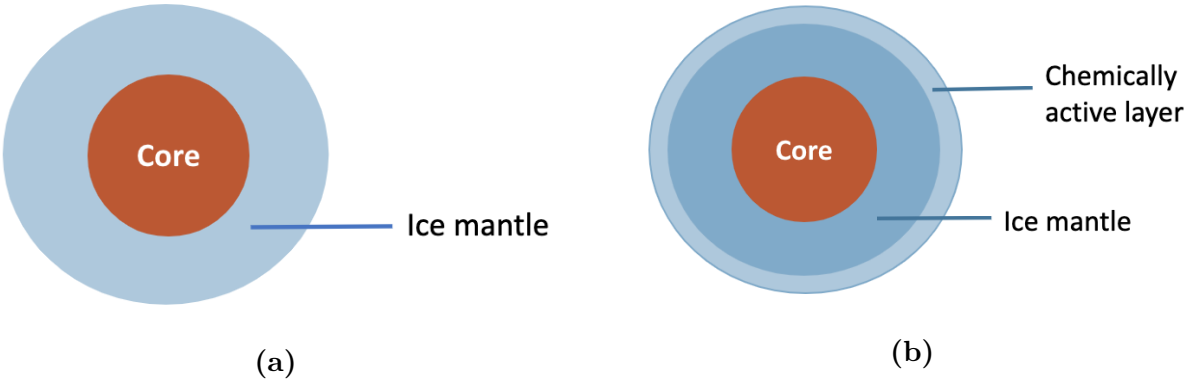

(a) (b)

Figure 3.2: Schematic depiction of (a) two-phase and (b) three-phase grain model.

H_2 ratio is set to 10^{-3} consistent with a spin temperature, $T_{spin} \sim 20$ K (Brünken et al. 2014; Crabtree et al. 2011). This corresponds to the assumption that the spin-state ratio has had the time to undergo thermalisation prior to the formation of the core. The initial abundances of the species are provided in Table 3.1. To calculate the abundances in the pre-stellar core, the core is divided into concentric shells and chemical evolution is computed in each shell separately. These are, then, combined to derive the final radial abundance distribution for a given time step and species. The binding energies for ammonia on water ice surfaces are from Chapter 2. Three binding energy values - 3780 K, 4080 K, and 5280 K - are chosen to cover a broad spectrum of possible strengths of adsorption on water ice, ranging from low to high. The binding energies of various other species are taken from Garrod & Herbst (2006) and Sipilä (2012). The simulated abundances of NH_3 are combined abundances of the ortho and para forms of the molecule.

3.2.3 Abundance Distribution

In Chapter 2, a range of binding energies for ammonia are estimated on water ice substrates. Here, the goal is to study the impact of the binding energy on the chemistry of L1544. Ammonia is assumed to desorb from the top ice layer of the grain, where it could be bound to water and other molecules present on the dust grains. We use three different binding energy values (expressed as E_b/k_B): 3780 K, 4080 K and 5280 K, and allow the simulation to evolve until t = 10^7 years. The abundances are, then, extracted for two time steps: 10^5 years and 10^6 years.

For each binding energy value, two separate models are simulated using different cosmic ray-induced desorption (CRID) rates. Given the high densities and low temperatures in the interiors of these cores, non-thermal desorption mechanisms are required to describe the chemical evolution in these regions. Desorption due to cosmic rays is a frequently adopted non-thermal desorption mechanism because cosmic rays can penetrate the dense interiors of the cores that otherwise remain shielded from UV or optical radiation. These occasionally strike dust grains which are then momentarily heated to a higher temperature. The maximum temperature (T_{max}), set to 70 K in the current model, attained by the dust grain depends on the grain material, grain size, and the energy of the incoming cosmic ray (CR).

Table 3.1: Initial chemical abundances with respect to total H nuclei, n_H, used in the chemical model of the pre- and protostellar core.

Species	Abundance
H_2	5.00×10^{-1}
He	9.00×10^{-2}
HD	1.60×10^{-5}
C^+	1.20×10^{-4}
N	7.60×10^{-5}
O	2.56×10^{-4}
S^+	8.00×10^{-8}
Si^+	8.00×10^{-9}
Na^+	2.00×10^{-9}
Mg^+	7.00×10^{-9}
Fe^+	3.00×10^{-9}
P^+	2.00×10^{-10}
Cl^+	1.00×10^{-9}

This heating causes the desorption of many molecules from the ice mantle surrounding the grain surface. These molecules carry the heat away while desorbing, and, consequently, cool the grain back to its equilibrium temperature, T_{eq} (Fig. 3.3).

In the first model, a constant CRID rate is employed, following the approach proposed by Hasegawa & Herbst (1993a). In their work, the rate constant of CRID is proportional to the ratio of the grain cooling time due to the desorption of volatiles to the transient grain heating interval due to successive CR strikes. The heating and cooling times of the grain are fixed at 3.16×10^{13} s (based on the CR flux from Leger et al. 1985) and 10^{-5} s. In the second model (based on Sipilä et al. 2021), a varying CRID rate is used. Here, the heating interval is determined by the variation in the CR flux with visual extinction (from Padovani et al. 2018) in the core. The cooling is dynamic and depends on time-dependent ice abundances. The efficiency of the cooling is heavily influenced by the total number of available atoms and molecules for cooling, their fractional abundances in the ice, and their binding energies. In total, 12 models are simulated for L1544 for each binding energy, time step, and CRID mechanisms combined.

Fig. 3.4a shows the gas-phase abundance profile of NH_3 at $t = 10^5$ years for the three binding energy values and the model with the fixed CRID rate. The cosmic ray ionisation rate is maintained at 1.3×10^{-17} s^{-1}. Close to the centre of the core (10^2 - 10^3 AU), the efficiency of freeze-out onto the dust grains is high due to low temperatures. As a consequence, the abundances of NH_3 in the gas phase are low. Moving further away, the freeze-out becomes less efficient and hence, NH_3 abundance slowly increases (second zone: 1-3 $\times$ 10^3 AU) until the highest abundance at 7×10^3 AU. Beyond 10^4 AU, closer to the edges of the cloud, the UV radiation prevents the formation of ammonia by breaking up molecules. Consequently,

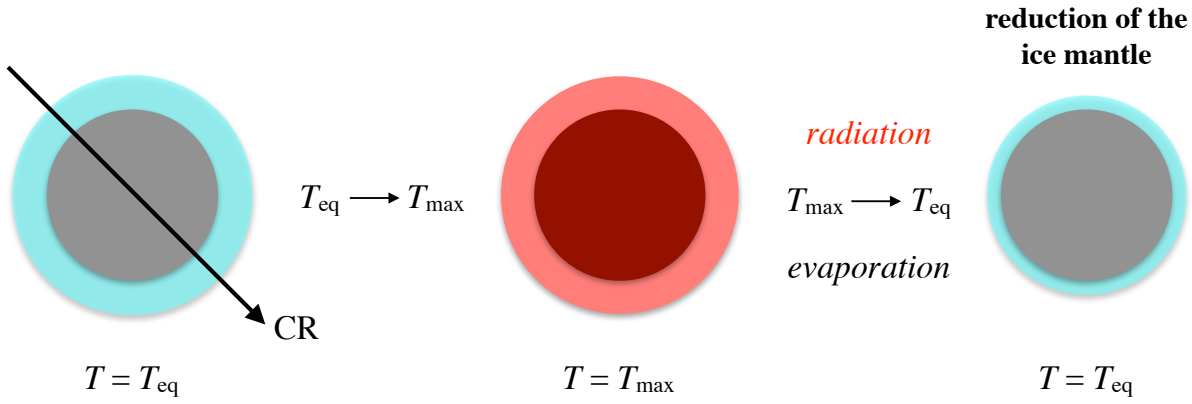

Figure 3.3: Schematic describing the process of Cosmic Ray induced desorption of the ice mantle. *Left*: A cosmic ray strikes a grain which is at an equilibrium temperature, T_{eq}, *Centre*: The grain is transiently heated to a maximum temperature, T_{max}, which induces desorption of species from the grain mantle cooling the grain *Right*: The thickness of the ice mantle is reduced and the grain cools down to its equilibrium temperature. Image credits: O. Sipilä

the ammonia abundance drops. In Fig. 3.4b, NH_3 abundances are plotted for t = 10^6 years when the core is more evolved for the same conditions. Overall, the trend is the same as before except that the abundance at 10^2 AU is higher and the maximum value (between 10^2 - 3×10^3 AU) is lower than at t = 10^5 years.

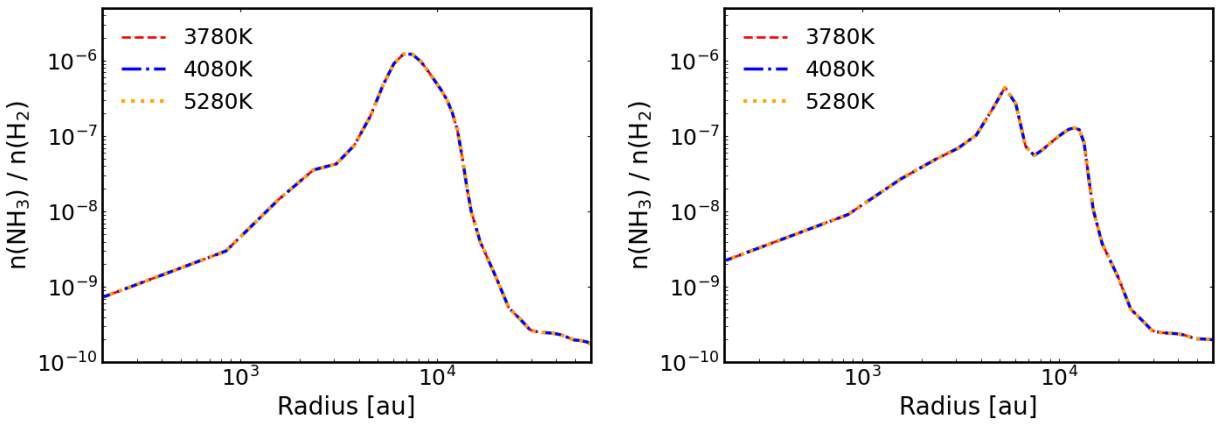

Figure 3.4: Abundance profiles of ammonia as a function of radial distance from the centre in L1544 for three binding energy values (E_b/k_b) at a time, t (a) 10^5 years and (b) 10^6 years for a constant CRID.

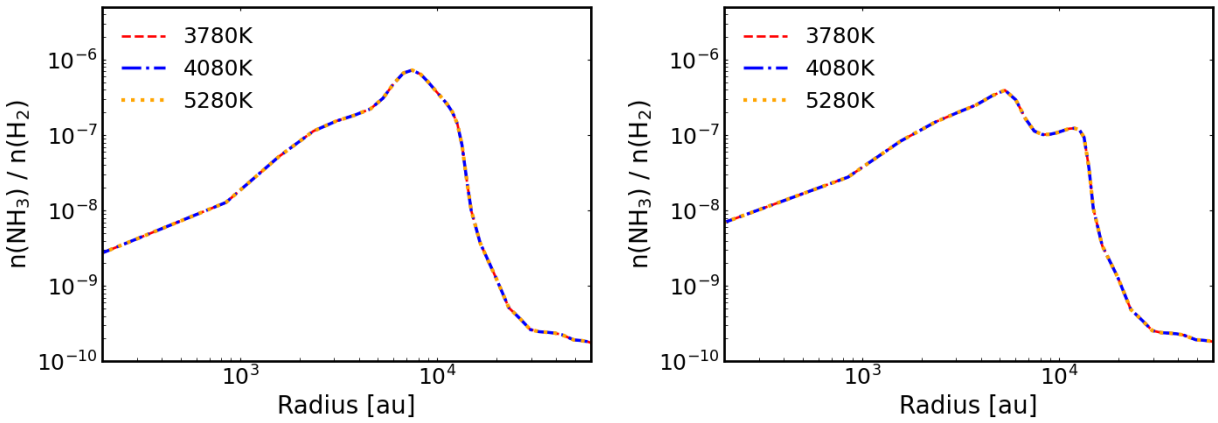

Figure 3.5: Same as figure 3.4 but using time-dependent approach to CRID.

In the second model, the dynamic approach is applied to CRID in the simulations. The abundance profiles evolved similarly to the previous case at both time steps (Fig. 3.5). The peak abundance is at the same distance from the core centre as the model with a constant CRID rate. The overall abundance throughout the core is higher than when varying CRID rate was not introduced. This is because of the effects on grain cooling time due to time-dependent ice abundances, as explained in Sipilä et al. (2021). As in the previous model, the abundance of ammonia drops beyond 10^4 AU irrespective of the presence or absence of CRID.

The important aspect between the two sets of simulations is the perfect overlap of the abundance profiles obtained for the three binding energy values, irrespective of the model. Ammonia has a high binding energy, making it even more susceptible to gas-phase depletion than other molecules. Even when using the lowest binding energy value from the experiments (3780 K), the temperatures are so low that they fall well below the desorption energy threshold required to induce ammonia desorption and, therefore, significantly affect ammonia abundances.

3.3 The protostellar core

The next step is to investigate the role of binding energy on the chemistry of a protostellar core. The source chosen is IRAS 16293-2422 - a Class 0 protostar in the ρ - Ophiuchi cloud. It is located at a distance of 120 pc (Lombardi et al. 2008). It exhibits hot corino chemistry rich in various complex organic molecules. Centimetre and mm observations have revealed the source to be a multiple-source system IRAS 16293 A and B (Wootten (1989), Mundy et al. (1992)). Source A has been further resolved into two sub-sources A1 and A2 (Wootten (1989), Chandler et al. (2005), Sadavoy et al. (2018), Maureira et al. (2020)).

3.3.1 Physical Model

The core is characterised using the model by Crimier et al. (2010) (Fig. 3.6) where the radial density profile follows as $n(H_2) \propto r^{-1.8}$ within 6900 AU from the centre, where $n(H_2)$ is the H_2 number density. Although this model does not account for the observed substructure of the source, it effectively represents data from single-dish observations. Since the goal is not to study the specific source or its substructure, but rather to understand how binding energy can affect the evolution of protostellar cores in general, this model serves as a good template for this study. In this model, the temperature of the gas rises significantly towards the interior due to both gas compression during collapse and radiation emitted by the protostar. We assume that the dust temperature and the gas kinetic temperature are equivalent. The analytical approach involves dividing the core into concentric shells like for the case of L1544, and the final results are combined radially. A two-phase (gas + ice) grain model (Fig. 3.2a) with a dust grain radius = 0.1 μm is employed, where the ice layer is treated as a single bulk entity available for desorption, without distinguishing between a mantle and surface layer. We chose the two-phase grain model over the three-phase model because, although both models produced comparable results, the 3-phase model was computationally more expensive.

The abundance profiles are obtained in two steps. First, the initial conditions corresponding to the parent cloud are obtained by running a single-point simulation with $T_{dust} = T_{gas} = 10\,K$, $n(H_2) = 10^4$ cm^{-3}, grain radius = 0.1 μm, cosmic-ray ionisation rate, $\zeta = 1.3\times e^{-17}$ s^{-1}, and visual extinction $A_V = 10$ mag. Adsorption, desorption, and photodesorption are also considered, and the simulation is allowed to proceed until a time, $t_1 = 10^6$ years, consistent with the previous work of Brünken et al. (2014) and Harju et al. (2017) on the source. At this stage, the abundances of all the species are extracted. These are then used as the initial abundances to trace the evolution of the protostellar core. Finally, the abundances of this core are extracted after an evolutionary time of $t_2 = 10^4$ years. The choice of time is arbitrary; sub-structure (e.g., a protostellar disk) is expected to form within the inner regions in a timescale of 10^4 - 10^5 years which is not taken into account by the present static physical model. Hence, an early time step (10^4 years) is selected to obtain the abundances, giving an estimate of the initial chemical conditions of the forming small-scale structures.

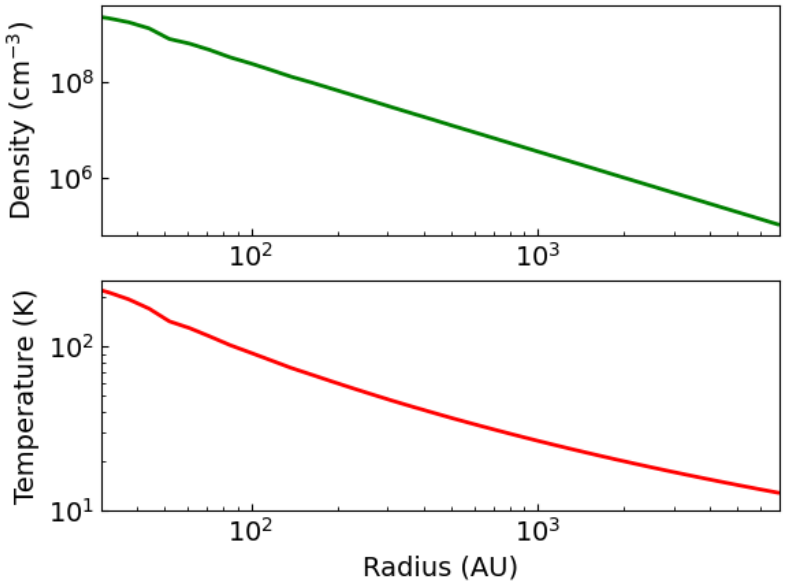

Figure 3.6: (Top) The H_2 number density and **(bottom)** the temperature distribution assumed to model IRAS 16293-2422.

3.3.2 Chemical Model

The chemical evolution of the core is monitored by the same gas-grain chemical code used for L1544. Two chemical networks are employed: the first is identical to the one used for L1544 (section 3.2.2), while the second is an expanded version of the former with additional reactions and more complex species (particularly, COMs) in both the gas-phase and on grain surfaces. Initial simulations with the smaller network showed differences in ammonia abundance profiles due to binding energy, prompting the use of the larger network to confirm whether these differences are indeed caused by variations in binding energy than the network itself. In addition, the KIDA network is also used to study the effect of proton transfer reactions on the abundances of NH_3 (Section 3.3.6). The model used is pseudo-time dependent, i.e., the chemical evolution is tracked assuming a static core. The same initial elemental abundances as for L1544 are used (Table 3.1). The binding energies for NH_3 on water ice surfaces are from Chapter 2.

3.3.3 Abundance Profiles

To investigate the impact of variations in NH_3 binding energy on the chemical composition of a protostellar core, a series of simulations are conducted where only the binding energy of NH_3 is systematically varied in each model and the resulting chemical evolution with time is traced within the core. The abundances of NH_3 are extracted at $t_2 = 10^4$ years representing the protostar at its early stages of formation.

As mentioned in Section 3.3.2, variations in NH_3 abundance profiles for different binding

energy values prompted a switch to a larger network. The results were consistent across both networks. Consequently, the larger network is employed for all subsequent studies in this work. Henceforth, only the results obtained from this network are discussed. Figure 3.7 presents the abundances of NH_3 at this time in the gas-phase (solid lines) and on grain surfaces (dashed lines) with respect to the radial distance from the centre to the outer edges of the core. The gas-phase abundance of NH_3 decreases moving radially inwards toward the centre of the core before increasing rapidly by several orders of magnitude. The abundance profile shows clear differentiation based on the value of binding energy employed. The region of high NH_3 gas-phase abundance appears closer to the centre with the radius of the desorption zone varying between 150 and 300 AU with increasing binding energy value used. The primary contributor influencing NH_3 gas-phase abundances here is thermal desorption from dust grains. As the binding energy increases, NH_3 remains on the grains until a higher temperature is reached at which point it acquires sufficient thermal energy for desorption.

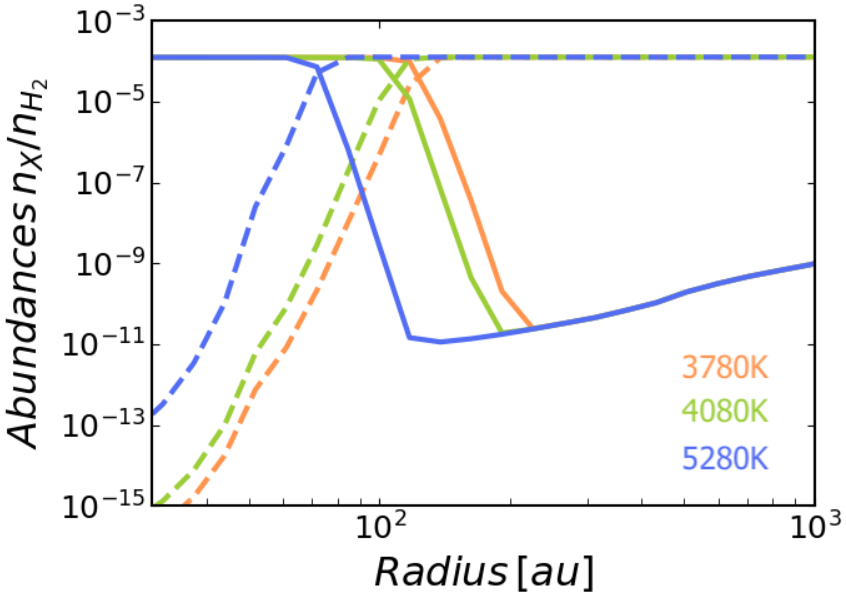

Figure 3.7: Radial abundances of NH_3 in gas phase *(solid lines)* and on grain surfaces *(dashed lines)* at 10^4 years. The binding energies of NH_3 (marked using different colours) used in each model are displayed in the lower right corner.

Notable related effects are only seen in species like HNC, CN, HCN etc (Fig. 3.8). Their abundance profiles vary within the same spatial zone where NH_3 abundances vary. The effects are directly tied via chemical reactions to the variations in the NH_3 abundances. This effect is further discussed in section 3.3.6. Furthermore, the relative abundances of key volatile compounds found in ices is analysed, namely NH_3, CO, CO_2, CH_4, and CH_3OH with respect to H_2O. These predictions are compared with the reported values in Boogert et al. (2015), but direct comparisons are challenging due to differences in the sources and uncertainties related to the parameters employed for calculating ice abundances in the cited study. Further details of these comparisons are available in appendix B.

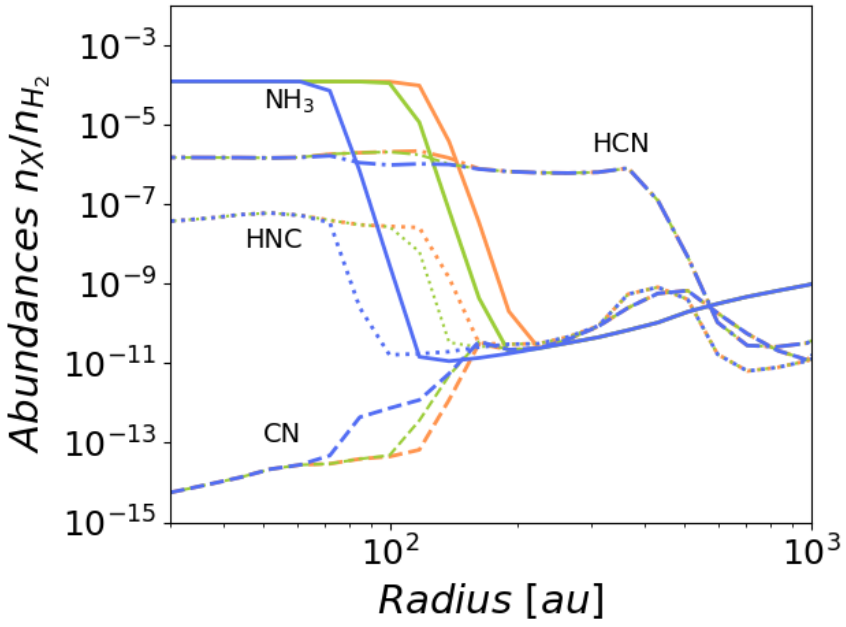

(a)

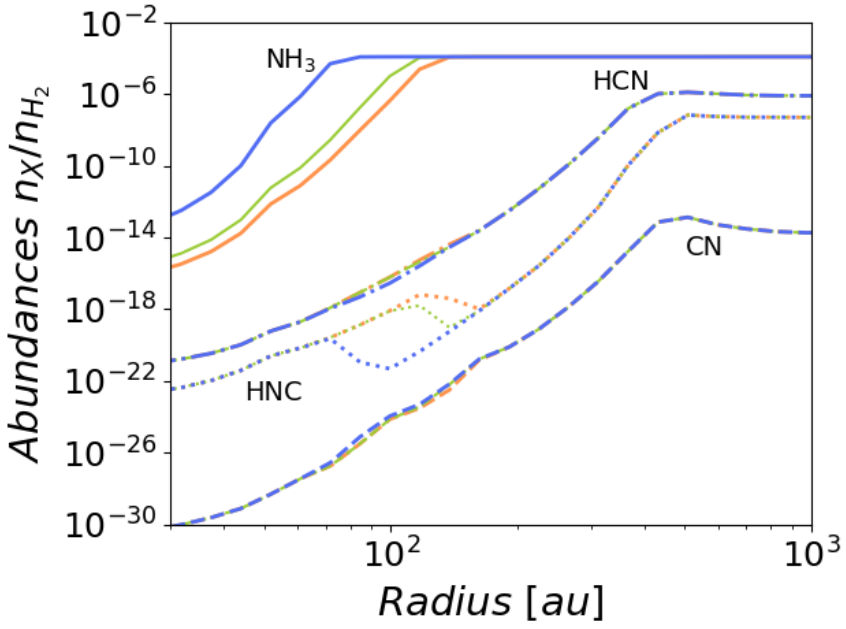

(b)

Figure 3.8: Variation in the (a) gas-phase and (b) grain abundances of NH_3, HNC, HCN and CN with binding energy. The colour scheme for the lines follows the same as in Fig. 3.7.

3.3.4 Column Density maps of NH_3

To assess the potential observational impact of the NH_3 abundance variations, NH_3 column density maps are simulated individually for each BE value. The model calculates the *or-*

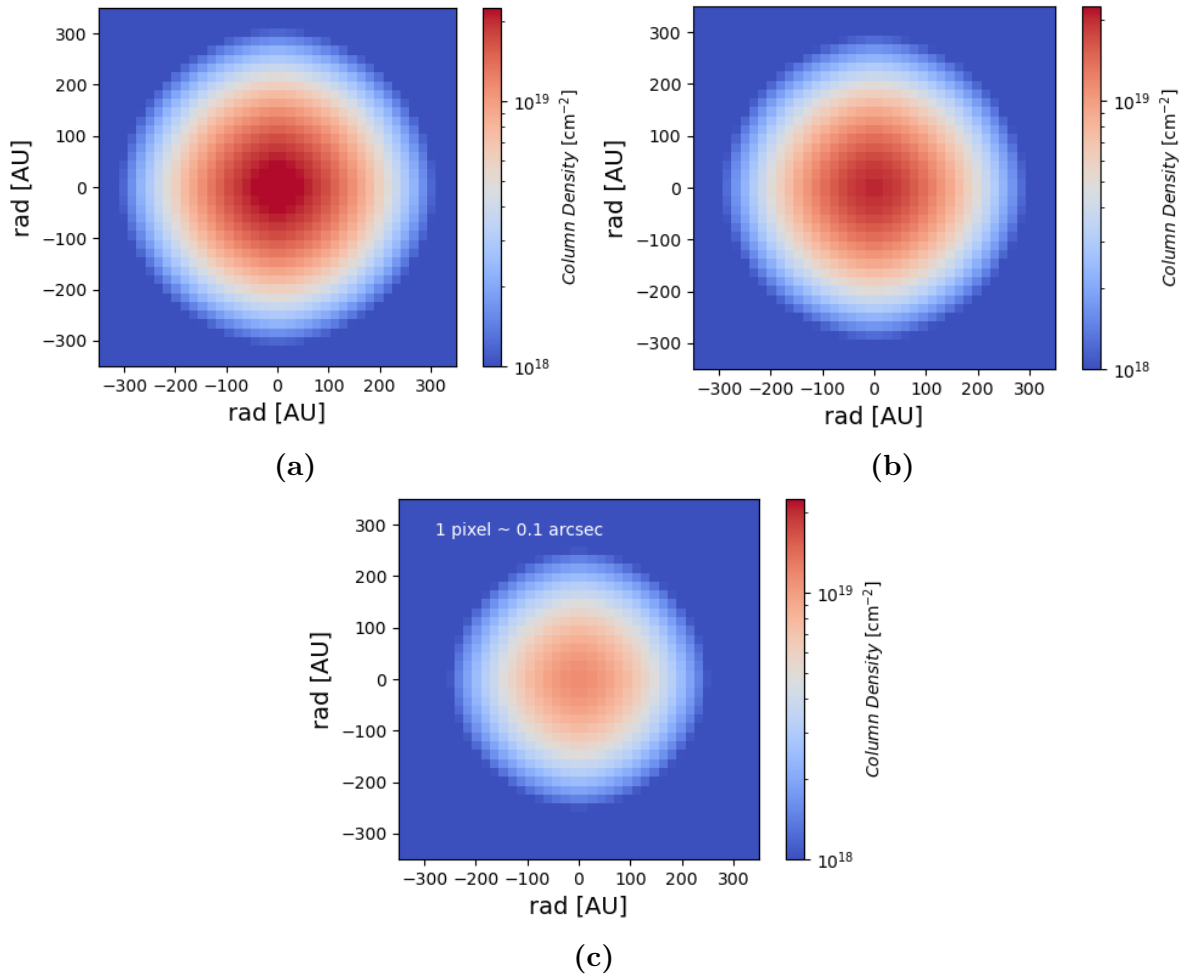

Figure 3.9: Column density map of p-NH_3 without the envelope (see text) for binding energy (a) 3870 K (b) 4080 K and (c) 5280 K. The angular size simulated by each pixel for each map is given in the top left corner of Fig. 3.9c.

tho/para- NH_3 ratio time-dependently at each point across the radius of the source. Here, only p-NH_3 is simulated to compare the column density maps against the simulated emission of the (1,1) transition of this molecule (see Sect. 3.3.5). This transition corresponds to the lowest inversion transition of NH_3 (Fig. 1.8), allowing to trace both the warm inner region and the colder outer envelope. To generate the column density maps, radial abundances of p-NH_3 obtained in the previous section are used as input, which are then interpolated to create a two-dimensional map of the cloud core. The abundances are convolved to a beam size of 2" for the object situated at 120 pc to simulate interferometric observations (the distance to IRAS 16293-2422, although this can be applied to other similar sources by simply changing the distance value). The radial distribution of column density, denoted as N, is calculated using the formula:

$$\mathrm{N} = \sum_{\mathrm{i}} \mathrm{p} \times \mathrm{X_i} \times \mathrm{n(H_2)}$$

Here, Σ represents the summation across i elements of the core model, p is the path length

through a volume element i in cm, X_i is the abundance of the species (here, p-NH_3) in i with respect to H_2, and $n(H_2)$ is the volume density of i in mol cm^{-3}. Figure 3.9 shows the 2D maps of column densities of p-NH_3 within a 300 AU radius where the binding energy-dependent variations are apparent. The radius of the desorption zone decreases as the binding energy increases. The column density as shown in Fig. 3.9 traces the part of the distribution that could only be observed with specific NH_3 lines, for example, the (1,1), (2,2), etc., inversion line. The column density maps also indicate the extent of desorbed NH_3 that will be available in the gas phase.

3.3.5 Radiative transfer studies of NH_3 (1,1) transition

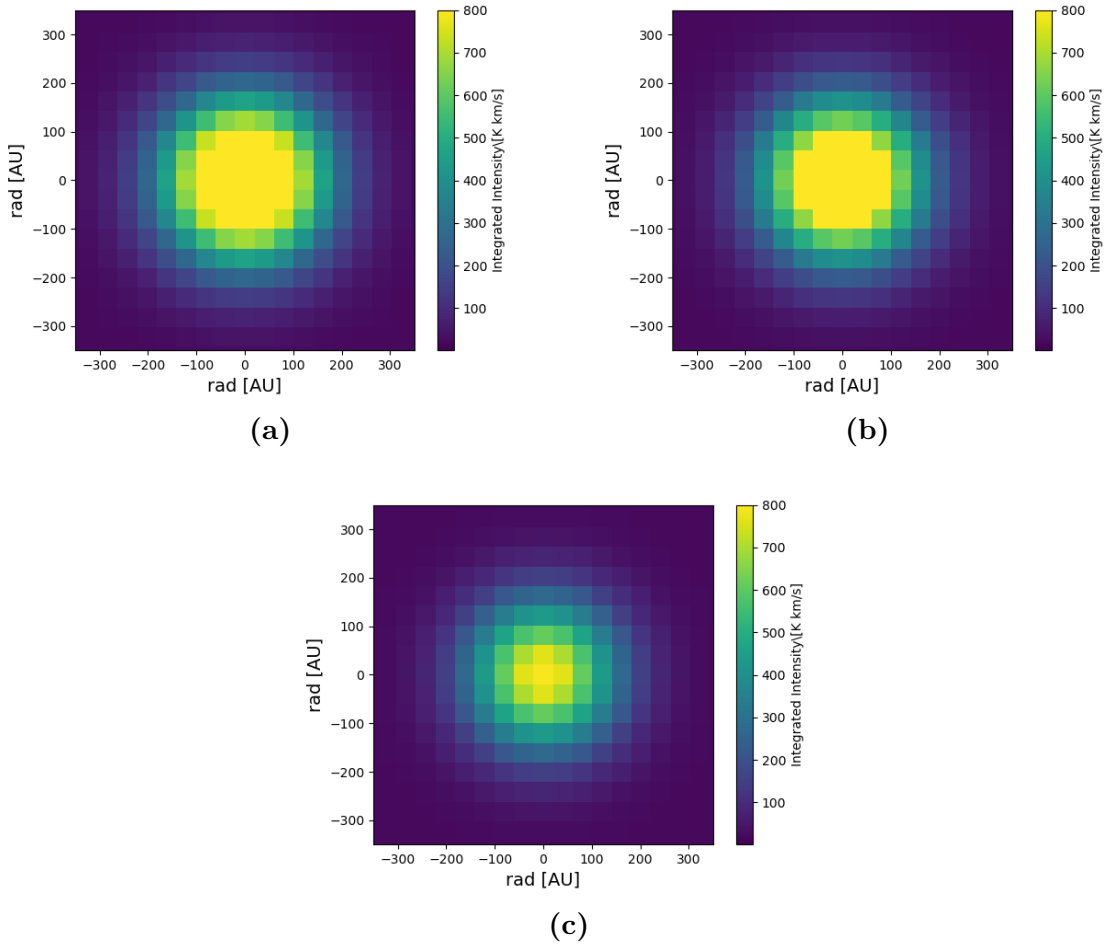

Figure 3.10: Integrated intensity map of p-NH_3 (1,1) in the core for binding energy (a) 3870 K (b) 4080 K and (c) 5280 K with envelope.

One-dimensional radiative transfer modelling of the 23 GHz (1,1) rotational-inversion transition of p-NH_3 is carried out to verify the observability of the binding energy-dependent variation in the radius of the desorption zone using the non-LTE radiative transfer code LOC (Juvela 2020). The first step in this analysis is to simulate the cloud that contains the

protostellar core and its envelope. Given that the source is a Class 0 object, the core represents a deeply embedded source surrounded by an envelope. The methodology employed to determine NH_3 abundances within the envelope closely follows the two-step approach outlined for the core in Section 3.3.1. First, the abundances corresponding to the parent cloud are obtained by running a single-point simulation for $t_1 = 10^6$ years under the same conditions as the parent cloud, similar to that described in Section 3.3.1. After extracting the NH_3 abundances at this stage, a second single-point simulation is run for $t_2 = 10^4$ years, this time using the specific physical conditions for the envelope. These conditions include an envelope thickness set to obtain a visual extinction, $A_V = 5$ mag, $n(H_2) = 10^4$ m^{-3} and $T = 10$ K. The modelling is done taking into consideration the 18 hyperfine components of p-NH_3. The spectra are obtained for 1000 lines of sight across the radius of the whole object. Each spectrum is then convolved to a synthesised beam of 2". The intensity of the transition from these spectra is integrated and interpolated to create a two-dimensional intensity map (Fig. 3.10) assuming spherical symmetry.

The collisional and radiative rate coefficients for the p-NH_3 line simulations were taken from the LAMDA database (Schöier et al. 2005). The provided coefficients (collisional data from Danby et al. (1988)) do not resolve the hyperfine structure, and hence the coefficients for the individual hyperfine components are assumed to be distributed according to LTE. To investigate the potential effect of hyperfine-resolved collisional rate coefficients on the results, another series of line simulations are performed adopting instead the set of collisional rate coefficients presented recently by Loreau et al. (2023). The hyperfine-resolved radiative transition frequencies and Einstein A coefficients were derived from data in the CDMS (Endres et al. 2016). These two approaches led only to small differences in simulated lines, and in what follows the results of simulations carried out using the data originating in LAMDA are presented.

In each model, the peak intensity is centrally concentrated and declines going outwards. The location and size of this zone are in good agreement with the simulations of the column densities (Fig. 3.9), despite optical thickness effects that were missed by calculating the column density directly from the simulated abundances. Predominantly, the intensity originates from the inner zone due to elevated NH_3 gas-phase abundance, as indicated by the abundance profiles (Fig. 3.7). Moreover, the size of the emitting region diminishes with higher binding energy, attributed to a reduction in gas-phase NH_3 concentrations associated with increasing binding energy. Similar results are obtained for radiative transfer models using the (2,2) and (3,3) lines (not shown).

Convolutions of the spectra for the (1,1) transitions at larger beam sizes are also conducted to evaluate the observability of this variation in the size of the emitting region. However, these effects become discernible only with beam sizes of 10 arcsec or smaller. This highlights the need for higher-resolution observations to detect such subtleties in the star-formation process. When convolved with a 6 arcsec beam, similar to the observations by Mundy et al. (1990), brightness temperatures lower than but within a factor of two are obtained compared to their reported value of 16.5 K for the NH_3 (1,1) emission towards the brightest regions of their source - IRAS 16293-2422.

3.3.6 Discussion

Influence of NH_3 binding energy on abundance profiles of chemically related species

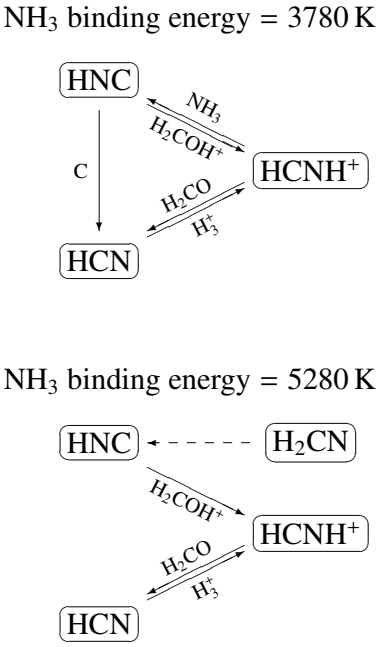

Figure 3.11: Main formation and destruction pathways of HNC as predicted by the chemical model for the two extreme binding energy (BE) values. In the lower figure (BE = 5280 K), the dashed arrow represents an alternative pathway for the formation of HNC through H-abstraction from H_2CN. This pathway becomes prominent when the gas-phase abundance of NH_3 is low, thereby inhibiting the formation via the reaction between NH_3 and $HCNH^+$.

Interestingly, notable effects are observed on other species and their abundance profiles within the same zone where NH_3 abundances vary. A few examples are demonstrated in Fig. 3.8. The abundance profiles of these species vary depending on the chosen binding energy of NH_3. To understand this, consider the example of HNC (Fig. 3.11). In the inner regions of the model with binding energy = 3780 K, HNC is efficiently produced through the reaction between $HCNH^+$ and NH_3, yielding HCN and HNC. $HCNH^+$ originates from HCN through the interaction with H_3^+ and can revert to HCN via reactions between $HCNH^+$ and H_2CO (and $HCNH^+ + NH_3$). Hence, the connection between HCN and HNC follows the sequence $HCN \rightarrow HCNH^+ \rightarrow HNC$, where the first step involves H_3^+, and the second step involves NH_3.

In contrast, in the model with binding energy = 5280 K, the gas phase abundance of NH_3 is low, which effectively closes off the $HCNH^+ + NH_3$ route. HNC is being created instead via H-abstraction from H_2CN (dashed arrow in Fig. 3.11), but at approximately ∼10% of the rate of the NH_3 route of the previous model; HNC formation is severely inhibited by the lack of available NH_3. This can be seen in Fig. 3.8 where the shape of the HNC abundance

profile follows that of NH_3. Simultaneously, the rate of the reaction $HCNH^+ + H_2CO \rightarrow HCN + H_2COH^+$ increases (as the $HCNH^+$ destruction channel with NH_3 is absent). These findings support the importance of further investigations into the role of NH_3 binding energy in the abundances of various species in the protostellar core.

Effect of Proton Transfer reactions on NH_3 abundances

Taquet et al. (2016) demonstrated that methanol abundances are significantly enhanced through proton transfer reactions involving NH_3, as compared to simulations lacking NH_3. Subsequently, the following reaction is introduced into the present network

$$CH_3OH_2^+ + NH_3 \longrightarrow CH_3OH_{gas} + NH_4^+$$

derived from the network outlined in their research, which contributes to the synthesis of dimethyl ether (CH_3OCH_3) or methyl formate (CH_3OCHO). New chemical simulation are run with this reaction included, where only NH_3 binding energies are varied, to investigate potential effects on methanol abundances. For this test, the KIDA network (Wakelam et al. 2015) is used in place of the full deuterium and spin-state containing networks from this work, for two main reasons: 1) to check if the overall conclusions on the binding energy-dependent NH_3 desorption region remain unaffected regardless of the chemical network used (i.e., that the presence of deuterium and spin states does not affect the conclusions to a significant degree); and 2) to search for potential effects on some complex organic molecules (COMs) that are not included in the fiducial chemical network (for example, CH_3OCH_3, CH_3CH_2OH, etc). The grain-surface network used in this test is the same as the fiducial one used previously in this work, but with deuterium and spin states removed.

In the investigation of Taquet et al. (2016), protonation by NH_3 extended the survival time of methanol from 10^4 years to 10^5 years. In the present study, methanol remained for up to 10^6 years even without their reaction integrated into the KIDA network. Upon inclusion of their reaction, the simulations validated their results, showing an increase in methanol abundances of up to two orders of magnitude for a specific binding energy value. However, this enhancement became noticeable only beyond 10^6 years. Analysis of abundances for different binding energy values at a specific time step revealed marginal variations in methanol abundances, even at 10^6 years, where the most substantial difference emerged between simulations with and without the proton-transfer reaction. The discrepancy in the evolutionary time in the current model versus that of Taquet et al. (2016) regarding when the effect on CH_3OH becomes apparent is very likely due to different simulation parameters. The goal of this test is not to attempt a one-to-one simulation with the aim of duplicating their results. Nevertheless, the comparison indicates that proton-transfer reactions can be very important and should be explored in more detail in later simulations.

3.4 Conclusions

In Chapter 2, a distribution of binding energy of NH_3 on different water ice substrates is calculated, in contrast to past studies that proposed a single value for NH_3. Given that binding energy is a crucial parameter for determining the abundance and chemistry of a

species in the ISM, it is essential to examine the significance of this distribution in real astrophysical scenarios. For this purpose, in this chapter, gas-grain astrochemical networks are employed in the physical models of a pre- and protostellar core, which represent the earliest stages of star formation, varying only the binding energy in each case.

For the pre-stellar core, where temperatures are low, non-thermal desorption mechanisms are also incorporated, specifically cosmic ray induced desorption. Two models for cosmic ray induced desorption are employed: a static model with constant cooling and heating intervals, and a dynamic model where cooling depends on time-dependent ice abundances and the heating interval varies as a function of visual extinction. The results show that ammonia abundance increases going outwards from the core before decreasing as it reaches the outer edges of the core. However, varying the binding energy has no impact on the abundance profiles of NH_3 in each case. This could be attributed to the high binding values of NH_3, which are too high for the low temperatures in the core for effectively desorbing it from the grain.

In a protostellar core, a distinct dependence of NH_3 abundance profiles on the binding energy employed is seen, particularly in the warm, inner regions of the model. This variation, consequently, influences other key species, including HCN, HNC, and CN, where the NH_3 abundance dictates the preferred pathway for their formation. However, in proton transfer reactions involving NH_3, expected to enhance methanol formation, the abundance variation of NH_3 due to binding energy does not appear to be a significant contributing factor.

Simulation of column density maps for p-NH_3 reveals that the size of the desorption region diminishes as the binding energy increases. These findings align with radiative transfer studies on the (1,1) inversion line of NH_3, where an envelope is added to the physical model to examine absorption and emission effects. In these studies, the peak intensity is centrally concentrated and decreases outward. Additionally, the intensity diminishes with higher binding energy due to a reduction in gas-phase NH_3. These results highlight the importance of considering diverse binding energies in astrochemical models, providing a refined understanding of molecular cloud chemistry and star formation processes.

Bibliography

Boogert, A. A., Gerakines, P. A., & Whittet, D. C. 2015, Annual Review of Astronomy and Astrophysics, 53, 541

Brünken, S., Sipilä, O., Chambers, E. T., et al. 2014, Nature, 516, 219

Caselli, P., Pineda, J. E., Zhao, B., et al. 2019, The Astrophysical Journal, 874, 89

Chandler, C. J., Brogan, C. L., Shirley, Y. L., & Loinard, L. 2005, The Astrophysical Journal, 632, 371

Crabtree, K. N., Indriolo, N., Kreckel, H., Tom, B. A., & McCall, B. J. 2011, The Astrophysical Journal, 729, 15

Crapsi, A., Caselli, P., Walmsley, C., & Tafalla, M. 2005, Astrochemistry: Recent Successes and Current Challenges, 231, 193

Crapsi, A., Caselli, P., Walmsley, M. C., & Tafalla, M. 2007, , 470, 221

Crimier, N., Ceccarelli, C., Maret, S., et al. 2010, Astronomy & Astrophysics, 519, A65

Danby, G., Flower, D., Valiron, P., Schilke, P., & Walmsley, C. 1988, Monthly Notices of the Royal Astronomical Society, 235, 229

Endres, C. P., Schlemmer, S., Schilke, P., Stutzki, J., & Müller, H. S. P. 2016, Journal of Molecular Spectroscopy, 327, 95

Galli, P., Loinard, L., Bouy, H., et al. 2019, Astronomy & Astrophysics, 630, A137

Garrod, R. & Herbst, E. 2006, Astronomy & Astrophysics, 457, 927

Garrod, R., Wakelam, V., & Herbst, E. 2007, Astronomy & Astrophysics, 467, 1103

Grassi, T., Bovino, S., Caselli, P., et al. 2020, Astronomy & Astrophysics, 643, A155

Harju, J., Sipilä, O., Brünken, S., et al. 2017, The Astrophysical Journal, 840, 63

Hasegawa, T. I. & Herbst, E. 1993a, Monthly Notices of the Royal Astronomical Society, 261, 83

Hasegawa, T. I. & Herbst, E. 1993b, Monthly Notices of the Royal Astronomical Society, Vol. 263, NO. 3/AUG1, P. 589, 1993, 263, 589

Jiménez-Serra, I., Vasyunin, A. I., Caselli, P., et al. 2016, The Astrophysical Journal Letters, 830, L6

Juvela, M. 2020, Astronomy & Astrophysics, 644, A151

Kakkenpara Suresh, S., Sipila, O., Caselli, P., & Dulieu, F. 2024b, arXiv preprint arXiv:2407.17891

Keto, E. & Caselli, P. 2010, Monthly Notices of the Royal Astronomical Society, 402, 1625

Lee, C. W., Myers, P. C., & Tafalla, M. 1999, , 526, 788

Leger, A., Jura, M., & Omont, A. 1985, Astronomy and Astrophysics (ISSN 0004-6361), vol. 144, no. 1, March 1985, p. 147-160. Research supported by the University of California and NASA., 144, 147

Lombardi, M., Lada, C. J., & Alves, J. 2008, Astronomy & Astrophysics, 480, 785

Loreau, J., Faure, A., Lique, F., Demes, S., & Dagdigian, P. J. 2023, , 526, 3213

Maureira, M. J., Pineda, J. E., Segura-Cox, D. M., et al. 2020, The Astrophysical Journal, 897, 59

Mundy, L. G., Wooten, A., Wilking, B. A., Blake, G. A., & Sargent, A. I. 1992, Astrophysical Journal, 385, 306

Mundy, L. G., Wootten, H., & Wilking, B. A. 1990, Astrophysical Journal, Part 1 (ISSN 0004-637X), vol. 352, March 20, 1990, p. 159-166., 352, 159

Padovani, M., Ivlev, A. V., Galli, D., & Caselli, P. 2018, Astronomy & Astrophysics, 614, A111

Redaelli, E., Bizzocchi, L., Caselli, P., et al. 2019, Astronomy & Astrophysics, 629, A15

Sadavoy, S. I., Myers, P. C., Stephens, I. W., et al. 2018, The Astrophysical Journal, 869, 115

Schöier, F. L., van der Tak, F. F. S., van Dishoeck, E. F., & Black, J. H. 2005, , 432, 369

Semenov, D., Hersant, F., Wakelam, V., et al. 2010, Astronomy & Astrophysics, 522, A42

Sipilä, O. 2012, Astronomy & Astrophysics, 543, A38

Sipilä, O., Caselli, P., & Harju, J. 2015a, Astronomy & Astrophysics, 578, A55

Sipilä, O., Harju, J., Caselli, P., & Schlemmer, S. 2015b, Astronomy & Astrophysics, 581, A122

Sipilä, O., Hugo, E., Harju, J., et al. 2010, Astronomy & Astrophysics, 509, A98

Sipilä, O., Silsbee, K., & Caselli, P. 2021, The Astrophysical Journal, 922, 126

Spezzano, S., Caselli, P., Bizzocchi, L., Giuliano, B., & Lattanzi, V. 2017, Astronomy & Astrophysics, 606, A82

Taquet, V., Wirström, E. S., & Charnley, S. B. 2016, The Astrophysical Journal, 821, 46

Vastel, C., Quénard, D., Le Gal, R., et al. 2018, Monthly Notices of the Royal Astronomical Society, 478, 5514

Wakelam, V., Loison, J.-C., Herbst, E., et al. 2015, The Astrophysical Journal Supplement Series, 217, 20

Wootten, A. 1989, The Astrophysical Journal, 337, 858

4

Ammonia formation via successive N hydrogenation on grain surfaces

4.1 Introduction

In the previous chapters, we explored the surface behaviour of ammonia, examining its reactivity in mixed ices and determining its binding energy values, both of which significantly influence ammonia chemistry in grain-surface and gas-phase processes. Despite these insights, a significant gap remains in our understanding: the formation of ammonia on dust grains and its contribution to the observed gas-phase ammonia abundance in the ISM, especially in cold, dark molecular clouds where dust grains are key to regulating chemistry.

Although the gas-phase formation of ammonia has been extensively studied (Herbst & Klemperer 1973; Herbst et al. 1987; Le Gal et al. 2014; Gerin et al. 2016), these pathways alone cannot account for the observed abundances of ammonia and its intermediates (Hily-Blant et al. 2010; Goicoechea et al. 2004). Research indicates that many molecules, including ammonia (Fedoseev et al. 2015), water (Dulieu et al. 2010, 2013), formaldehyde (Molpeceres et al. 2021), methanol (Watanabe & Kouchi 2002; Rimola et al. 2014), and ethanol (Chuang et al. 2021; Perrero et al. 2022) can form efficiently on grain surfaces.

Hydrogenation processes, which are among the most efficient grain-surface reactions in cold molecular clouds, could offer a potential explanation. Previous studies, such as those by Hiraoka et al. (1995) and Hidaka et al. (2011), have shown that ammonia can indeed form at low temperatures through the hydrogenation of nitrogen atoms on grain surfaces. However, these experiments were conducted on an N_2 matrix, which does not accurately represent the ice composition in astrophysical environments, and they did not report the detection of important intermediates like NH and NH_2. Subsequent studies, including those by Nourry

& Krim (2016), demonstrated that NH_2 can be formed at 10 K through the reaction of NH_3 with $N(^4S)$ atoms, and Jonusas et al. (2020) reported the detection of both NH and NH_2 under similar low-temperature conditions. Nonetheless, the formation pathways of ammonia and these intermediates remain ambiguous, as it is unclear whether they indeed result from successive hydrogenation or other mechanisms.

Through the work described in this Chapter, we aim to address these uncertainties by investigating the formation pathways of ammonia on dust grains, with a particular focus on the hydrogenation of nitrogen atoms. By combining experimental data with modelling, we seek to provide a more comprehensive understanding of ammonia chemistry in the interstellar medium. In the following sections, we present the methodology, discuss preliminary results, and outline the future steps for this ongoing research.

4.2 Calibration and Preliminary Results

4.2.1 Experimental Approach

Characterisation of the molecular beams

The formation of ammonia is probed experimentally using the VENUS setup described in Chapter 2. The experiment consists of depositing N and H atoms onto the deposition surface and monitoring the experiment via FTIR. This is done by introducing molecular beams of N_2 and H_2 into the main chamber through separate beamlines. To convert these molecular species into their atomic forms, a microwave discharge is employed in each beamline for dissociation. Before starting the experiments, we will first identify the optimal conditions to maximise dissociation efficiency for each species. To find the conditions that yield the maximum stable dissociation efficiency, we will systematically vary experimental parameters such as beam flux and microwave discharge power. The resulting variation in the flux of each molecular/atomic species will be monitored using a QMS. The dissociation efficiency, τ, is calculated using the following formula from Congiu et al. (2020):

$$\tau = \frac{S_{OFF} - S_{ON}}{S_{OFF}} \tag{4.1}$$

Here, S_{OFF} and S_{ON} represent the counts of the parent molecular species detected by the QMS when the discharge is turned OFF and ON, respectively.

Optimal N atom dissociation conditions

We present here the results from preliminary tests conducted on N_2 dissociation using the VENUS setup described in Chapter 2. These results provide qualitative insights rather than precise quantitative measurements. Further testing will be done for accurate quantification.

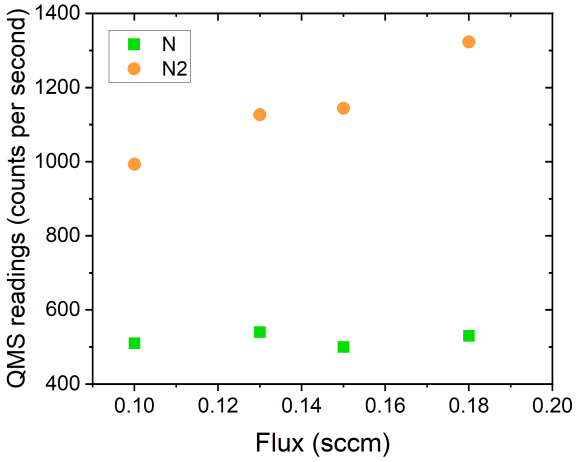

(a) Resultant N_2 and N atom QMS fluxes for different injected molecular N_2 fluxes for a constant microwave discharge power of 80W.

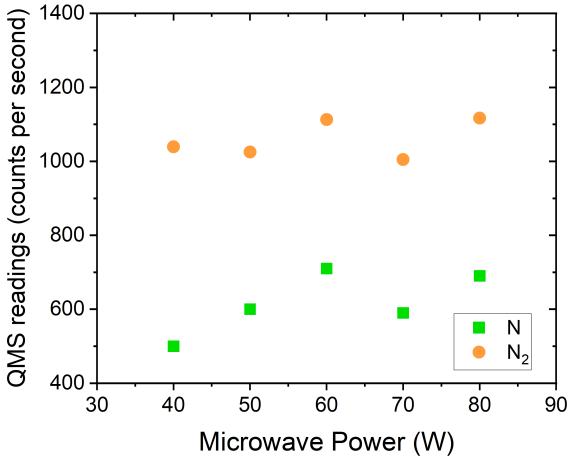

(b) Same as 4.1a but varying the microwave discharge power and maintaining a constant flux of 0.1 sccm.

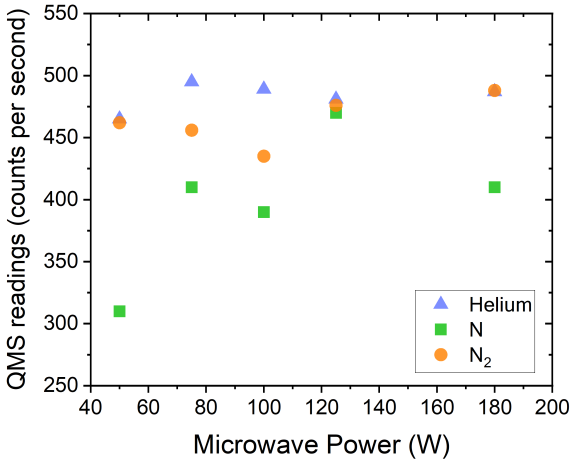

(c) Variation in N_2 dissociation efficiency with microwave power after the addition of Helium gas maintaining a constant flux of 0.1 sccm.

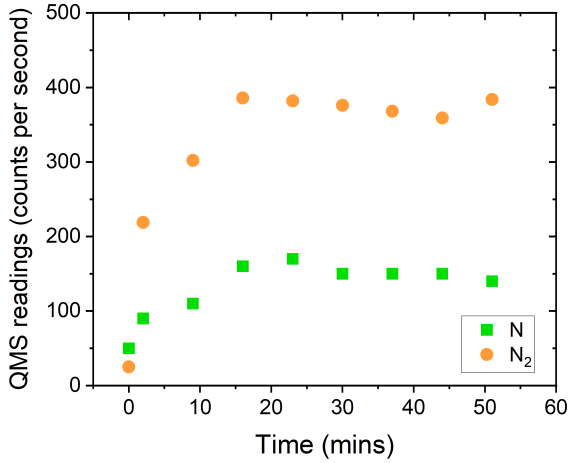

(d) Plot showing time required by the N_2 jet to achieve stable dissociation for a flux of 0.1 sccm.

Figure 4.1: Plots representing preliminary tests conducted to characterise the N_2 molecular beam. The N atom abundances have been scaled up by a factor of 10 for visual convenience.

Figure 4.1a illustrates how the N atom flux varies with different input fluxes of the N_2 molecular beam, using a constant microwave power of 80 W. Our results suggest that the flux of N atoms is higher when the input flux is below 0.13 sccm. At higher input fluxes, the relative amount of N atoms decreases, likely due to the recombination of N atoms into N_2, as higher fluxes increase the collision frequency with other N atoms leading to the formation of the more stable N_2 molecules. Figure 4.1b depicts the variation in N atom flux with changing microwave discharge power while keeping the N_2 flux constant at 0.1 sccm. At low microwave powers, the production of N atoms is low. Beyond 60 W, the flux of N atoms

increases, and the ratio of N atoms remains relatively constant with increasing power.

Figure 4.1c presents the effect of introducing a buffer gas, helium, into the beamline carrying N_2. The buffer gas, at a pressure of a few 10^{-6} mbar, helps reduce N atom recombination by cooling the atoms through collisions. The results show that, with a constant flux of 0.1 sccm, the N atom flux increases with microwave power up to 120 W, beyond which the flux decreases. Figure 4.1d shows the stability of the N atom flux over time. Stability is achieved approximately 20 minutes after the discharge is switched on and remains stable for at least 30 minutes. Additional tests are planned to assess stability over longer duration.

Using Eq. 4.1, we obtained a maximum N_2 dissociation efficiency of approximately 5% in each set of experiments, both with and without He. This value aligns with the results reported in Congiu et al. (2020), but it falls within the error margin for background noise in the system. A better efficiency would correspond to a value of at least 30-40% since this would give approximately equal amounts of N atoms and N_2 molecules. To improve the efficiency, we conducted tests on the ultra-high vacuum setup, FORMOLISM (Amiaud et al. 2007; Congiu et al. 2012), which is similar to VENUS. FORMOLISM can reach base pressures of 10^{-10} mbar and is equipped with a QMS, an FTIR, and a microwave discharge setup. Unfortunately, these tests did not yield reproducible results. Although N_2 dissociation occurred in the beamlines, the QMS detected only N_2 molecules and no N atoms. We attempted several adjustments, including moving the dissociated N_2 plasma closer to the beamline exit, introducing a flag to reduce the flux of N_2, and repositioning the deposition surface nearer to the beamline. Despite these efforts, we still could not detect any N atoms. Due to the time constraints of this PhD schedule, which allocates 18 months at Cergy, France, for experimental work and the remaining time at Garching, Germany, we were unable to continue these tests further.

4.2.2 Calibration of the Astrochemical Model

To gain a deeper understanding of the hydrogenation process observed in our experiments, we aim to simulate the experiments using a gas-grain astrochemical model. This modelling approach will allow us to identify key reaction pathways, formation of other potential products, and examine the effect of short-lived reaction intermediates that might not be detectable via FTIR. We use the code, *pyRate*, for this study.

Before conducting full simulations, we first calibrate the gas-grain code using a three-phase model (as in Section 3.2.1) for the ice chemistry. This model is particularly advantageous because it can not only treat the surface layer as chemically active, which aligns with the experimental conditions where reactions occur predominantly on the surface but also be used to study chemistry happening in multiple surface layers in the experiments.

The calibration process involves estimating the optimal value of n, which is a parameter in the model that denotes the volume density (in cm^{-3}). The objective is to find the value of n that results in the formation of a surface layer (similar to a monolayer from experiments), at a grain temperature of 10 K, within the same time frame (i.e., $\sim$ 10 mins) observed in the experiments. This is done to fine-tune the model parameters to match the incoming flux of the species as in the experiments. We used a single species (in this case, N atoms) in

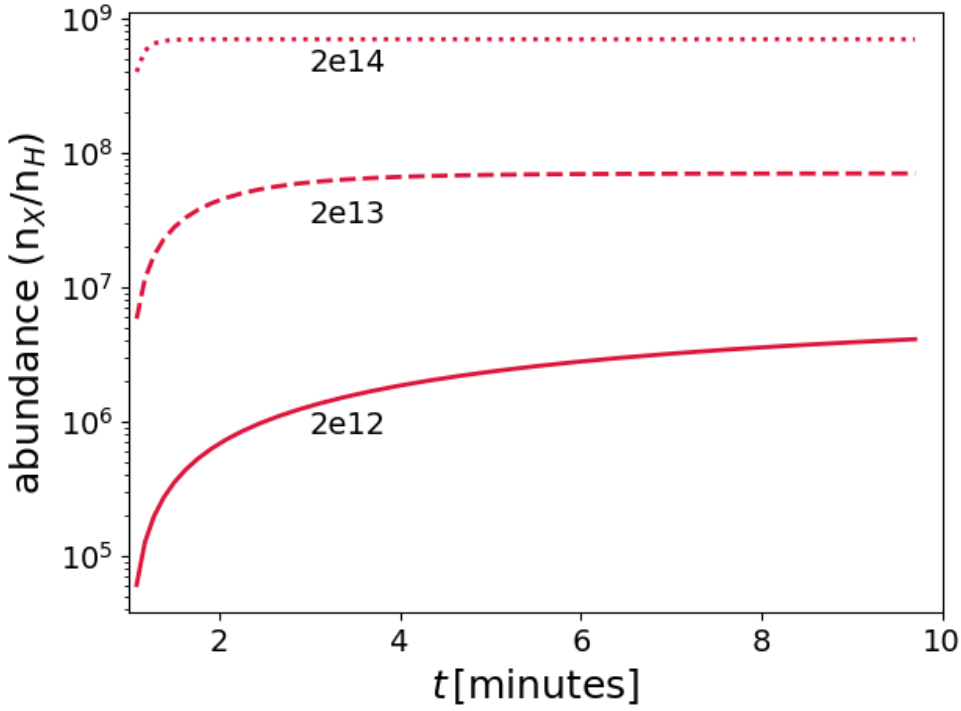

Figure 4.2: Figure representing different abundances of N atoms injected values of gas density, n, used to calibrate for the formation of a surface layer.

the network for the calibration, mirroring the monolayer calibration procedure used in the experimental setup in Chapter 2. The abundance of N is expressed relative to this density, n.

Figure 4.2 illustrates the results of our calibration, showing the variation in the surface abundance of N for different n values. Our objective is to estimate an n value at which the surface coverage plateaus around 10 minutes, indicating a saturated surface as in the experiments. At high densities, such as $n = 2{\times}10^{14}$ cm^{-3}, the abundance curve reaches a plateau in under 2 minutes, indicating that the surface layer has fully formed within this brief time. As we decrease n, the time required to form a complete surface layer gradually increases. At a lower density, $n = 2{\times}10^{12}$ cm^{-3}, the surface layer coverage continues to rise beyond 10 minutes, indicating incomplete surface formation. At $n = 2{\times}10^{13}$ cm^{-3}, the surface coverage slowly increases forming a plateau around 10 minutes. Consequently, we determined that a monolayer is formed at approximately $n = 2{\times}10^{13}$ cm^{-3} in our model. This density will be used consistently in all subsequent simulations and will serve as the basis for calibrating the abundance of other species. The purpose of this test is to establish an approximate value for n which will be fine-tuned in later tests for greater precision.

4.3 Strategies for Experiments and Model Development

Experimental study of N + H reactions

In the next phase of the experiment, we will co-deposit dissociated beams of N_2 and H_2 onto a surface maintained at 10 K. We will perform the codeposition for various N:H ratios, for example, 10:90, 25:75, 50:50, 75:25, and 90:10 to study the effect of varying the N:H ratios on the hydrogenation process. Using an FTIR spectrometer, we will monitor the variation in abundances of N_2, H_2, NH, NH_2, and NH_3, and other species possibly formed during the experiment. The data will be analyzed to determine how NH_3 yield varies with the N:H ratio, examine the abundance variations of intermediates such as NH and NH_2 across different ratios, and assess the impact of using a realistic N:H ratio on both NH_3 yield and intermediate abundances.

Additionally, the co-deposition experiments will be replicated at substrate temperatures of 6 K and 15 K. The temperatures are chosen to represent the temperatures in the inner and outer regions of molecular clouds. This will help us understand how varying substrate temperatures influence the formation of NH, NH_2, and NH_3, to determine whether lower temperatures favour the production of intermediates or enhance the formation of the final product, NH_3.

The data from each of these experiments - across different temperature conditions and N ratios - will be analysed to identify trends in species formation, with a particular focus on optimising NH_3 yield and understanding the behaviour of intermediate species.

Initial modelling tests using N + H reaction network

With the model calibrated, we will replicate the hydrogenation experiments by constructing a simplified chemical network. This network includes both gas-phase and grain-surface reactions involving nitrogen (N), hydrogen (H), and a variety of species containing these elements. This custom chemical network, which includes the relevant species, will be expanded to incorporate additional reactions and processes as needed.

We replicate the experimental procedures by tracking the abundances of NH_3 and other relevant species over time at different surface temperatures, which, in the model, corresponds to varying the dust grain temperature. To further explore the effects of the N:H ratio on NH_3 formation, we adjust the initial atomic N and H abundances in the model, mirroring the ratios employed in the experimental section. This approach allows us to systematically evaluate how different conditions influence the formation of NH_3 and related species.

4.4 Future Directions

Moving forward, our experimental focus will be on refining the parameters for maximising N (and H) atom dissociation and continuing co-deposition studies to optimise ammonia formation via hydrogenation. On the modelling side, the goal is to extend our chemical

network to include additional nitrogen and hydrogen interactions. This expansion will enable a more comprehensive analysis of NH_3 formation and its related species, providing insights that can be integrated into models of astrophysical environments, such as pre- and protostellar cores discussed in Chapter 3. As a result of combining both experimental and modelling approaches, we may identify new reactions that are not part of existing networks, and which may be important in chemical evolution in varying conditions. Additionally, we aim to develop a code designed to complement experimental work broadly, offering support for understanding experimental chemistry and serving as a useful tool for the wider scientific community.

Bibliography

Amiaud, L., Dulieu, F., Fillion, J.-H., Momeni, A., & Lemaire, J. 2007, The Journal of chemical physics, 127

Chuang, K.-J., Fedoseev, G., Scirè, C., et al. 2021, Astronomy & Astrophysics, 650, A85

Congiu, E., Chaabouni, H., Laffon, C., et al. 2012, The Journal of chemical physics, 137

Congiu, E., Sow, A., Nguyen, T., Baouche, S., & Dulieu, F. 2020, Review of Scientific Instruments, 91, 124504

Dulieu, F., Amiaud, L., Congiu, E., et al. 2010, Astronomy & Astrophysics, 512, A30

Dulieu, F., Congiu, E., Noble, J., et al. 2013, Scientific reports, 3, 1338

Fedoseev, G., Ioppolo, S., Zhao, D., Lamberts, T., & Linnartz, H. 2015, Monthly Notices of the Royal Astronomical Society, 446, 439

Gerin, M., Neufeld, D. A., & Goicoechea, J. R. 2016, , 54, 181

Goicoechea, J. R., Rodríguez-Fernández, N. J., & Cernicharo, J. 2004, The Astrophysical Journal, 600, 214

Herbst, E., DeFrees, D., & McLean, A. 1987, Astrophysical Journal, Part 1 (ISSN 0004-637X), vol. 321, Oct. 15, 1987, p. 898-906., 321, 898

Herbst, E. & Klemperer, W. 1973, , 185, 505

Hidaka, H., Watanabe, M., Kouchi, A., & Watanabe, N. 2011, Physical Chemistry Chemical Physics, 13, 15798

Hily-Blant, P., Maret, S., Bacmann, A., et al. 2010, Astronomy & Astrophysics, 521, L52

Hiraoka, K., Yamashita, A., Yachi, Y., et al. 1995, Astrophysical Journal, Part 1 (ISSN 0004-637X), vol. 443, no. 1, p. 363-370, 443, 363

Jonusas, M., Leroux, K., & Krim, L. 2020, Journal of Molecular Structure, 1220, 128736

Le Gal, R., Hily-Blant, P., Faure, A., et al. 2014, , 562, A83

Molpeceres, G., Kastner, J., Fedoseev, G., et al. 2021, The Journal of Physical Chemistry Letters, 12, 10854

Nourry, S. & Krim, L. 2016, Physical Chemistry Chemical Physics, 18, 18493

Perrero, J., Enrique-Romero, J., Martínez-Bachs, B., et al. 2022, ACS Earth and Space Chemistry, 6, 496

Rimola, A., Taquet, V., Ugliengo, P., Balucani, N., & Ceccarelli, C. 2014, Astronomy & Astrophysics, 572, A70

Watanabe, N. & Kouchi, A. 2002, The Astrophysical Journal, 571, L173

5

Summary and Future Prospects

The elemental partitioning of nitrogen in star-forming regions remains a fundamental and unresolved question in astrochemistry. This thesis investigates the chemistry of ammonia, a key nitrogen-bearing molecule found in both the gas phase and in ices, and thought to be one of the primary nitrogen reservoirs. While ammonia has been detected across a wide range of astrophysical environments, its chemistry, especially on the surfaces of interstellar grains, remains poorly understood. This knowledge gap limits our ability to fully comprehend the role of ammonia in the nitrogen cycle within star-forming regions. To address this, the research presented here focuses on the surface chemistry of ammonia, using a combination of experimental and modelling approaches.

In Chapter 2, we conducted experiments to investigate the desorption behaviour of ammonia in mixed ices containing H_2O, CO, and CO_2. The results revealed a reduction in the desorption rate of ammonia in the presence of water and possibly CO_2, suggesting that ammonia could remain on grains at higher temperatures than previously thought and that the presence and stability of ammonia on grains is highly sensitive to the surrounding environment. Additionally, we estimated the binding energy of ammonia from compact amorphous solid water ice and crystalline ice, finding that the binding energy is distributed across a range of values rather than being a single fixed value as previously believed. This implies that the ammonia snowline may be broader than currently assumed and leads to consider a distribution of binding energies for other species.

Building on these experimental findings, in Chapter 3, we investigated the impact of varying binding energies on the abundance of ammonia using gas-grain chemical networks, in models of pre- and protostellar cores. Our results showed that in pre-stellar cores, the low temperatures and high binding energy of ammonia mean that its gas-phase abundance remains largely unaffected by the variation in binding energy. However, in protostellar cores, the

gas-phase abundance of ammonia is sensitive to its binding energy, especially in the warm inner regions of the core: lower binding energies result in ammonia entering the gas-phase at greater distances from the central warm region, while higher binding energies keep it frozen on grains closer to the core. These variations in binding energy also influence the abundances and formation pathways of other species chemically linked to ammonia.

In Chapter 4, we presented an ongoing project to explore the formation of ammonia through the hydrogenation of nitrogen atoms on grain surfaces at low temperatures, using a combination of experimental and modelling approaches. Understanding the surface formation pathways of ammonia at such temperatures is key to comprehending its observed abundances and role in interstellar chemistry. Additionally, this study aims to refine our knowledge of relevant reaction pathways, potentially identify new ones, and evaluate the impact of short-lived reaction intermediates.

Research is a continuous journey, with each answer leading to new questions. Future directions for this work involve replicating co-deposition experiments with ammonia and other molecules such as methanol or methane, as well as broadening the scope of binding energy studies by determining the binding energy of ammonia on CO ice and investigating the binding energies of additional species. We also plan to use more sophisticated models of protostellar cores that incorporate observed structural details. Incorporating binding energy distributions into these models is another promising avenue. Additionally, investigating the role of deuterated species and spin states in ammonia formation may yield valuable findings. Simulations of experiments, including those beyond ammonia, remain largely unexplored but are crucial for a deeper understanding of the actual processes occurring in known chemistry. Therefore, we aim to develop our model in this area to benefit the broader scientific community. In addition to ammonia, further research into other nitrogen-bearing molecules, such as HCN, CH_3CN, and CH_3NH_2, could reveal differences in their chemistry, providing new insights into the elemental partitioning of nitrogen in star-forming regions.

This thesis has laid the groundwork for these future studies, proposing methodologies that are already in progress and pointing the way for continued exploration of ammonia and related species in the context of star formation.

6

Conclusions et perspectives

La partition élémentaire de l'azote dans les régions de formation d'étoiles demeure une question fondamentale et non résolue en astrochimie. Cette thèse explore la chimie de l'ammoniac, une molécule clé porteuse d'azote, présente à la fois dans la phase gazeuse et dans les glaces, et considérée comme l'un des principaux réservoirs d'azote. Bien que l'ammoniac ait été détecté dans une grande variété d'environnements astrophysiques, sa chimie, en particulier à la surface des grains interstellaires, reste encore mal comprise. Cette lacune dans les connaissances limite notre capacité à appréhender pleinement le rôle de l'ammoniac dans le cycle de l'azote au sein des régions de formation d'étoiles. Afin de combler cette lacune, la recherche présentée dans ce travail se concentre sur la chimie de surface de l'ammoniac, en combinant des approches expérimentales et de modélisation.

Dans le chapitre 2, nous avons mené des expériences pour étudier le comportement de désorption de l'ammoniac dans des glaces mixtes contenant du H_2O, du CO et du CO_2. Les résultats ont révélé une réduction du taux de désorption de l'ammoniac en présence d'eau et peut-être de CO_2, ce qui suggère que l'ammoniac pourrait rester sur les grains à des températures plus élevées qu'on ne le pensait auparavant et que la présence et la stabilité de l'ammoniac sur les grains sont très sensibles au milieu environnant. En outre, nous avons estimé l'énergie de liaison de l'ammoniac à partir de glace d'eau solide amorphe compacte et de glace cristalline, et nous avons constaté que l'énergie de liaison est répartie sur une gamme de valeurs plutôt que d'être une valeur fixe unique comme on le pensait auparavant. Cela implique que la limite de neige de l'ammoniac peut être plus large que ce que l'on suppose actuellement et conduit à envisager une distribution des énergies de liaison pour d'autres espèces.

Sur la base de ces résultats expérimentaux, nous avons étudié dans le chapitre 3 l'impact de la variation des énergies de liaison sur l'abondance de l'ammoniac en utilisant des réseaux

chimiques de grains de gaz, dans des modèles de noyaux pré- et protostellaires. Nos résultats montrent que dans les noyaux pré-stellaires, les basses températures et l'énergie de liaison élevée de l'ammoniac signifient que son abondance en phase gazeuse n'est pas affectée par la variation de l'énergie de liaison. Cependant, dans les noyaux protostellaires, l'abondance de l'ammoniac en phase gazeuse est sensible à son énergie de liaison, en particulier dans les régions chaudes internes du noyau : des énergies de liaison plus faibles font que l'ammoniac entre dans la phase gazeuse à de plus grandes distances de la région chaude centrale, tandis que des énergies de liaison plus élevées le maintiennent gelé sur les grains plus proches du noyau. Ces variations de l'énergie de liaison influencent également les abondances et les voies de formation d'autres espèces chimiquement liées à l'ammoniac.

Au chapitre 4, nous avons présenté un projet en cours visant à explorer la formation de l'ammoniac par l'hydrogénation d'atomes d'azote à la surface des grains à basse température, en utilisant une combinaison d'approches expérimentales et de modélisation. La compréhension des voies de formation de l'ammoniac à la surface à de telles températures est essentielle pour comprendre les abondances observées et le rôle de l'ammoniac dans la chimie interstellaire. En outre, cette étude vise à affiner notre connaissance des voies de réaction pertinentes, à en identifier potentiellement de nouvelles et à évaluer l'impact des intermédiaires réactionnels de courte durée.

La recherche est un voyage continu, chaque réponse conduisant à de nouvelles questions. Les orientations futures de ce travail consistent à reproduire les expériences de codéposition avec l'ammoniac et d'autres molécules telles que le méthanol ou le méthane, ainsi qu'à élargir le champ des études sur l'énergie de liaison en déterminant l'énergie de liaison de l'ammoniac sur la glace de CO et en étudiant les énergies de liaison d'autres espèces. Nous prévoyons également d'utiliser des modèles plus sophistiqués de noyaux protostellaires qui intègrent les détails structurels observés. L'intégration des distributions d'énergie de liaison dans ces modèles est une autre voie prometteuse. En outre, l'étude du rôle des espèces deutérées et des états de spin dans la formation de l'ammoniac pourrait donner lieu à des résultats intéressants. Les simulations d'expériences, y compris celles qui ne concernent pas l'ammoniac, restent largement inexplorées mais sont cruciales pour une compréhension plus profonde des processus réels qui se produisent dans la chimie connue. C'est pourquoi nous visons à développer notre modèle dans ce domaine afin d'en faire profiter la communauté scientifique dans son ensemble. En plus de l'ammoniac, des recherches supplémentaires sur d'autres molécules contenant de l'azote, telles que le HCN, le CH_3CN et le CH_3NH_2, pourraient mettre en évidence des différences dans leur chimie, offrant ainsi de nouvelles perspectives sur la partition élémentaire de l'azote dans les régions de formation d'étoiles.

Cette thèse a jeté les bases de ces études futures, en proposant des méthodologies déjà en cours et en indiquant la voie à suivre pour poursuivre l'exploration de l'ammoniac et des espèces apparentées dans le contexte de la formation des étoiles.

A

Supplementary Material for Chapter 2

A.1 Additional experiments to study the behaviour of ammonia with H_2O, ^{13}CO, and CO_2

Table A.1 lists additional codeposition experiments performed to study the behaviour of ammonia with H_2O, ^{13}CO, and CO_2. These experiments are an extension of the work presented in Chapter 2 (Table 2.1). As their results exhibit similar trends, they have been excluded from the main text to prevent repetition. Experiment 3 in the table serves as a control experiment to confirm that the observed trends in the main experiments are due to hydrogen bonding between NH_3 and H_2O, rather than interactions with ^{13}CO or CO_2, and to check for any interactions between ^{13}CO and CO_2.

Table A.1: Additional ice experiments of ammonia with H_2O, ^{13}CO, and CO_2

No.	**Experiment**	**Ratio**	**Quantity Deposited (ML)**
1	$\{NH_3 + H_2O\}$	1:3	5(NH_3), 16 (H_2O)
2	$\{NH_3 + H_2O\}$	1:1	5 of each
3	$\{NH_3 + CO_2 + {}^{13}CO\}$	1:3:15	7.4 (^{13}CO), 1.7 (CO_2), 0.5 (NH_3)
4	$\{NH_3 + CO_2\}$	1:3	6 (NH_3), 18 (CO_2)

B

Supplementary Material for Chapter 3

B.1 Relative ice abundances of key volatiles in the model protostellar core

In Fig. B.1, we present the simulated abundances of key volatile compounds found in ices, namely NH_3, CO, CO_2, CH_4, and CH_3OH with respect to H_2O abundances, in our model of IRAS 16293-2422. We compared our predictions with the reported values in Boogert et al. (2015) (Table 2). Here, we focus on simulated abundance ratios beyond 2000 AU. In our model, the higher temperatures below 2000 AU, reaching around 200 K in the central regions, result in very little ice remaining on the grains, making ice abundances less meaningful in these areas. Therefore, we show ice abundances beyond 2000 AU, where the lower temperatures (around 10-20 K) result in more substantial freeze-out of species and, consequently, higher ice abundances. Our findings for CO and CH_3OH align well with the range observed in low-mass young stellar objects (LYSOs) as described in Boogert et al. (2015). Although our estimates for CH_4 abundances are slightly elevated, they remain reasonably close to the values reported in their work. Our model estimates CO_2 levels lower by two orders of magnitude, while NH_3 is overestimated by a factor of three, for LYSOs. These discrepancies may stem from a variety of factors, such as the elemental abundances used in our model, the impact of background emissions on the observed line intensities, missing grain-surface chemistry, and non-diffusive chemistry (Garrod & Pauly 2011), particularly in the case of CO_2. A comprehensive discussion of the cause of these variations exceeds the scope of our current study and is therefore not attempted.

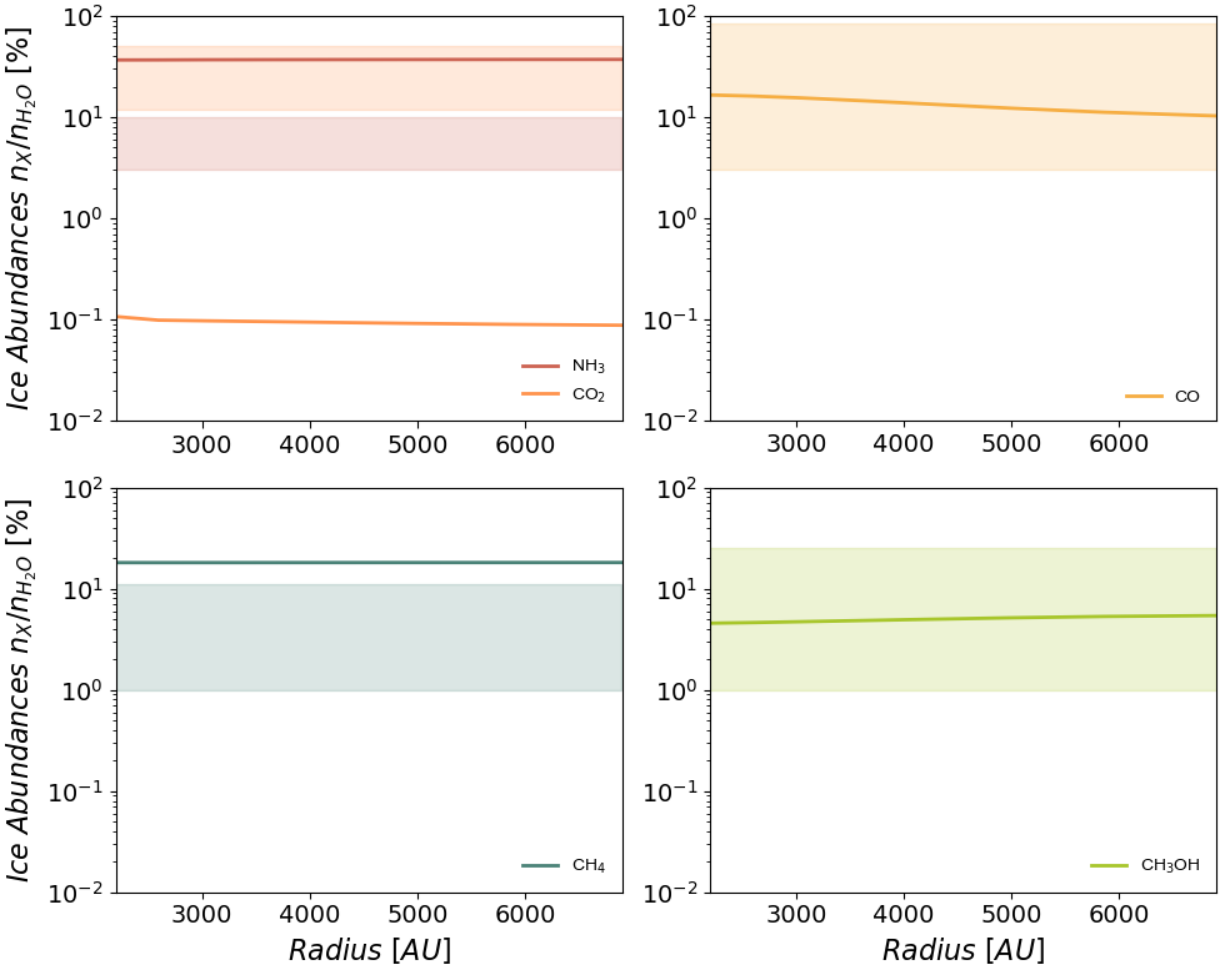

Figure B.1: Relative ice abundances of key volatiles with respect to water ice. The solid lines represent values obtained in this work and the shaded zones of the same colour represent the range of observed values reported in Boogert et al. (2015) in low mass young stellar objects.

Bibliography

Boogert, A. A., Gerakines, P. A., & Whittet, D. C. 2015, Annual Review of Astronomy and Astrophysics, 53, 541

Garrod, R. T. & Pauly, T. 2011, The Astrophysical Journal, 735, 15

Acknowledgements

First and foremost, I'd like to thank coffee, the true MVP of this thesis. Without its unwavering support and relentless caffeine boosts, these pages would still be a distant dream. Secondly, a big shoutout to my favorite procrastination tools - YouTube rabbit holes, pretty Pinterest boards, and that mysterious urge to clean my entire apartment whenever deadlines loomed. You all made this journey just a bit more... interesting!

On a more serious note, I owe a tremendous debt of gratitude to my advisors - Francois Dulieu, Paola Caselli, and Olli Sipilä - for their patient and watchful guidance throughout this journey. Like careful mentors, you allowed me the space to explore and learn, while gently nudging me when necessary to ensure I stayed on track. Your support has been invaluable, even during those times when my research felt as lost as a sock in the laundry. A special thanks also to Stephanie Cazaux, the experte externe, whose insightful feedback during my annual thesis evaluations has been very helpful in my growth.

This PhD journey was a tale of two cities - and not the Dickens kind, although it had its share of drama! To my incredible colleagues and friends at LERMA, Paris - Julie, Francesco, Franciele, Emanuele, Laurent, Saoud, Stephane, Abdi, Henda - you made those gruelling lab days bearable, and dare I say, even enjoyable. Francesco, your spontaneous opera performances were the soundtrack I never knew I needed. Julie, your presence alone was enough to make my day better. Laurent, your friendship was like a reliable Wi-Fi connection - always there when I needed it most. And Emanuele, listening to the Italian music from your office was the perfect antidote to lab-induced headaches.

Moving to CAS, Munich - what an experience! A huge thank you to everyone (too many of you to name without turning this into another thesis) for making my time there unforgettable. My office mates - Judit, Teresa, and Jelke - thank you for all the memories. Teresa, your cat photos were always delightful. Jelke, those unintentionally long conversations were a masterclass in procrastination, and I wouldn't have chosen a better dance partner to waltz through this PhD. Judit, our Studio Ghibli movie nights and shared complaints about the office temperature were life-savers. I still miss seeing your face pop up between my monitors at 12 pm sharp with that cheeky "lunch?" look.

To my gal pals - Caroline, Farideh, Hayley, and Judit. Caroline, your boss-woman energy, sarcasm, and gluten-free snacks kept me going, especially in the final stretch. Farideh, as my former flatmate, you had the unique challenge of enduring my morning chirpiness when you were still in zombie mode, and I'm so grateful for your patience. Hayley, thank you for being my sounding board, both in science and in life. Our walks and talks were a breath

of fresh air, and your relentless support - especially when I questioned my own sanity - meant the world to me. You were always there to cheer me on, keeping me grounded and reminding me that I could do this, even when I wasn't so sure myself. Judit (again), I'll forever cherish our deep (and shallow) conversations about life, Japan and everything under the Sun. Your friendship was like a warm cup of tea (or in my case, coffee) on a cold Munich day - comforting, energising, and always just what I needed.

A huge thank you to Anirvan - I'm so glad I found someone who shares my borderline obsession with cooking (and, of course, eating) amazing food, no matter how complicated the recipe. We're truly culinary soulmates. My dear Jas, you're like the sister I always wanted. I missed your aloo parathas (and you, of course) more than ever, especially in the final stretch of thesis writing. My time in Paris wouldn't have been the same without our adventures around the city to our favourite spots (you know exactly the ones I mean). Your aloo parathas were my comfort food and my motivation!

A special shoutout to Ryan, Chris, Lily, and Jere - my Garching crew - for all the fun and unforgettable times. You guys made the journey a whole lot brighter!

To my rocks - Florent and my bhaiyya (older brother) Pradeep - your support has been invaluable. Florent, your friendship has been a steady anchor, offering a listening ear, wise advice, and much-needed laughter. Bhaiyya, your unwavering belief in me has been a constant source of comfort. You've both been my pillars of strength through every curveball this PhD (and life) threw at me. I honestly don't know where I would be without either of you; your combined support has been fundamental to my journey.

To my parents, Suresh and Bindu - achha and amma - I owe everything to you. Thank you for always encouraging me to reach for the stars, both literally and figuratively, and for pushing me to aim high and stay resilient. I'm deeply grateful for your constant support and the sacrifices you've made to help me reach this point.

Lastly, I must acknowledge the stars themselves, for reminding me that even the smallest speck in the universe can have a profound impact - just like this thesis, which I hope contributes, even if only a little, to the vast field of knowledge.